6-17-2018

Development of a Slab-based Monte Carlo Proton Dose Algorithm with a Robust Material-dependent Nuclear Halo Model

John Wesley Chapman Jr
Louisiana State University and Agricultural and Mechanical College

DEVELOPMENT OF A SLAB-BASED MONTE CARLO PROTON DOSE ALGORITHM WITH A ROBUST MATERIAL-DEPENDENT NUCLEAR HALO MODEL

A Dissertation

Submitted to the Graduate Faculty of the
Louisiana State University and
Agricultural and Mechanical College
in partial fulfillment of the
requirements for the degree of
Doctor of Philosophy

in

The Department of Physics and Astronomy

by
John Wesley Chapman Jr
B.S., Louisiana State University, 2008
M.S., Louisiana State University, 2012
August 2018

ACKNOWLEDGMENTS

This project required substantial supplemental theory beyond the typical medical physics curriculum. I am grateful to Dr. Kenneth Hogstrom for providing this additional instruction and am humbled to have been taught by a prominent expert in this field. I also am thankful for my thorough and helpful advisor, Dr. Jonas Fontenot, whose guidance has improved both my technical communication and challenged me to critically evaluate every step in my project.

I acknowledge my family for their support, with special emphasis on my parents. They have taught me to never let fear of the unknown interfere with my goals. My parents' recent illnesses have motivated me to pursue science with renewed purpose, especially in the area of treating human disease. I hope that upon completion of my training I can end up a fraction of what they are, and that my knowledge can one day approach their level of wisdom. I thank everyone who has patiently sat and listened to explanations of my research and feigned interest. I thank my siblings for being amazing friends, and I am grateful that all in my family have become my biggest fans, even though I am still not sure if they know exactly what medical physics is.

It seems to me no coincidence that my incredible wife, Rebecca, entered my life when I began graduate studies. She has been there from the start and will be there at the end to celebrate our next phase of life together. Rebecca, I could not think of a better person to have spent my life with. Thank you for always being a friend, an inspiration, and especially my advocate. Thank you even more for being the love of my life. I am grateful to Rebecca for her patience in tolerating the long hours required to complete this project, often carrying well into the night. I am grateful that she supported my goals; after all, a good portion of this dissertation was written using a 55" HDTV and a recliner during nighttime hours. Throughout this project, Rebecca has been a constant source of inspiration, always finding unique ways to make me laugh (mostly cat jokes). She has always found a way to help me remain positive and focused.

TABLE OF CONTENTS

ABSTRACT

Pencil beam algorithms (PBAs) are often utilized for dose calculation in proton therapy treatment planning because they are fast and accurate under most conditions. However, as discussed in Chapman *et al* (2017), the accuracy of a PBA can be limited under certain conditions because of two major assumptions: (1) the central-axis semi-infinite slab approximation; and, (2) the lack of material dependence in the nuclear halo model. To address these limitations, we transported individual protons using a class II condensed history Monte Carlo and added a novel energy loss method that scaled the nuclear halo equation in water to arbitrary geometry. Our results indicated significant reductions in primary dose difference distal to laterally finite slab heterogeneities (~15%) compared to our previous model. Furthermore, our improved nuclear halo model decreased the distance-to-agreement (DTA) of the 1% isodose lines near heterogeneities by ~2-7 mm, and resulted in significant in-field improvement for deep air slabs (~2% improvement in total dose at the peak). Evaluation of both of these improvements in more clinically relevant geometries revealed an improved DTA of the 1% isodose line (~0.3-3 mm) and a reduction of maximum dose near the peak (18-27% reduced to 6-15%). Overall, the two modeling improvements made in this work have resulted in a dose model with significantly higher dose calculation accuracy across a wide range of particularly challenging geometries.

CHAPTER 1. INTRODUCTION

1.1 Overview

Proton therapy has gained widespread appeal and implementation into numerous external beam radiation treatment facilities. As of July 2017, the Particle Therapy Cooperative Group (PTCOG) reported sixty-four proton therapy facilities in operation and sixty-three either under construction or in the planning stages worldwide (PTCOG 2017). This development is attributed to the dosimetric benefits offered by protons, including: a sharp lateral penumbra, a narrow Bragg peak that can be modulated to arbitrary width, and a finite range, beyond which there is clinically insignificant dose. As will be shown, these dosimetric properties result from the physical interactions between protons and matter.

As interest in proton therapy continues, there has been a trend toward improving the precision of these treatments. For instance, the proton range (a critical factor for planning a patient treatment) is subject to uncertainties in imaging, patient setup, beam delivery and dose calculation. The specific parameters that define each of these aspects of patient care are typically managed using computer-based treatment planning systems (TPS). A TPS is used to evaluate the dose distribution in several beam configurations, and identify the configuration resulting in optimal tumor and non-tumor dose. However, the extent to which dose conforms to the tumor or spares normal tissue is limited by the previously mentioned uncertainties. Therefore, reducing the uncertainties of any one of these aspects directly results in a more conformal plan.

An essential component for the quality of a radiotherapy treatment plan is the accuracy of the dose calculation model. Although the clinical advantages of more accurate dose calculations have not been fully quantified, studies have shown that 5% changes in dose can result in 10-20% changes in tumor control probability (TCP), or up to 20-30% changes in normal tissue complication probabilities (NTCP) (Stewart and Jackson 1975, Goiten and Busse 1975, Orton *et al* 1984). Thus, maximizing the accuracy of dose calculations in treatment planning potentially translates directly to both improved tumor control and a reduction in incidence and / or severity of side effects.

Paganetti (2012) published a comprehensive study on this matter and posited reducing uncertainties in the proton range would allow a reduction of the treatment volume, permitting better utilization of the dosimetric advantages inherent to protons. In some cases, reducing some of these uncertainties will likely require the development of new technologies – such as replacing the now standard photon-based computerized tomography (CT) imaging technologies with proton-based solutions. Reduction of uncertainties in beam delivery and patient setup may require new procedures. However, Paganetti estimated that the largest uncertainties in the range were due to the analytical approximations used in current dose calculation technologies, amounting to ~+/-3% (1.5 standard deviations); he further speculated that the uncertainties in this category could be reduced to ~+/-0.2% using a dose calculation tool that more realistically models proton transport and interaction physics, especially in inhomogeneous regions.

An additional critical component that needs to be included in any proton dose calculation model is the dose resulting from secondary particles generated in nonelastic nuclear interactions (Pedroni *et al* 2005). The physical basis for this phenomenon will be discussed in a later section, but it has been shown that neglecting this effect in a proton dose model may result in systematic errors for small fields (~10-15%), depending on the size of the target volume (Pedroni *et al* 2005, Soukup *et al* 2005).

Thus, the literature indicates higher accuracy proton dose calculation algorithms would improve treatments and better utilize the dosimetric advantages inherent to proton therapy. Additionally, the increasing focus on conformal treatments places emphasis on developing higher accuracy dose calculations algorithms. All of these considerations will be further expanded on in the following sections.

1.2 Proton Physics

In this section, we consider the subset of interaction physics important for dose calculations in proton therapy. To facilitate discussion, this overview will be divided into three broad categories: energy loss, scatter, and nuclear interactions. Furthermore, emphasis will be on interactions resulting in the beneficial dosimetric properties previously mentioned, as well as concepts and equations relevant to discussion in proceeding sections. Detailed coverage of proton interactions in matter is available in the literature (Chu *et al* 1993, Pedroni

et al 1995, Lomax 2009, ICRU 1998, ICRU 2007, Newhauser *et al* 2015). In the sections that follow on dose calculation, discussion of dose models is broadly separately into two categories: "primary" and "secondary" (sometimes called "nuclear halo") dose. "Primary" dose is used to refer to dose due to protons which were present at the start of the simulation (i.e., those protons that originate from the beam). As such, these protons are the ones that encounter energy loss interactions (section 1.2.1), multiple Coulomb scatter (MCS) (section 1.2.2) and larger angle scatter events, and fluence loss in nonelastic nuclear interactions (section 1.2.3). However, the "primary" dose term is based on analytical functions which cannot fully characterize all such events (for instance, the scatter model is based on a Gaussian, which is not capable of quantifying all large angle scatter events). The intention of the "secondary" dose term is to model dose due to secondary protons created in nonelastic nuclear interactions; however, events that are not adequately modeled by the primary term are also inherently accounted for in the secondary term since the total dose is fit to Monte Carlo data in water (see Chapter 2).

1.2.1 Energy Loss

As protons traverse matter, their energy is reduced by numerous inelastic interactions with atomic electrons. The electrons are ionized in these interactions, depositing energy mostly in local tissue, which results in absorbed dose. The proton's large mass relative to that of the electron (1,832 times larger) results in negligible deflections during these events so that protons trajectories are very closely approximated by straight lines (see Figure 1.1); for this reason, energy loss can be quantified without considerations of scatter. These frequent energy loss events that protons encounter in matter results in a continual decrease in energy. After a proton has insufficient energy for further transport into matter, the proton stops, resulting in a finite range that is a function of the incident energy. Protons can also lose energy in elastic interactions with the atomic nucleus, however, this energy loss mechanism only becomes an important contribution to the overall dose at low energies, toward the end of range. In this work, energy loss via nuclear elastic interactions was not an important effect to model because it did not result in any difference in terms of the proton range. A less significant form of energy loss (negligible in therapeutic scenarios) is called Bremsstrahlung, meaning "braking radiation," in

which the proton is deflected by the nucleus and the kinetic energy lost in this process is carried off by a photon to deposit dose in a remote area.

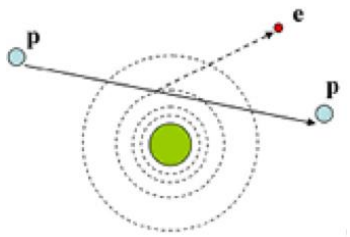

Figure 1.1. Protons lose energy mainly via inelastic Coulomb interactions with atomic electrons. Modified from Newhauser *et al* (2015).

The large number of protons in a therapeutic beam and the statistical nature of interaction cross sections infers that energy loss events are amenable to statistical treatment. Therefore, the energy loss rate, also called the linear stopping power, is defined as the ratio of the differential mean energy loss to depth in the material of interest. A more convenient expression of the energy loss rate is the mass stopping power, which is independent of the mass density. The linear stopping power is indicated by S, and the mass stopping power makes the density independence explicit, S/ρ. The stopping power is often further subdivided into electronic and nuclear stopping powers; the electronic stopping power characterizes energy loss events with atomic electrons whereas the nuclear stopping power characterizes energy loss due to elastic interactions with the nucleus. As mentioned previously, the nuclear stopping power was not included in the new dose model discussed in this work. In fact, Gottschalk *et al* (2015) states that in a model such as ours, it is conceptually incorrect to include the nuclear stopping power.

Numerous formulations have been presented for the linear electronic stopping power (Bragg and Kleeman 1905, Bohr 1915, and Bethe 1930 and Bloch 1933), but the most accurate formulation, called the Bethe-Bloch formula (Bethe 1930, Bloch 1933), takes relativistic and quantum mechanical considerations into effect and has the following form,

$$\frac{S}{\rho} = \frac{-dE}{\rho dx} = \frac{4\pi N_A r_e^2 m_e c^2}{\beta^2}\frac{Z}{A}\left[\ln\frac{2m_e c^2\gamma^2\beta^2}{I} - \beta^2 - \frac{\delta}{2} - \frac{C}{Z}\right], \quad (1)$$

where $N_A = 6.022x10^{23}\ mol^{-1}$ is Avogadro's number, $r_e = 2.818x10^{-13}\ cm$ is the classical electron radius, $m_e c^2 = 0.511\ MeV$ is the rest mass of an electron, β is the ratio of the velocity of the proton to the speed of light, Z is the atomic number and A is the atomic weight of the material of interest, $\gamma = (1-\beta^2)^{-1/2}$, I is the mean excitation potential of the material, δ is a density correction due to shielding of remote electrons by local electrons, and C is a shell correction term.

The energy loss rate is inversely proportional to β^2, which implies an infinitely high and infinitesimally narrow peak as β approaches zero; this results in the monoenergetic Bragg peak that is characteristic of proton beams. However, stochastic variations in proton energy loss (energy straggling) (Bohr 1948) result in slight changes in proton path lengths (range straggling). The overall effect of range straggling is a broadening of the Bragg peak that increases with increasing depth. For instance, a proton stopping power computation by Berger *et al* (2005) resulted in the range straggling evident in Figure 1.2. Energy straggling theories for thick (Bohr 1915), intermediate (Landau 1944), and thin slabs of material (Vavilov 1957) have been characterized. The simplest formulation is by Bohr (1915), in which the energy straggling is modeled as a Gaussian. Further simplifications of Bohr's theory have been presented as parameterizations of the RMS width of the Gaussian based on range (Chu *et al* 1993).

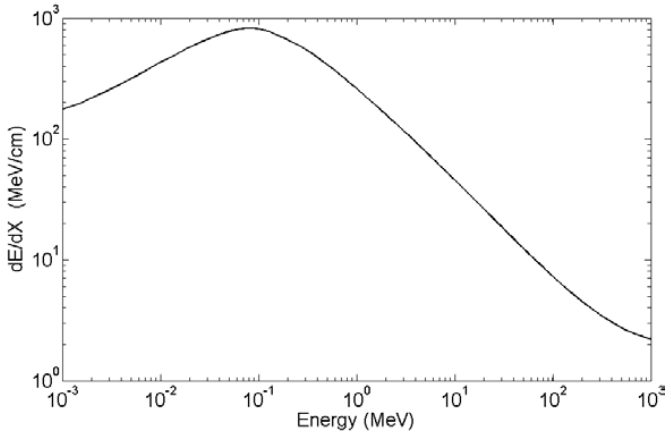

Figure 1.2. Computed linear stopping power in liquid water vs. proton energy (Berger *et al* 2005).

A consequence of protons traveling in nearly straight lines is the near equivalence of the proton range and average proton pathlength. The assumption that protons lose energy continuously is referred to as the continuous slowing-down approximation (CSDA), which is often used in dose calculation models. Using the

CSDA, the proton range is calculated by integrating the reciprocal of the linear stopping power as a function of energy. Additionally, using the CSDA, energy loss over discrete distances Δx is calculated using the product of the linear stopping power and Δx.

As a final point, equation (1) provides a theoretical framework for calculating stopping power, but it is often more convenient to obtain stopping power values from readily available databases that perform all the computations needed. Although there are certain dose calculation models that actually compute equation (1) for a large number of particles, it is typically more convenient and less resource-intensive to use a tool such as PSTAR (Berger *et al* 2005) or SRIM (Ziegler *et al* 2012). For example, PSTAR is an online tool that calculates stopping power (electronic, nuclear, total) and range (CSDA, projected) for a database of pre-determined materials and user-selected energies. Similarly, SRIM calculates ion stopping power and range values in several biological materials and for a wide range of energies.

1.2.2 Scatter

Protons near the atomic nucleus may encounter a repulsive force due to the positive charge of the nucleus. This elastic Coulomb interaction deflects the proton away from the nucleus (Figure 1.3). In this interaction, the proton energy loss is negligible, and the deflection angle tends to be small. For this reason, scatter may be quantified without considering energy loss. Like the energy loss rate, it is typically more convenient to express scatter in a stochastic form.

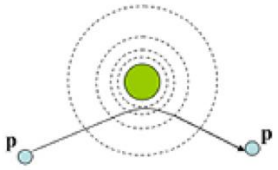

Figure 1.3. Protons are deflected mainly via elastic Coulomb interactions with atomic nuclei. Modified from Newhauser *et al* (2015).

Individual proton scatter events in the vicinity of an atomic nucleus tend to be very small; however, as protons proceed through the medium, the accumulation of a large number of these deflections has a larger impact on the lateral displacement. Because there are a large number of small scatter events and because of the statistical nature of this phenomenon, it can be quantified using the central limit theorem. Thus, the probability

density describing what is called *multiple Coulomb scatter (MCS)* angles is modeled by a statistical distribution, typically a Gaussian. MCS is the primary interaction that determines the sharpness of the lateral penumbra.

MCS relies on, and is derived from an accurate model of *single scatter*, which according to Rutherford (1911) can be calculated using

$$\xi(\chi) = \frac{d\sigma}{d\Omega} = Zr_e^2 \frac{(m_e c^2/\beta\rho)^2}{4\sin^4(\chi/2)}, \tag{2}$$

where $d\sigma$ is the differential cross section for scattering into solid angle $d\Omega$, and χ is the single scattering angle. In equation (2), the Rutherford dependence is roughly χ^{-4}. The true mathematical form for scatter, therefore, should approach χ^{-4} at large angles. Moliere's scatter theory (Bethe 1953) includes all these effects, as well as scatter events intermediate to MCS and single scatter, called plural scattering. For that reason, and because Moliere theory has been demonstrated to have excellent agreement with measurements (Gottschalk *et al* 1993), it is considered the most accurate scatter theory. However, Moliere theory also requires numerous calculations, including numerical integrations that could be potentially time-consuming depending on the material composition of the calculation geometry. For that reason, a Gaussian approximation is typically preferred. Regardless of the statistical distribution used to model MCS, the characteristic scattering angle must be determined. For this purpose, a differential quantity is defined that can be integrated to determine the mean squared scattering angle of a group of protons in an absorber. Integrating the characteristic angle of the single scattering distribution, the linear angular scattering power is derived,

$$T = \frac{d\langle\chi^2\rangle}{dx} = \frac{\int_{\chi_{min}}^{\chi_{max}} \chi^2 \xi(\chi)\, 2\pi\chi\, d\chi}{\int_{\chi_{min}}^{\chi_{max}} \xi(\chi)\, 2\pi\chi\, d\chi}, \tag{3}$$

where the denominator evaluates to unity. χ_{max} and χ_{min} are determined by considering the finite size of the nucleus for large angles and screening of the nuclear field for small angles (more details available in Rossi and Griesen 1941). Similar to the mass stopping power, this quantity can also be calculated independent of mass density so that the mass scattering power is given by T/ρ. There are several scattering power formulae available for protons (Gottschalk 2010). When using scattering power in a dose calculation

model, the spatial RMS width is often more useful than the scattering power. The various moments of the scattering power can be calculated according to Fermi-Eyges theory (Eyges 1948),

$$\sigma_j^2(x) = \frac{1}{2}\int_0^x (x - x')^j \, T\left(\bar{E}(x')\right) dx', \tag{4}$$

where *j=0* gives the sigma of the angular scattering Gaussian distribution, *j=1* is the covariance, and *j=2* gives the sigma of the spatial scattering Gaussian distribution.

1.2.3 Nuclear Interactions

Protons passing through matter may bypass the Coulomb barrier and interact with the nuclear field. In the event of a proton in proximity to the nucleus, the proton may transfer momentum to the nucleus (Figure 1.4). If the momentum transfer to the nucleus is large enough, it may disrupt the forces holding the nucleons together, which results in the emission of several secondary particles. These secondaries then redistribute energy. One of the effects of this type of interaction is a reduction of the primary proton fluence at about a rate of *1.2% $g^{-1}cm^2$* (see Figure 1.5) (ICRU 1993). Note that although the dose is somewhat reduced by reduction of primary proton fluence, ejected secondary particles redistribute dose. There are three types of nuclear interactions recognized by ICRU Report 63 (ICRU 2000): elastic, inelastic, and non-elastic. Elastic interactions were discussed in the previous section as being responsible for MCS and inelastic interactions are a special case of non-elastic interactions in which the nucleus is left in an excited state that usually sheds excess energy radiatively.

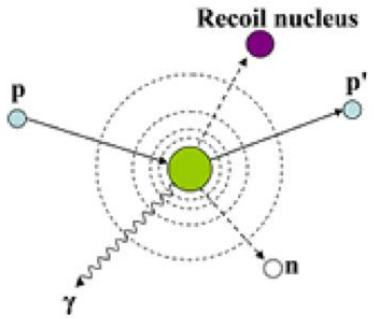

Figure 1.4. Protons are absorbed by the nucleus in non-elastic interactions and secondary particles are ejected and the resulting nucleus recoils. Modified from Newhauser *et al* (2015).

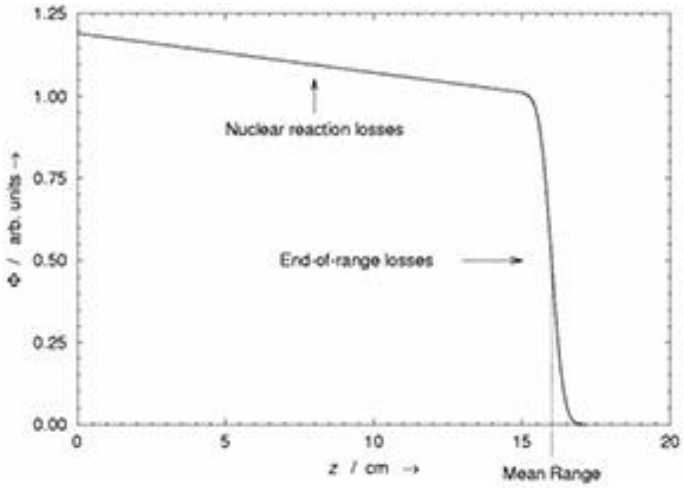

Figure 1.5. Primary proton fluence is reduced at a rate of about 1.2% $g^{-1}cm^2$. Data shown in water. From Newhauser *et al* (2015).

The cross section for non-elastic nuclear interactions in oxygen is shown in Figure 1.6. This figure shows that the cross section is zero up until a threshold of a few MeV, which is referred to as the Coulomb barrier because it is the energy needed to overcome the repulsive Coulombic force of the nucleus. The cross section also levels off around energies exceeding 100 MeV. The Evaluated Nuclear Data File (Chadwick *et al* 2011) database provides a repository for these cross sections.

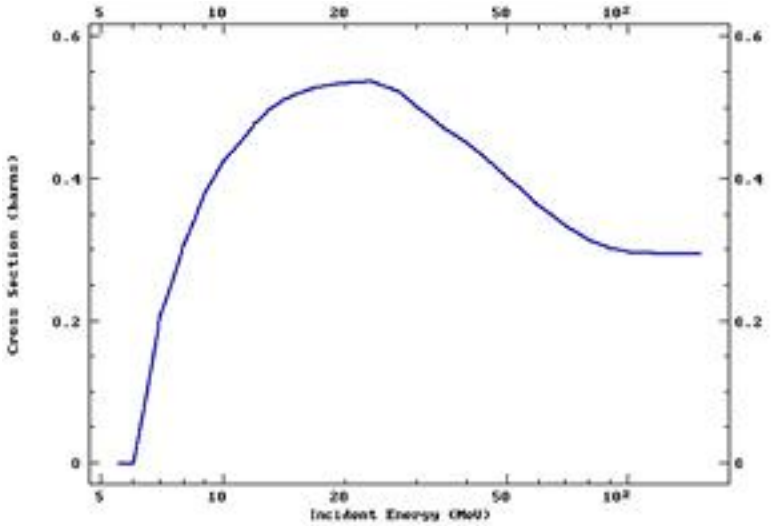

Figure 1.6. Total proton non-elastic nuclear cross section in oxygen vs incident proton energy. From Chadwick *et al* (2011).

In these non-elastic interactions, energy is carried away from the interaction site by secondary particles. The secondaries in these interactions include short-range charged particles, and long-range neutral particles. The energy carried off by long-range neutral secondaries either exits the target completely or is redistributed;

for this reason, the energy deposited in the Bragg peak is lowered (Gottschalk 2004). Figure 1.7 shows how the Bragg peak value is lowered as a result of these neutral particles carrying off some of the incident proton energy. The short-range charged secondaries resulting from non-elastic nuclear events carry off low energies relative to the incident proton and scatter out into a faint halo of secondary dose (Pedroni *et al* 2005); for this reason, proton beams are said to exhibit a "nuclear halo" (Pedroni *et al* 2005).

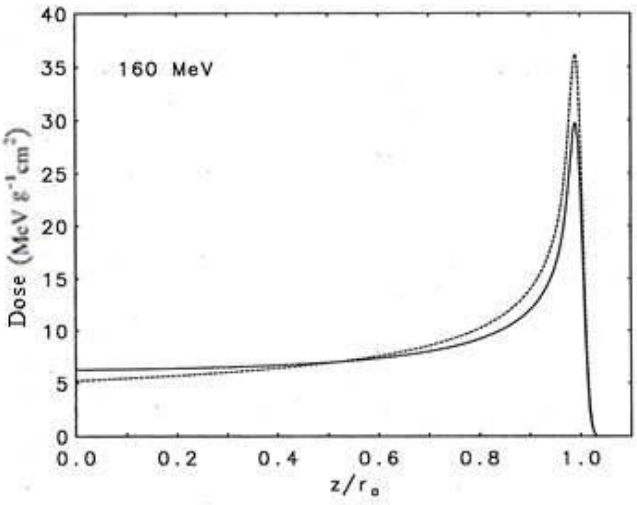

Figure 1.7. Monte Carlo calculations of the Bragg peak with nuclear reactions turned off (dashed) and the actual Bragg peak (solid) (Berger 1993) for a 160 MeV beam in water.

1.3 Dose Calculation Approaches

Monte Carlo (MC) dose models have long been considered the gold standard for dose calculations (Schaffner *et al* 1999, Paganetti *et al* 2008, Schuemann *et al* 2014, Schuemann *et al* 2015). Indeed, the MC approach has been shown to provide higher dose calculation accuracy than analytical models (Titt *et al* 2008, Koch *et al* 2008, Newhauser *et al* 2008, Paganetti *et al* 2008, Schuemann *et al* 2014, Schuemann *et al* 2015), but this also requires increased computational resources and longer calculation times that limit its widespread application in routine treatment planning. For instance, in one study using the MC code Monte-Carlo N-Particle eXtended (MCNPX) (Pelowitz 2011), Taddei *et al* (2009) simulated a typical three-beam proton lung cancer treatment that required 5,000 hours on a single central processing unit. Although advances in computer hardware and parallel processing techniques (especially those involving graphical processing units (GPUs)) have resulted in faster computation times for general purpose MC codes, this would still require specialized

hardware and increased costs that many cancer clinics would be reluctant to adopt. Additionally, GPUs have a highly vectorized architecture which is not well suited for parallel processing of independent particle transport. Finally, GPU-based general purpose Monte Carlo would likely still result in long calculation times in certain applications, such as four-dimensional treatment plans and inverse planning (Keall *et al* 2004, Jeraj *et al* 2002, Jeraj *et al* 1999). For these reasons, dose calculation models that strike a balance between speed and accuracy have been the focus in the literature.

Typically, analytical proton dose models used in commercial treatment planning systems (TPS) are based on pencil beam algorithms (PBA) (Petti 1992, Russell *et al* 1995, Hong *et al* 1996, Deasy 1998, Schneider *et al* 1998, Schaffner *et al* 1999, Szymanowski and Oelfke 2002, Ciangaru *et al* 2005, Schaffner 2008, Westerly *et al* 2013, Chapman *et al* 2017, Inaniwa *et al* 2017), which segments a broad beam into many smaller composite beams (called "pencil beams"). These proton dose models typically follow the formalism of the electron dose model developed by Hogstrom *et al* (1981). Computation speed is an important factor in calculation of radiotherapy treatment plans because it accommodates high patient throughput, and repeated calculations needed during plan optimization and plan adjustment. Thus, PBAs are typically used because they achieve a balance between accuracy and computation speed. However, the speed of PBAs is achieved mainly through approximations of the underlying physical interactions that ultimately limits the accuracy of this class of algorithms. It can be instructive to examine some of the more commonly used approximations and the circumstances under which their accuracy decreases.

One approximation that has become customary in PBAs is the central-axis semi-infinite slab (CAXSIS) approximation (Hogstrom *et al* 1981). In this approximation, materials encountered by the central-axis of each pencil beam are considered to be laterally infinite homogeneous slabs. To illustrate the limitation this imposes, consider a pencil beam with its central-axis originating in water with enough lateral scatter at a given depth to spread part of the pencil beam distribution into an adjacent material of differing composition. In this example, the CAXSIS approximation would be used to model those particles that extend into the adjacent material as though they were in water, even though they are not (Figure 1.8).

Due to the CAXSIS approximation, PBAs work well for simple heterogeneous or slab-structured phantoms (Schaffner *et al* 1999, Soukup *et al* 2005, Ciangaru *et al* 2005), but these approaches have mixed success in calculating proton dose in areas with combinations of high- and low-density media (Ciangaru *et al* 2005, Yamashita *et al* 2012, Schuemann *et al* 2015, Chapman *et al* 2017).

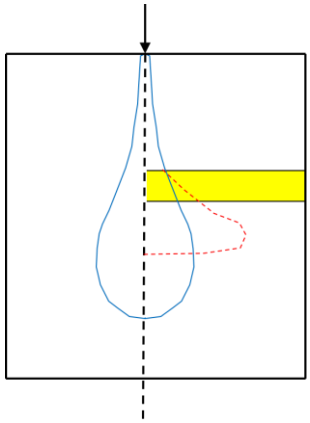

Figure 1.8. An illustration of the limitations imposed by the central-axis semi-infinite slab approximation in heterogeneous regions. The central-axis (dashed black line) for a single pencil beam is shown entering a water phantom (white areas within black rectangle) containing a half bone slab (yellow rectangle), along with a representative dose envelope for the pencil beam in water (blue). Due to this approximation, the pencil beam dose is computed as though it were only in water, even though some of it extends into the bone slab. The red dashed shape shows how the dose envelope should be modified for this pencil beam to properly account for the bone slab.

In a previous publication (Chapman *et al* 2017), our PBA was tested relative to simulations in MCNPX for energies including 100, 150, 200, and 250 MeV, field sizes including 4x4 cm^2 and 10x10 cm^2, and geometries including homogeneous phantoms of various composition (water and compact bone) and heterogeneous slabs (compact bone or air) that either extended across half of the phantom (laterally finite) or across the entire phantom (laterally infinite).

The results obtained in homogeneous and laterally infinite geometries (Figure 1.9) indicated that the introduction of heterogeneous materials caused inaccurate calculation of low isodose values, which were amplified at the level of the slab, and inaccurate dose calculations distal to the proximal edge of the slab (most noticeable at the Bragg peak). These inaccuracies were at least partially due to parameterizing the nuclear halo model in water without adding in a robust material dependence. The over- or under- estimation of the Bragg

peak resulted from scaling the absorbed dose describing the nuclear halo to materials of interest using only a ratio of stopping powers rather than explicitly modeling the production and transport of secondary protons.

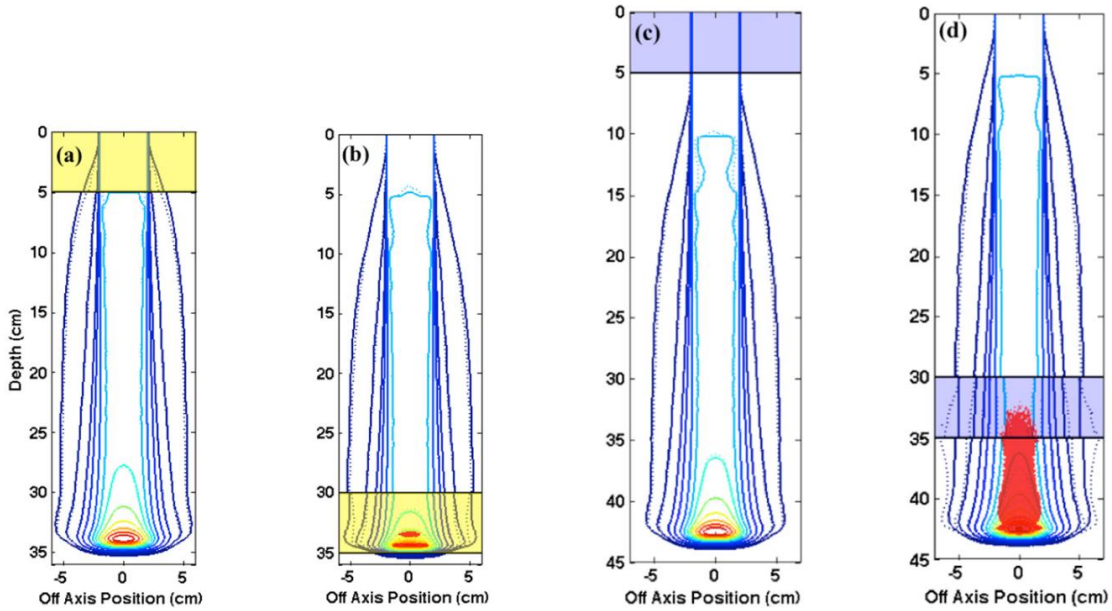

Figure 1.9. Isodose comparisons between MC (dashed) and PBA (solid) for a 250 MeV, 4x4 cm^2 beam incident on a water phantom with a 5 cm slab. Both compact bone (yellow) slabs at the surface (a) and at *z=30* cm (b) are shown, along with air slabs (blue) at the surface (c) and at *z=30* cm. Pass-rates within 2% dose difference or 1 mm distance-to-agreement were 100% (both (a) and (c)), 99.5% (b), and 93.2% (d). Isodose lines shown are 1, 2, 5, 10, 20, 30, 40, 50, 60, 70, 80, 90, and 100%. All pixels within the 1% isodose line were evaluated using our 2% or 1 mm criteria, and regions that failed this criteria are indicated in red.

For the laterally finite slab evaluations (Figure 1.10), the accuracy of the PBA worsened as the slab depth increased. The failures in these types of geometries were due to the CAXSIS approximation, and agreement worsened with depth simply because the scatter increases, and the pencil beam envelope was therefore larger at deeper depths, which resulted in more laterally distant points inaccurately attributed to the material encountered along the pencil beam central-axis (refer to Figure 1.8). For all deeply placed slabs, the PBA was not able to model dose perturbations caused by the sharp material interface between the heterogeneous slab and water. For a field incident upon the edge of a laterally finite slab, this resulted in the appearance of two hot spots and two cold spots distal to the slab heterogeneity.

With the accuracy limitations of some analytical approaches and speed limitations of MC approaches, there is interest in developing new approaches that can, perhaps, achieve a more favorable balance between the two. One approach is called the pencil beam redefinition algorithm (PBRA), originally described for electrons

by Shiu *et al* (1991). In the original Fermi-Eyges (Eyges 1948) based electron PBA (Hogstrom *et al* 1981), Hogstrom *et al* realized that electrons were scattering in air before reaching the field-defining plane where the pencil beams were modeled. Their solution was to mathematically redefine the pencil beams at the beam-defining plane, which allowed modeling of scatter both in air and in patient, without the scatter in air overtaking scatter in the patient. The PBRA was an extension of this original idea, where pencil beams were redefined every 1 cm in depth. The PBRA has also been applied to protons (Egashira *et al* 2013) but required GPU implementation because the lateral dose grid size had to be very small to accommodate the small proton scatter angles, which would result in slow calculation times on a standard CPU implementation. Discrete ordinate calculation models, which directly evaluates variants of the Boltzmann transport equation on a grid, (Sandison *et al* 2000) have also been described in the literature.

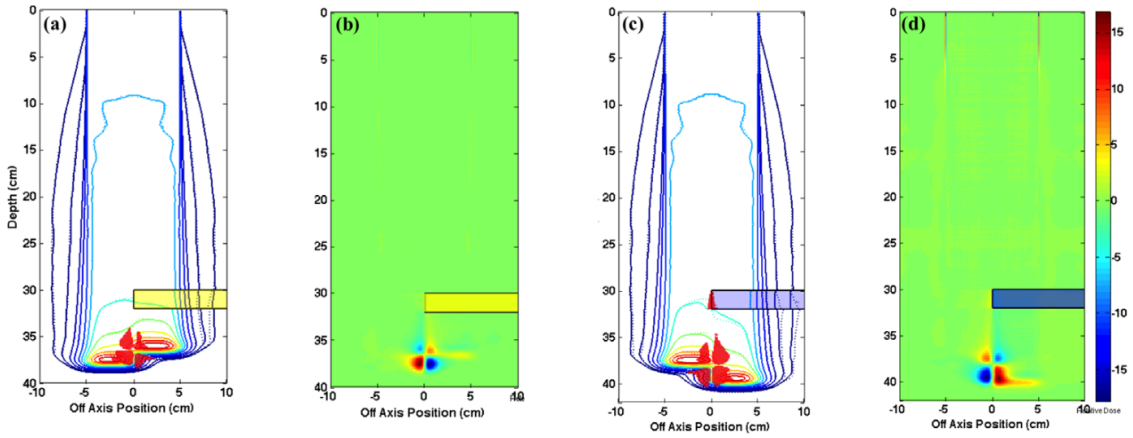

Figure 1.10. Isodose (a,c) and dose difference (b,d) comparisons between MC (dashed) and PBA (solid) for a 250 MeV, 10x10 cm^2 beam with a 2 cm (a) compact bone (yellow) slab and a (c) air slab (blue) at *z=30* cm. Pass rates were 98.6% (a) and 98% (c). Isodose lines shown are 1, 2, 5, 10, 20, 30, 40, 50, 60, 70, 80, 90, and 100% and regions that failed our criteria are indicated in red.

Another approach to achieving balance between calculation speed and accuracy are so-called "fast MC" codes. One such model, called the fast dose calculator (FDC, Yepes *et al* 2009), relies on pre-simulated proton trajectories in water (including path length, angles, energy loss, energy deposited, and stopping power information for each step), which are scaled to other materials, typically using a stopping power ratio of an arbitrary material to water. The FDC improved the dose calculation time by two orders of magnitude over a general-purpose MC code. Because the proton trajectories in these models were pre-simulated, the calculation

speed of this type of approach was fast but required processing an extremely large dataset that was best utilized in a graphical processing unit (GPU) environment (Yepes *et al* 2010).

Recently, the FDC was validated in water for proton scanning beams (Yepes *et al* 2016a), with greater than 99% of points over 23 patients within 2% or 2 mm. The FDC was also validated for use in intensity modulated proton therapy (IMPT) (Yepes *et al* 2016b) for 23 patient cases and more than 99% of the voxels in all patients were within 2% or 2 mm. Finally, the FDC was compared to dose calculated by the Eclipse treatment planning system (Varian Medical Systems) for 525 patients (Yepes *et al* 2018). Out of these 525 patient cases, the FDC was shown to under-predict Eclipse by more than 10% for 4 patient cases and by more than 15% for 2 patient cases, highlighting some potentially clinically significant dose differences in Eclipse. However, the FDC does not include a nuclear halo model, which could result in dose errors for high energy beams (Pedroni *et al* 2005).

In VMCpro (Fippel and Soukup 2004), protons were transported individually, step by step through the calculation geometry, and sampled interaction step lengths using a cross section previously described by Kawrakow (2000). Secondary particles and delta electrons were also individually transported. Excellent agreement was reported along the central-axis of pencil beam simulations (1% or 0.5 mm) between VMCpro and the general-purpose MC codes FLUKA (Ferrari *et al* 2005) and GEANT 4 (Agostinelli *et al* 2003) in homogeneous phantoms of various materials (adult soft tissue and skeleton), demonstrating high accuracy in the electromagnetic and nuclear models they used for those specific geometries. In a water phantom containing a bone-lung interface heterogeneity, however, they noted an under-prediction of dose by a few percent, mostly stemming from parameterization of their MCS scattering power only on mass density, and the inaccuracies caused by that approximation were magnified by the low density of lung. Another potential cause for this under-prediction is the absence of material dependence in their secondary dose model.

Despite these limitations, considerable speedup was observed in VMCpro (168 seconds) compared to general purpose MC codes (~35 times faster than GEANT 4 (99 mins) and ~13 times faster than FLUKA (37 mins)) for a 150-MeV pencil beam in the lung-bone inhomogeneous geometry mentioned previously. Given this

computation time, however, VMCpro would still be too time consuming for broad beam calculations, which would require the transport of several such pencil beams. Furthermore, the stochastic method used to transport secondary protons that characterize the nuclear halo is subject to statistical fluctuations and increase the calculation time beyond analytical methods.

Jia *et al* (2012) developed the gPMC, which implemented the Fippel and Soukup (2004) model on GPU. The gPMC had calculation times on the order of 6-22 seconds and for 30 patient cases, accuracy was within 1% or 1 mm for 94% of points within the 10% isodose line. Agreement below the 10% isodose line was not reported. They also noted that the 1% or 1 mm agreement stated did not apply to geometries with low-density air regions. Jia *et al* (2012) used the same simplified, material-independent implementation of the nuclear halo as Fippel and Soukup (2004). However, this model did result in 1-2% underestimation in target for prostate cancer cases (Giantsoudi *et al* 2015). Recently, Qin *et al* (2016) described the next iteration of this model, gPMC 2.0, which for a prostate cancer case increased the number of pixels within 1% or 1 mm from 82.7% (gPMC 1.0) to 93.1% (gPMC 2.0). However, they did not some differences in secondary proton dose when compared to TOPAS (Perl *et al* 2012, Testa *et al* 2013). Souris *et al* (2016) described a multi-core implementation of Fippel and Soukup (2004) and showed that their model agreed with GEANT4 (Agostinelli *et al* 2003) within 2% or 1 mm. Calculation times in this model were below 25 seconds for 10^7 protons with initial energy 200 MeV.

Tourovsky *et al* (2005) described a fast MC model that reduced the subset of interaction physics to the main interactions needed for dose calculation (i.e., energy loss, scatter, nuclear interactions). This approach retained most of the accuracy of general purpose MC while reducing the required time to calculate dose. In the fourteen patient treatment plans tested, the Tourovsky *et al* (2005) model resulted in nearly 90% of voxels within +/-5% agreement. Furthermore, comparing range calculations of their model to a proton radiograph system, it was shown that the differences in range were mostly between -5% to 2% and differences in range spread were between -1% to 3.5%. As demonstrated by Sawakuchi *et al* (2008), MCS within heterogeneities is the main contributor to the degradation of the distal edge of the Bragg peak, thus the small differences in range

and range spread in the Tourovsky *et al* (2005) model indicate that primary protons were transported accurately in heterogeneous geometries. Finally, for a typical treatment, this model required 20 minutes of calculation time.

Although the comparisons between radiograph measurements and range calculations in Tourovsky et al (2005) seem to indicate that the MCS model is accurate in heterogeneous geometries, the model nonetheless is configured in a way that limits accuracy in such cases. Additionally, there were several implementation details of their model that lent itself to inefficient calculations. For instance, they used a constant transport step size (~2 mm) in order to achieve reasonable dose calculation times. Near the Bragg peak, this step size is likely too coarse to adequately sample the rapidly changing stopping power in this area. This limitation could be the primary explanation for the wide range of dose differences and the long tail observed in their range difference histogram. Secondly, the geometries used to test the model have not fully probed the underlying accuracy of their dose model in heterogeneous tissue. For instance, the continuous changes of heterogeneities in CT geometries, the overlapping spot beams of various sizes and energies delivered from multiple angles, the large PTVs treated, and the wide range of materials (from air to Titanium) somewhat average out the inaccuracies that may be present under simpler conditions. Finally, their nuclear halo model was overly simplistic because it lacked material dependence and was based on a single Gaussian, which Li *et al* (2012) showed was insufficient for modeling the full lateral extent of the nuclear halo.

1.3.1 The Nuclear Halo

The concept of a "nuclear halo" of dose resulting from non-elastic nuclear interactions has been known to be an important contribution to proton dose for over a decade, with the first publication in this area by Pedroni *et al* (2005). In fact, Pedroni *et al* (2005) and Soukup *et al* (2005) demonstrated that the lack of a nuclear halo in a proton dose model could result in significant dose errors up to 10-15%, depending on the size of the target volume; therefore, the nuclear halo has a non-negligible effect on the proton dose distribution. Several models for the nuclear halo have been described in the literature, but unfortunately the physics of this phenomenon has only been studied in modest detail.

Despite the lack of knowledge in the physics of the nuclear halo, general purpose Monte Carlo (Agostinelli *et al* 2003, Ferrari *et al* 2005, Pelowitz 2011), which typically rely on the Bertini intranuclear cascade model (Bertini *et al* 1968) for calculating the dose due to non-elastic nuclear interactions, have been shown to agree well with measured data (Polf 2007, Kimstrand *et al* 2008, Titt *et al* 2008, Randeniya *et al* 2009). Some Fast Monte Carlo (FMC) models (Fippel and Soukup 2004, Jia *et al* 2012, Qin *et al* 2016, Souris *et al* 2016) have also been described, which use data from ICRU Report 63 (ICRU 2000) to stochastically transport secondary particles. However, because these FMCs transport primary protons and multiple types of secondary particles, many of them require parallel computing implementations (graphics processing units or multi-core central processing units) in order to achieve reasonable calculation times for clinical use.

Because stochastically-based nuclear halo models increase the calculation time, analytical models could be used to calculate nuclear halo dose instead to achieve a balance of speed and accuracy. Pedroni *et al* (2005) published the first analytical nuclear halo model, which used two Gaussians to model the fluence: one to account for MCS and another which was empirically fit to account for the nuclear halo. This same nuclear halo model was used in Tourovsky *et al* (2005). However, Li *et al* (2012) showed that a single Gaussian is not sufficient for modeling the lateral profile of the nuclear halo out to low isodose values.

Poor modeling of the nuclear halo could be somewhat countered by use of the so-called field-size factor, which forces the calculated dose to equal the measured dose at the center of a given field. Li *et al* (2012) described a model that reduced the field size factor correction by up to 50% compared to Gaussian models, which more realistically matched the lateral falloff of the nuclear halo as indicated by MC simulations. Their approach was to replace the single Gaussian that was typically used in PBAs with a weighted sum of both a Gaussian and a Cauchy-Lorentz term. Their model was parameterized in water and the results were only presented in a homogeneous water phantom. An extension of the Li *et al* (2012) model was implemented by Chapman *et al* (2017) in their PBA.

Despite the large number of publications on the nuclear halo (Pedroni *et al* 2005, Soukup *et al* 2005, Sawakuchi *et al* 2010a, Sawakuchi *et al* 2010b, Sawakuchi *et al* 2010c, Zhang *et al* 2011, Peeler and Titt 2012,

Clasie *et al* 2012, Anand *et al* 2012, Li *et al* 2012, Zhu *et al* 2013, Inaniwa *et al* 2016, Chapman *et al* 2017), none have resulted in a complete understanding of the physics in these interactions. Some of these studies rely on the parameterization introduced in Pedroni *et al* (2005), and all[1] of them apply a weighting factor to the planar integrated depth dose (PIDD) to model the energy loss for secondary particles in the nuclear halo; therefore, these models only used a one-dimensional calculation for estimating energy loss of secondary particles in the nuclear halo.

Recently, Gottschalk *et al* (2015) published the most detailed nuclear halo model to date, highlighting the physics and overall form of the nuclear halo for a 177-MeV proton beam in water. In his paper, Gottschalk *et al* (2015) took issue with the use of PIDDs in prior literature, arguing that the PIDD inherently includes both electronic and nuclear stopping power. Gottschalk *et al* (2015) noted that significant excess dose resulted from these prior models near mid range (particularly, Pedroni *et al* 2005), and attributed that to the inclusion of nuclear stopping power. He further stated that dose on the central-axis of a single pencil beam should not include dose deposited by secondary particles, which is inherently included in the nuclear stopping power. Therefore, energy loss modeling in current nuclear halo models is inaccurate.

Another limitation of all prior analytical nuclear halo models in the literature is the lack of robust material dependence. In fact, all prior analytical models used the effective depth in water, a one-dimensional calculation, to scale the nuclear halo to other materials. In a previous study (Chapman *et al* 2017), which also relied on the effective depth in water, we demonstrated that significant dose differences resulted distal to thick heterogeneities near the end of range, particularly air slabs. These dose differences were attributed to the lack of robust material dependence in the nuclear halo model. Note that Inaniwa *et al* (2016) introduced an additional scaling factor to scale the nuclear halo to non-water materials, but this factor was constant for each material; therefore, this correction is inadequate to correct for the errors observed below heterogeneities in Chapman *et al* (2017) because it is independent of slab thickness or proximity of the heterogeneity to the end of range.

[1] Chapman *et al* (2017) uses a parameterization based on the central-axis of a broad field, which is mathematically equivalent to the planar integrated depth dose by the reciprocity relationship (ICRU 1984).

1.4 Motivation for Research

Because general purpose MC dose models are not yet clinically viable due to the long calculation times required and because analytical models have limited dosimetric accuracy in some cases, much of the literature on proton dose models has been focused on development of fast Monte Carlo codes. Current fast Monte Carlo dose models result in high dosimetric accuracy and calculation times less than a minute but model the nuclear halo either by neglecting it entirely (Yepes *et al* 2008, Yepes *et al* 2010, Yepes *et al* 2016a, Yepes *et al* 2016b, Yepes *et al* 2018), relying on overly simplistic modeling (Tourovsky *et al* 2005), or using stochastic transport which increases calculation time (Fippel and Soukup 2004, Jia *et al* 2012, Qin *et al* 2016, Souris *et al* 2016). It is our opinion that the best balance of accuracy and speed for proton dose calculations may be achieved using a stochastic model for "primary" interactions (i.e., multiple Coulomb scatter and continuous energy loss from protons which have not been removed from the primary beam) and an analytical model for the "nuclear halo", provided the physics of the nuclear halo could be modeled in more detail. A stochastic model for the primary term would remove the dependence on the central-axis approximation, which should improve dosimetric accuracy in heterogeneous geometries. An analytically-based nuclear halo model would reduce calculation time relative to stochastic models because it does not require the transport of additional particles. The accuracy of such a model is dependent on the validity of the approximations made.

Gottschalk *et al* (2015) has published the most detailed, physics-based model on the nuclear halo in water to date, but the physics of the nuclear halo is still not sufficiently well understood to yield accurate calculations in some situations. For instance, Chapman *et al* (2017) showed that neglecting material dependence in the nuclear halo resulted in large dose differences distal to thick heterogeneities, which could potentially be clinically relevant. The physics of material dependence in the nuclear halo has not been well studied and a better understanding would likely yield more accurate analytical dose calculation models. Thus, there is limited but cautionary evidence (Chapman *et al* 2017) suggesting that the nuclear halo may result in large dose errors in some cases, but the clinical significance is not well understood.

In this work, we discuss a stochastically based primary dose model and a novel method for adding robust material dependence to an analytically calculated nuclear halo. Our novel method relied on an improved energy loss calculation that scaled the secondary particle dose resulting from the nuclear halo along all three Cartesian axes, rather than just the typical one-dimensional scaling along depth. This improvement also removes the central-axis approximation from the nuclear halo term, which previous analytical nuclear halo models neglected.

1.5 Hypothesis and Specific Aims

The hypothesis of this work is that a proton dose calculation algorithm can be developed that results in 100% of points below heterogeneities within 3% dose difference or 1 mm distance-to-agreement compared to Monte Carlo simulations. Furthermore, dose difference distal to slab heterogeneities will be within +/-5% in laterally finite geometries and within +/-3% in laterally infinite geometries.

The hypothesis was tested for the following conditions:

1. 250 MeV monoenergetic beam and a spread-out Bragg peak with 5 cm of range modulation.
2. Rectangular field size (4x4 cm^2).
3. Heterogeneities composed of two materials (air, compact bone), and various depths (*z=10, 20, 30* cm) and thicknesses (2, 4, 5 cm).

The hypothesis implies development of a dose model that achieves improved accuracy for proton dose calculations compared to our previous model (Chapman *et al* 2017). The Specific Aims that follow detail the development and evaluation of such a model, in incremental steps. In Specific Aim 1, the focus is on developing a high accuracy primary proton dose calculation, and the increase in accuracy is demonstrated relative to a three-dimensional extension of a pencil beam algorithm, using Monte Carlo data as the standard of comparison. Specific Aim 2 details the improvements made to our previous nuclear halo model, and focus is on the increase in accuracy attained from these improvements relative to the previous nuclear halo model. In Specific Aim 3, the composite dose model (primary + secondary) is evaluated against Monte Carlo simulations in heterogeneity configurations modeled after anatomy encountered in typical clinical scenarios.

1.5.1 Specific Aim 1: Develop and implement a dose calculation algorithm to address the limitations imposed by the central-axis semi-infinite slab approximation

A primary dose calculation algorithm, similar to the model by Tourovsky *et al* (2005), was developed and implemented. This model applied a slab-based approximation (from Z to Z+ΔZ) to individual proton transport that used Monte Carlo simulations and analytical equations, permitting high dose calculation accuracy. This model was compared to both a three-dimensional extension of the Chapman *et al* (2017) pencil beam algorithm and Monte Carlo simulations using MCNPX version 2.7e (Pelowitz 2011), which served as the standard of comparison for both algorithms.

Specific Aim 1 had the following milestones:

1. Demonstrate 3% dose difference or 1 mm distantance-to-agreement in the primary dose only between the present model and MC for 100% of points under the following conditions
    a. Monoenergetic 250 MeV beam.
    b. Rectangular field size (4x4 cm^2).
    c. Homogeneous water phantom.
    d. Geometries with deep (*z=30* cm), thick (4 cm) laterally finite heterogeneies of varying composition (air and compact bone).
2. For the same conditions in (1) for Specific Aim 1, examine dose distal to slab heterogeneities and demonstrate dose difference in the present model compared to MC within +/-5%.

1.5.2 Specific Aim 2: Develop and implement a methodology to include material dependence in the nuclear halo

A novel, simple method for estimating energy lost by secondary protons resulting from the nuclear halo is introduced, which permits lateral scaling in addition to the one-dimensional depth scaling of the water-based nuclear halo model in Chapman *et al* (2017). The novel, simple nuclear halo model in the present work was added to the primary dose model from Specific Aim 1 and compared against MC simulations. To demonstrate the improved modeling in the present work, comparisons were made between the improved nuclear halo model and the previous model (Chapman *et al* 2017).

Specific Aim 2 had the following milestones:

1. Demonstrate 3% dose difference or 1 mm distance-to-agreement in the total dose between the present model and MC for 100% of points under the following conditions:
    a. Monoenergetic 250 MeV beam.
    b. Rectangular field size (4x4 cm^2).
    c. Thick (2, 4, 5 cm), laterally infinite heterogeneities at various depths (*z=10, 20, 30* cm) of varying composition (air and compact bone).
2. For the same conditions in (1) for Specific Aim 2, examine dose distal to slab heterogeneities and demonstrate dose difference in the present model compared to MC within +/-3%.

1.5.3 Specific Aim 3: Quantify improvements made in Specific Aims 1 and 2 in geometries with complex heterogeneities

The dose model developed in Specific Aims 1 and 2 was evaluated in various geometries intended to model anatomy encountered in clinically-relevant scenarios.

Specific Aim 3 had the following milestones:

1. Demonstrate 3% dose difference or 1 mm distance-to-agreement in the total dose between the present model and MC for 100% of points under the following conditions:
    a. Monoenergetic 100 MeV and 250 MeV beam and a spread-out Bragg peak with 5 cm of range modulation.
    a. Rectangular field size (4x4 cm^2).
    b. Various geometries, including:
        i. 2 cm wide by 2 cm thick checkerboard pattern (alternating air and compact bone).
        ii. Prostate phantom, including femoral head (2 cm radius circle of compact bone) and rectum (ellipse of air).
        iii. Paranasal phantom, including numerous compact bone and air heterogeneities and a convex skin surface.

2. For the same conditions in (1) for Specific Aim 3, examine dose distal to heterogeneities and demonstrate dose difference in the present model compared to MC within +/-5%.

CHAPTER 2. DOSE CALCULATION MODEL

2.1 Overview

In this chapter, the new dose calculation model developed in this work is presented. This dose model was designed primarily to resolve the two categories of errors reported in Chapman *et al* (2017): (1) those caused by the pencil-beam central-axis approximation and (2) those caused by neglecting material-dependence in the nuclear halo model. To study these two issues in isolation and find appropriate correction strategies, the present model started with the same two-component dose equation as that from Chapman *et al* (2017):

$$D_{TOTAL}(X_i, Y_j, Z_k) = D_P(X_i, Y_j, Z_k) + D_S(X_i, Y_j, Z_k), \quad (5)$$

where the first term accounts for the "primary" effects on the beam due to energy loss and Coulombic scatter (i.e., MCS and continuous energy loss) from protons which have not been removed from the primary beam, and the second term accounts for the "nuclear halo" of dose deposited by secondary protons and other particles created in non-elastic nuclear interactions. The nuclear halo term in equation (5), $D_S(X_i, Y_j, Z_k)$, can also account for the remaining over- or under-estimated scatter of primary protons in the primary term. Dose terms in equation (5) were computed on a dose grid with 1x1x1 mm^3 resolution, whose coordinates (X_i, Y_j, Z_k) we specify using grid indices $(i,\ j,\ k)$. This nomenclature facilitates discussion of primary transport in the fast Monte Carlo model because it makes the indices of the dose grid (i, j, k) calculation point explicit. The uppercase nomenclature is used for all variables pertaining to the dose grid, whereas lowercase variables are used for variables pertaining to individual protons or pencil beams.

2.2 Primary Proton Dose: The Pencil Beam Algorithm (Fermi-Eyges based)

Before discussing the improved primary dose model, we examine how the pencil beam algorithm from Chapman *et al* (2017) was extended to three dimensions. To avoid extraneous detail and to keep focus on the improvements made in the present model, only modifications made to the primary pencil beam dose equation are presented. Further details relevant to the pencil beam algorithm can be found in Chapman *et al* (2017).

The pencil beam algorithm (PBA) began by segmenting the broad, monoenergetic beam at the field-defining plane into a number of mathematically deconstructed pencil beams of area ΔX by ΔY (Figure 2.1). For

the laterally uniform 4x4 cm^2 fields that were used in our model, each pencil beam therefore modeled some number of protons, $n_{beamlet}$, from the beam. Transport was then accomplished by applying Fermi-Eyges theory (Eyges 1948) to each of these pencil beams. It can be shown that under these conditions, primary dose to material *m* for a beam of field size FS_X by FS_Y at calculation point (X_i, Y_j, Z_k) is given by

$$
\begin{aligned}
D_P^{FS_X,FS_Y}(X_i, Y_j, Z_k) = \\
&\cdot \sum_{l=1}^{n_X} \sum_{m=1}^{n_Y} \left(1 - w_{SG}\left(Z_{eff}^{l,m}(Z_k)\right) - w_{SCL}\left(Z_{eff}^{l,m}(Z_k)\right)\right) \left\{\left[D_{expt}^{SSE}\left(Z_{eff}^{l,m}(Z_k)\right)\right]_w^{FS_X,FS_Y}\right\}_P \\
&\cdot \left(\frac{S}{\rho}\right)_w^{mat}\left(X_i, Y_j, Z_k;\ \bar{E}(x_l, y_m, Z_k)\right) \\
&\cdot \frac{1}{4}\left[\operatorname{erf}\left(\frac{x_l + \frac{\Delta X}{2} - X_i}{\sqrt{2}\,\sigma_P^{l,m}(Z_k)}\right) - \operatorname{erf}\left(\frac{x_l - \frac{\Delta X}{2} - X_i}{\sqrt{2}\,\sigma_P^{l,m}(Z_k)}\right)\right] \\
&\cdot \left[\operatorname{erf}\left(\frac{y_m + \frac{\Delta Y}{2} - Y_j}{\sqrt{2}\,\sigma_P^{l,m}(Z_k)}\right) - \operatorname{erf}\left(\frac{y_m - \frac{\Delta Y}{2} - Y_j}{\sqrt{2}\,\sigma_P^{l,m}(Z_k)}\right)\right],
\end{aligned}
\tag{6}
$$

where $\left(\frac{S}{\rho}\right)_w^{mat}$ denotes the mass stopping power ratio for the material to water at position (X_i, Y_j, Z_k) due to the pencil beam centered at (x_l, y_m) for the mean energy at $\bar{E}(x_l,\ y_m,\ Z_k)$. The mass stopping power ratio essentially converts dose in water to dose in material at the calculation point for comparison to dose values from MC simulations. w_{SG} and w_{SCL} are central-axis weighting factors for the nuclear halo that are defined in section 2.4. $\left\{\left[D_{expt}^{SSE}\left(Z_{eff}^{l,m}(Z_k)\right)\right]_w^{FS_X,FS_Y}\right\}_P$, which is the depth-dose for the primary term in water for which side scatter equilibrium (SSE) has been restored to the central-axis profile of an experimentally determined (in this work, a MC calculation) dose distribution in water for a field size of FS_X by FS_Y,

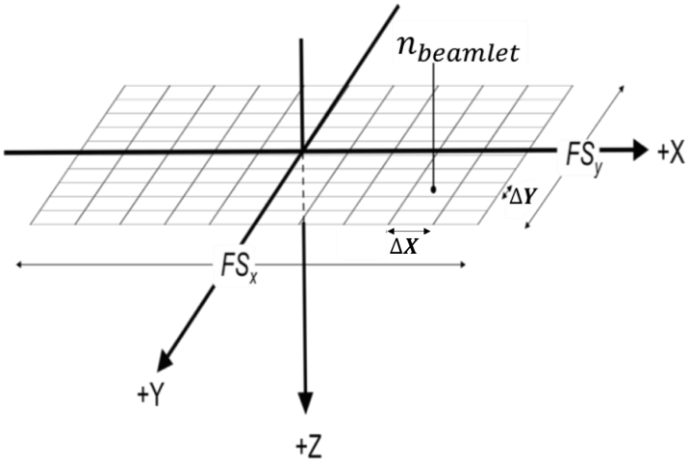

Figure 2.1. A beam with field size FS_X by FS_Y is discretized into beamlets with area ΔX by ΔY. Each beamlet shown, therefore, is representative of some number of protons ($n_{beamlet}$) from the beam.

$$\left\{\left[D_{expt}^{SSE}\left(Z_{eff}^{l,m}(Z_k)\right)\right]_w^{FS_X,FS_Y}\right\}_P = \left[D_{expt}\left(Z_{eff}^{l,m}(Z_k)\right)\right]_w^{FS_X,FS_Y} \cdot \left[\text{erf}\left(\frac{FS_X}{2\sqrt{2}\,\sigma_P^w(Z_{eff}^{l,m}(Z_k))}\right)\right]^{-1}\left[\text{erf}\left(\frac{FS_Y}{2\sqrt{2}\,\sigma_P^w(Z_{eff}^{l,m}(Z_k))}\right)\right]^{-1}, \tag{7}$$

where $\left[D_{expt}(Z_{eff}^{l,m}(Z_k))\right]_w^{FS_X,FS_Y}$ is the central-axis of an experimentally determined dose distribution in water. Dose grid resolution is set equal to the pencil beam width, ΔX and ΔY for the respective axes. The effective depth in water for the pencil beam centered at (x_l, y_m), $Z_{eff}^{l,m}(Z_k)$, given by

$$Z_{eff}^{l,m}(Z_k) = \int_0^{Z_k} S_w^{mat}(x_l, y_m, z')\ dz', \tag{8}$$

is used as shorthand for $Z_{eff}(x_l, y_m, Z_k)$, and $\sigma_P^{l,m}(Z_k)$ is likewise used as shorthand for $\sigma_P(x_l, y_m, Z_k)$ (equation 6). S_w^{mat} denotes the linear stopping power ratio for the material to water. $\sigma_P^w(Z_k)$ is the sigma in a homogeneous water phantom at depth Z_k. Finally, n_X and n_Y refer to the number of pencil beams along the *X* and *Y* axes, respectively, and are given by

$$n_X = \left\lfloor \frac{FS_X}{\Delta X} \right\rfloor \tag{9a}$$

$$n_Y = \left\lfloor \frac{FS_Y}{\Delta Y} \right\rfloor \tag{9b}$$

where the lower half-brackets indicate that the calculations are taken as the integer floor value.

2.3 Primary Proton Dose Model (Specific Aim 1)

The primary dose model in the present work is a class II condensed history Monte Carlo algorithm. Proton transport started from the field-defining plane and continued to depth in the patient. At the field-defining plane, the broad beam is discretized into beamlets of area ΔX by ΔY (Figure 2.2). Note that for this model we refer to the discretized areas as "beamlets" to distinguish them from the PBA, where we called them "pencil beams." Furthermore, by "beamlets" we do not mean to imply that is equivalent to a physical beam spot, but that it is a mathematically deconstructed portion of the broad beam. In this model, transport is carried out proton-by-proton. Because this method of transport does not model groups of protons simultaneously, the central-axis approximation is no longer needed, and the systematic modeling errors therein are eliminated (see section 1.3).

2.3.1 Initial Beam Characteristics

The beams used in the primary dose model were subject to the following assumptions: (1) the beam at the surface of the phantom is parallel; (2) the beam arrives parallel to the Z-axis; and (3) there is no air gap between the beam-defining-plane and the phantom surface (i.e., beamlets were defined directly on the phantom surface). These approximations have a few consequences. Notably, because the beam is modeled directly on the phantom surface and because the beam is parallel, there is no need to include a phase space model or perform beam divergence and field size corrections. For simplicity, we designed the dose model irrespective of any commercially available initial beam configuration. Adaptation of the model to relax these assumptions would be straightforward.

The beam in the primary dose model had the following user-defined parameters: (1) number of particles (NPS), which sets the initial number of protons (see section 2.3.4); (2) incident nominal energy (E_{nom}), which is used to calculate energy-specific parameters needed by the dose calculation; (3) rectangular field size (FS_X and FS_Y), which sets the lateral bounds of the beam; and, (4) sigma of the initial energy distribution (σ_E), which sets the bounds of variation on energies randomly selected at the beam-defining plane.

To ensure particles were uniformly spread in the beam-defining plane, each beamlet of area ΔX by ΔY (Figure 2.2) was divided into its own rectangular grid (the "beamlet" grid) with an equal number of particles (2,500) spread across every grid pixel. Thus, initial particle positions were chosen systematically rather than relying on random assignment. This systematic assignment resulted in sufficiently close particle spacing (0.002 cm) compared to the lateral scattering, so no difference was expected compared to random position assignment.

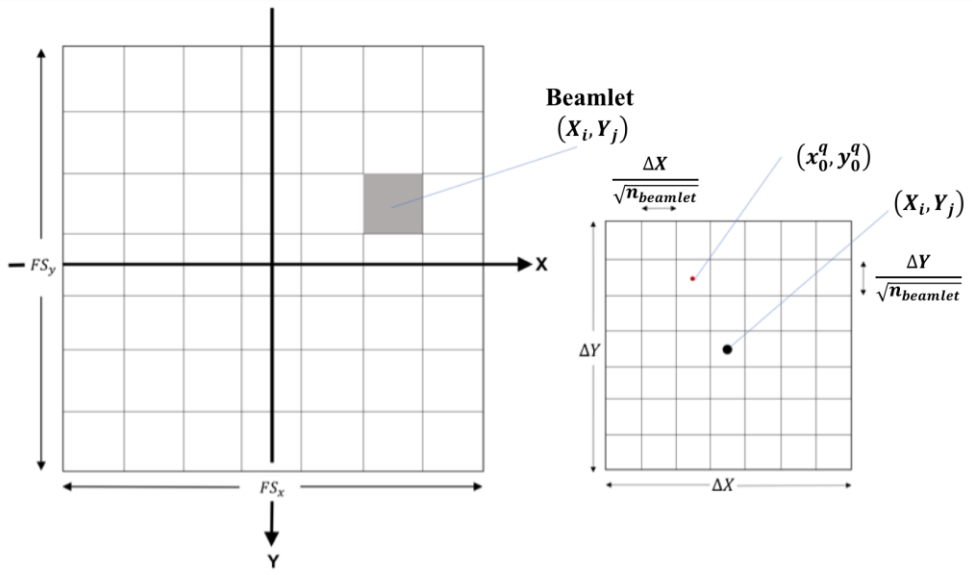

(a) (b)

Figure 2.2. Grids used to determine initial coordinates for particles. Beamlet (X_i, Y_j) is indicated in (a) as the grey square and the sub-grid for this beamlet is shown in (b). $n_{beamlet}$ particles (equation 10) are uniformly spread over the area ΔX by ΔY using the beamlet grid in (b). In (b), the initial position for one such particle, particle q is shown.

The procedure for ensuring uniform coverage of particles relied on binning equal numbers of particles uniformly across the field and forcing equal spacing of particles in each bin (Figure 2.2). Given NPS initial particles assigned to a beam of field size FS_X by FS_Y, each beamlet of area ΔX by ΔY received an equal share of particles $n_{beamlet}$,

$$n_{beamlet} = NPS \ \text{int}\left(\frac{\Delta X \, \Delta Y}{FS_X \, FS_Y}\right), \tag{10}$$

where "int" indicates the expression is cast to an integer result. Our model was only tested with a square field (*i.e.*, FS_X=FS_Y); thus, the spacing of the $n_{beamlet}$ particles in each beamlet was $\delta x = \Delta X/\sqrt{n_{beamlet}}$ along the

X-axis, and $\delta y = \Delta Y/\sqrt{n_{beamlet}}$ along Y. The final equations for initial coordinates of particle q within beamlet (i, j) are therefore given by

$$x_0^q = X_i - \frac{\Delta X}{2} + n_1\,\delta x, \quad n_1 = 1,2,\ldots,\sqrt{n_{beamlet}}, \tag{11a}$$

$$y_0^q = Y_j - \frac{\Delta Y}{2} + n_2\,\delta y, \quad n_2 = 1,2,\ldots,\sqrt{n_{beamlet}}, \tag{11b}$$

where the lowercase variables x_0^q and y_0^q refer to the initial position of the particle at the phantom surface (note that typically x_k^q and y_k^q are used, but at the beam-defining plane, *k=0*), and the uppercase variables X_i and Y_j refer to center coordinates of pixel (i, j). Furthermore, pixel spacing in the dose grid is indicated by ΔX and ΔY.

Finally, each proton at the beam-defining plane was initialized with an energy randomly sampled from a Gaussian to model energy straggling, given by

$$G(E)dE = \frac{1}{\sqrt{2\pi}\,\sigma_E}\exp\left[\frac{-(E-E_{nom})^2}{2\,\sigma_E^2}\right]dE. \tag{12}$$

To generate the independent random variable needed to sample from equation (12), the Box-Mueller transform (Box and Mueller 1958) was used. This approach takes two independent, random uniform random variables (U_1, U_2), on the range (0,1) and transforms them to two independent, normal random variables (N_1, N_2), again on the range (0,1). Thus, according to the Box-Mueller, transform,

$$N_1 = \sqrt{-2\ln(U_1)}\cos(2\pi\,U_2), \tag{13a}$$

$$N_2 = \sqrt{-2\ln(U_1)}\sin(2\pi\,U_2). \tag{13b}$$

Because (N_1, N_2) are independent, normal random variables (i.e., continued sampling would yield a distribution with a mean value of zero and unity variance), (N_1, N_2) can be transformed to (G_1, G_2) (i.e., two independent, random Gaussian samples from equation 12) using

$$G_1 = E_{nom} + \sigma_E N_1, \tag{14a}$$

$$G_2 = E_{nom} + \sigma_E N_2, \tag{14b}$$

where G_1 and G_2 are two independent, random Gaussian samples from equation (12). This approach was verified to reproduce the expected distribution using multiple test simulations.

2.3.2 Transport Geometry

Each proton, initialized as described in the previous section, was then transported through the calculation geometry. Figure 2.3 shows a representative schematic of a single proton track in our primary dose model. The parameters that characterize the proton transport are updated every "step" of thickness ΔZ. For proton q transported to depth Z_k, several parameters must be updated for our dose model: (1) position $\left(x_k^q, y_k^q\right)$, (2) energy $\left(E_k^q\right)$, (3) MCS scatter angles (α, β) and exit direction $\left(\theta_k^q, \phi_k^q\right)$, and (4) effective depth in water $\left(\left[Z_{eff}\right]_k^q\right)$. The circled area in Figure 2.3 is diagrammed in greater detail in Figure 2.4.

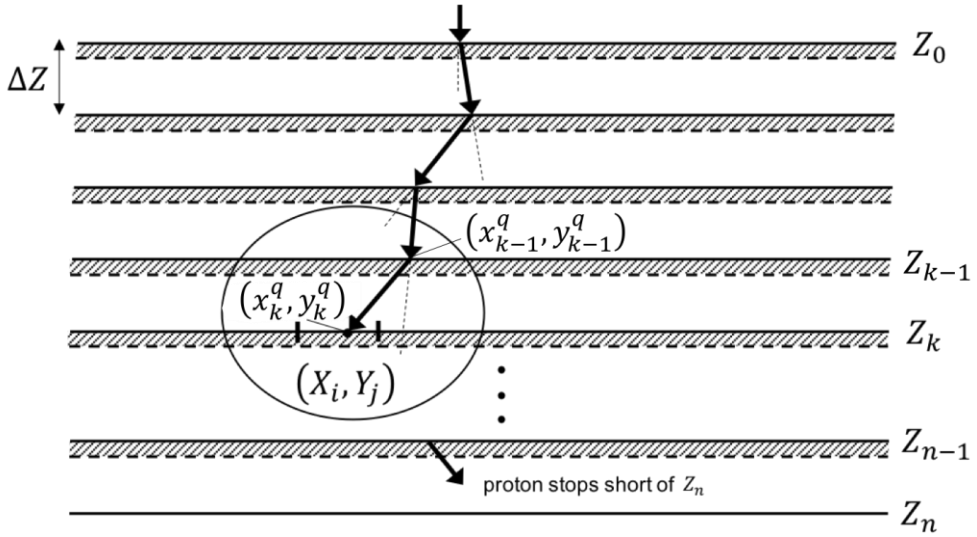

Figure 2.3. Schematic of a typical proton track. Proton q is shown entering the geometry at Z_0 with normal incidence and scattering at small step intervals of ΔZ. For each scatter event, the thickness ΔZ is approximated as a small, infinitesimally thick slab (shaded areas, see Figure 2.4), which simplifies transport calculations. Once the position of proton m is calculated at Z_k, the corresponding pixel coordinates (X_i, Y_j) in the dose grid must be found to accumulate dose. The circled area is more closely examined in Figure 2.4.

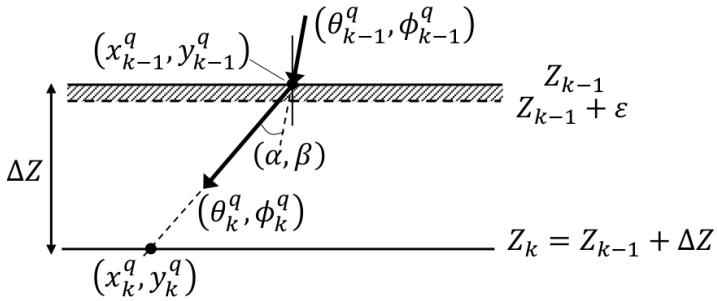

Figure 2.4. Each step ΔZ in the track for proton q is approximated as an infinitesimally thick, semi-infinite slab with thickness $\varepsilon \to 0$. Thus, the complex path that proton q experiences in the thickness ΔZ can be approximated by a single MCS scatter event in the thickness ε. Given that proton q enters this step with direction $\left(\theta_{k-1}^q, \phi_{k-1}^q\right)$, the MCS scatter angles (α, β) are used to calculate the exit direction $\left(\theta_k^q, \phi_k^q\right)$.

One of the most important considerations in a dose model is the determination of the locations to deposit dose. For each proton track, this information is given by the position of the proton for each step in the track. In an arbitrary step of the track, proton q enters with position $\left(x_{k-1}^{q}, y_{k-1}^{q}\right)$ at depth Z_{k-1} and at depth Z_k, the position is given by

$$x_k^q = x_{k-1}^q + \Delta \mathrm{Z}\ \tan\theta_k^q \cos\phi_k^q, \tag{15a}$$

$$y_k^q = y_{k-1}^q + \Delta \mathrm{Z}\ \tan\theta_k^q \sin\phi_k^q. \tag{15b}$$

This updated position depends on the exit direction $\left(\theta_k^q, \phi_k^q\right)$ for this step. For this transport step, the proton may experience numerous scatter events that result in a complex path. To address this problem, we approximated the slab as an infinitesimally small ($\varepsilon \to 0$), semi-infinite slab (Figure 2.4) located near the entrance to the slab ($Z_{k-1} + \varepsilon$), which allows the use of thin-target multiple Coulomb scatter (MCS) theory. Thus, in each step of the proton trajectory, the scatter is calculated using MCS theory, which we specify using spherical angles (α, β). As can be seen in Figure 2.4, due to the infinitesimal slab, the exit direction is a function of both the entrance direction $\left(\theta_{k-1}^q, \phi_{k-1}^q\right)$ and the MCS scatter angles (α, β) with respect to the entrance direction, such that

$$\theta_k^q = \cos^{-1}\left\{\cos\alpha\cos\theta_{k-1}^q + \sin\alpha\cos\beta\sin\theta_{k-1}^q\right\}, \tag{16a}$$

$$\phi_k^q = \widetilde{\tan}^{-1}\left\{\frac{\cos\alpha\sin\theta_{k-1}^q\sin\phi_{k-1}^q - \sin\alpha\left[\cos\beta\cos\theta_{k-1}^q\sin\phi_{k-1}^q - \sin\beta\cos\phi_{k-1}^q\right]}{\cos\alpha\sin\theta_{k-1}^q\cos\phi_{k-1}^q - \sin\alpha\left[\cos\beta\cos\theta_{k-1}^q\cos\phi_{k-1}^q + \sin\beta\sin\phi_{k-1}^q\right]}\right\}, \tag{16b}$$

where the ~ over the arc-tangent operation indicates that the result is returned in the proper quadrant (most software packages refer to this function as *atan2*). Equations (16a-b) describe both the angles leaving the current slab and the angles entering the next slab, i.e. proton q drifts from $Z_{k-1} + \varepsilon$ to $Z_{k-1} + \Delta Z$.

In order to quantify primary scatter angles within the slab (α, β), it is necessary to assume that the particles follow some distribution. In this model, we use a Gaussian to sample the polar angle:

$$f(\alpha) = \frac{\alpha}{\sigma_\alpha^2}\exp\left[-\frac{\alpha^2}{2\,{\sigma_\alpha}^2}\right]. \tag{17}$$

Using the conservation of probability to relate this Gaussian with a uniformly distributed random number (0,1), it can be shown that the polar scattering angle α can be sampled using the following equation:

$$\alpha = \sigma_\alpha \sqrt{-2\ln(U_\alpha)}, \tag{18}$$

where U_α is an independent uniformly distribution random number over the interval [0, 1]. Furthermore, according to MCS theory, σ_α can be calculated in the following way

$$\sigma_\alpha^2(X_i, Y_j, Z_k) = \frac{1}{2}\, T(E_k^m)\, \left(\frac{\Delta Z}{\cos\theta_k^m}\right), \tag{19}$$

where T is the linear angular scattering power (explained in the next section). Finally, azimuthal symmetry gives

$$\beta = 2\pi\, U_\beta, \tag{20}$$

where U_β is an independent uniformly distributed random number over the interval [0,1].

Having found all the geometric parameters necessary to calculate the position of proton q at depth Z_k, (x_k^q, y_k^q), the corresponding coordinates of the pixel in the dose grid, (X_i, Y_j), are found (see circled area in Figure 2.3). For $X_i - \frac{\Delta X}{2} \le x_k^q \le X_i + \frac{\Delta X}{2}$ and $Y_j - \frac{\Delta Y}{2} \le y_k^q \le Y_j + \frac{\Delta Y}{2}$, the primary dose contribution of proton q to (X_i, Y_j, Z_k) is given by

$$\left[D(X_i, Y_j, Z_k)\right]_P = \left[D(X_i, Y_j, Z_k)\right]_P + \frac{1}{\Delta X\, \Delta Y\, \cos\theta_k^q}\, \frac{S_{mat}}{\rho}(E_k^q)\, C\left(\left[Z_{eff}\right]_k^q;\, E_0^q\right), \tag{21}$$

where the 'P' subscript indicates that this refers to primary dose only, and $\left[D(X_i, Y_j, Z_k)\right]_P$ on the right-hand side refers to the previous value of $\left[D(X_i, Y_j, Z_k)\right]_P$. $C\left(\left[Z_{eff}\right]_k^q;\, E_0^q\right)$ is the correction factor for all remaining unmodeled physics, including the fluence loss due to nonelastic nuclear interactions (section 2.3.3), S_{mat}/ρ is the mass stopping power in the material, E_k^q refers to the energy of proton q at depth Z_k, and θ_k^q is the polar spherical angle of the proton track from the beam axis in a spherical coordinate system.

2.3.3 Selection of Parameters

In this section, the focus will be on the selection of those parameters that describe physical interactions of the proton. As mentioned in Chapter 1, there are three major categories of interactions that need to be included in a proton dose calculation model for the primary beam: (1) energy loss, (2) scatter, and (3) fluence loss of primary protons due to nonelastic nuclear interactions.

Energy loss for primary protons in our dose model is calculated using the continuous slowing down approximation (CSDA), which for proton q at depth Z_k, is calculated using

$$E_k^q \approx E_{k-1}^q - \left(\frac{\Delta Z}{\cos\theta_k^q}\right) S_{mat}\left(E_{k-1}^q\right), \tag{22}$$

where E_{k-1}^q refers to the energy of the proton at depth Z_{k-1} and E_k^q is the energy at Z_k, and S_{mat} is the stopping power of the material at (X_i, Y_j, Z_k) and at energy E_{k-1}^q. Note that equation (22) is approximate because the linear stopping power at energy E_{k-1}^q is used rather than the average stopping power over the step. Another measure of energy loss is the effective depth in water, given by

$$\left[Z_{eff}\right]_k^q = \left[Z_{eff}\right]_{k-1}^q + \left(\frac{\Delta Z}{\cos\theta_k^q}\right) S_w^{mat}\left(E_{k-1}^q\right), \tag{23}$$

where S_w^{mat} refers to the ratio of the linear collisional stopping power in the material at (X_i, Y_j, Z_k) to the linear collisional stopping power in water at energy E_{k-1}^q.

The equations for both E_k^q and $\left[Z_{eff}\right]_k^q$ require accurate determination of stopping power data. The required stopping powers in water were looked up from a table of values calculated before proton transport took place. This approach was preferred over using databases, such as SRIM (Ziegler *et al* 2012), because the computation of tabular data was based on an analytical formula (equation 25) which allowed variable energy resolution. To compute the stopping power table for water, three additional user-defined parameters are required: the maximum energy (E_{max}), the energy resolution (f_E), and the cutoff energy (E_{cut}). The energy array is then calculated using

$$E_h = f_E\, E_{h-1}, \tag{24}$$

where h is initialized to 1 and E_0=E_{max}. Using this set of energies, the corresponding stopping powers in water is then computed using the following analytical formula

$$\frac{S}{\rho}(E) = \frac{1}{a_1 a_2 E^{a_2-1} + a_3 a_4 E^{a_4-1} + a_5(\exp[a_6 E] - 1)}, \tag{25}$$

where a_1 through a_6 are material-specific parameters fit to SRIM data (Table 2.1) over the energy range 10 keV to 300 MeV; the fitting used a genetic algorithm (Donahue *et al* 2016).

Table 2.1. Parameters for equation (25) using Donahue *et al* (2016) for the three materials in this study.

Name	Analytical Stopping Power Parameters (Donahue *et al* 2016)					
	a_1	a_2	a_3	a_4	a_5	a_6
Air, Dry (ICRU-104)	0.22635	0.31744	1.20178	1.63921	176.54209	-0.00399
Water, Liquid (ICRU-276)	0.00016	0.31224	0.00098	1.58180	0.17113	-0.00400
Bone, Compact (ICRP)	0.00027	0.23111	0.00174	1.53310	0.32531	-0.00389

In order to calculate stopping power in non-water materials, we used equation (25) to determine stopping power ratios between the material of interest and water. The dose model included three biological materials (Table 2.2). The compositions listed in the table are from *ICRU* (1989) (air and water) and ICRP (1975) (compact bone) and match the compositions found in SRIM. A number of representative points from these stopping power ratios were chosen as a function of depth and stored as a lookup table as a function of energy (mass stopping power ratios shown in Figure 2.5), and intermediate values were linearly interpolated. Thus, to calculate the stopping power in any of the materials used in this work, we used the following equation

$$S_{mat}(E) = S_w^{mat}(E)\, S_{water}(E), \tag{26}$$

where S_{mat} is the linear collisional stopping power in the material, S_{water} is the linear collisional stopping power in water, and $S_w^{mat}(E)$ is the ratio of linear collisional stopping power in material to water at E.

Table 2.2. Composition of the three materials used in this study.

Name	Rho (g/cc)	Fraction by Mass (%)								
		H	C	N	O	Mg	P	S	Ar	Ca
Air, Dry (ICRU-104)	1.63E-03	0	0.02	75.51	23.18	0	0	0	1.29	0
Water, Liquid (ICRU-276)	1	11.19	0	0	88.81	0	0	0	0	0
Bone, Compact (ICRP)	1.85	6.4	27.8	2.7	41	0.2	7	0.19	0	14.7

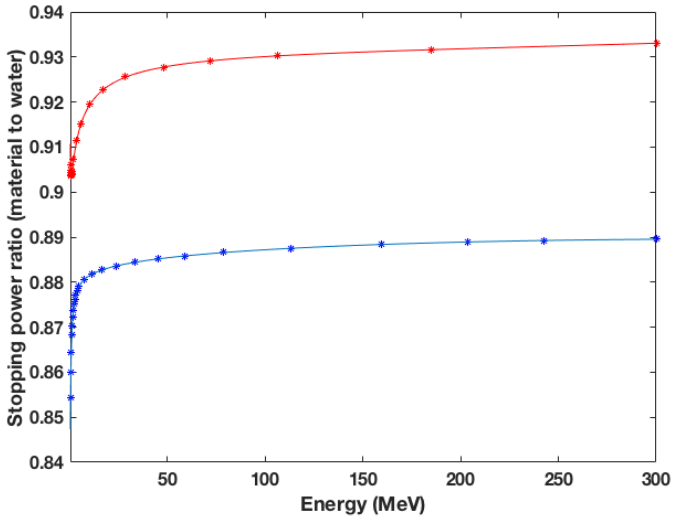

Figure 2.5. Mass stopping power ratios vs energy shown for air-to-water (blue) and compact bone-to-water (red). Mass stopping power ratios are shown rather than linear stopping power ratios to avoid the large variation in density. f_E=*0.99* is used in equation (24) for the data shown, with the representative points used in the final code indicated with asterisks (*).

Proton scatter was discussed in the previous section, and it was seen that the sigma for the MCS scatter angle α (equation 19) was dependent on a quantity called the linear angular scattering power (equation 27). There are several scattering power formulae available for protons (Gottschalk 2010), but the only one derived from Moliere theory (which is considered the most accurate scatter theory) is the differential Moliere scattering power, which has the form

$$T_{dM} = f_{dM}(pv, pv_0)\left(\frac{E_s}{pv}\right)^2 \frac{1}{X_s}, \tag{27}$$

where f_{dM} is called the single scattering correction (found in Gottschalk 2010). Other parameters in equation (27) include the constant $E_s = 15\ MeV$, pv is the product of momentum and velocity at the point of interest, pv_0 is the same product at the initial energy, and X_s, which is defined as

$$\frac{1}{X_s} = \alpha_{fs} N_A r_e^2 \rho \frac{Z^2}{A}\left\{2\ln\left(33219(ZA)^{-1/3}\right) - 1\right\}, \tag{28}$$

where $\alpha_{fs} = 1/137$ is the fine-structure constant, $N_A = 6.022x10^{23}\ mol^{-1}$ is Avogadro's number, and $r_e = 2.818x10^{-13}\ cm$ is the classical electron radius. The linear angular scattering power (27) was calculated for the three materials listed in Table 2.2.

The last major interaction that needs to be discussed for this primary dose model is the fluence loss of primary protons resulting from non-elastic nuclear interactions. This interaction is not calculated while the proton is transported, unlike the previously mentioned proton track parameters. Instead, fluence loss is handled using tabular data obtained from Monte Carlo simulations. This approach allows a simple, computationally inexpensive table lookup to determine fluence loss for the primary beam. This approach results in a reduced subset of physical interactions in our model, which is one of the primary reasons that our model is fast. In contrast, general purpose MC include an extensive set of interaction types that often result in long calculation times. Modeling fluence loss with tabular data in our model also improves computational efficiency over dose models with stochastic nuclear halos (Fippel and Soukup 2004, Jia *et al* 2012, Qin *et al* 2016, Souris *et al* 2016), which relied on evaluating cross sections and stochastic secondary proton transport. This approach was also more computationally efficient than the analytical nuclear halo approach by Tourovsky *et al* (2005), which also relied on evaluating cross section data.

The procedure for characterizing fluence loss required two simulations: (1) simulation of the *primary* proton dose (i.e., no nuclear halo included) at point (X_i, Y_j, Z_k) for beam with incident energy E_0 in water using our present model, $\left[D_P^w(X_i, Y_j, Z_k;\ E_0)\right]_{PM}$, and (2) an MCNPX simulation of the *total* dose under the same conditions, $\left[D_{Tot}^w(X_i, Y_j, Z_k;\ E_0)\right]_{MC}$. To calculate fluence loss using these datasets, however, the beam must be sufficiently broad to not be impacted by loss of side-scatter equilibrium, so that scatter is not accounted for twice; thus, we instead equated the integral doses $[IDD_{Tot}^w(Z_k;\ E_0)]_{MC} = \int_{X'}\int_{Y'}\left[D_{Tot}^w(X_i, Y_j, Z_k;\ E_0)\right]_{MC}\ dX'dY'$ and $[IDD_P^w(Z_k;\ E_0)]_{PM} = \int_{X'}\int_{Y'}\left[D_{Tot}^w(X_i, Y_j, Z_k;\ E_0)\right]_{PM}\ dX'dY'$. Thus, $C(Z_k; E_0)$, the fluence loss correction factor, is given by

$$C(Z_k; E_0) = \frac{[IDD_{Tot}^w(Z_k;\ E_0)]_{MC}}{[IDD_{Tot}^w(Z_k;\ E_0)]_{PM}}. \tag{29}$$

After $C(Z_k; E_0)$ has been calculated, a number of representative points are chosen as a function of depth and stored as a lookup table for energy E_0 in the primary dose model program, giving the discrete distribution

$C^*(Z_k; E_0)$. A plot showing both $C^*(Z_k; 250\ \text{MeV})$ and $C(Z_k; 250\ \text{MeV})$ is in Figure 2.6. Using the same procedure, $C^*(Z_k; E_0)$ was calculated for two nominal energies $E_0 = \{100, 250\}\ MeV$, and intermediate energies are calculated by linear interpolation over nominal energy. Note that in equation (21), we use $C\left(\left[Z_{eff}\right]_k^q;\ E_0^q\right)$; thus, the correction factor is scaled to the material of interest by the effective depth in water. Thus, for the primary fluence loss, we still relied on a one-dimensional scaling based on the effective depth in water.

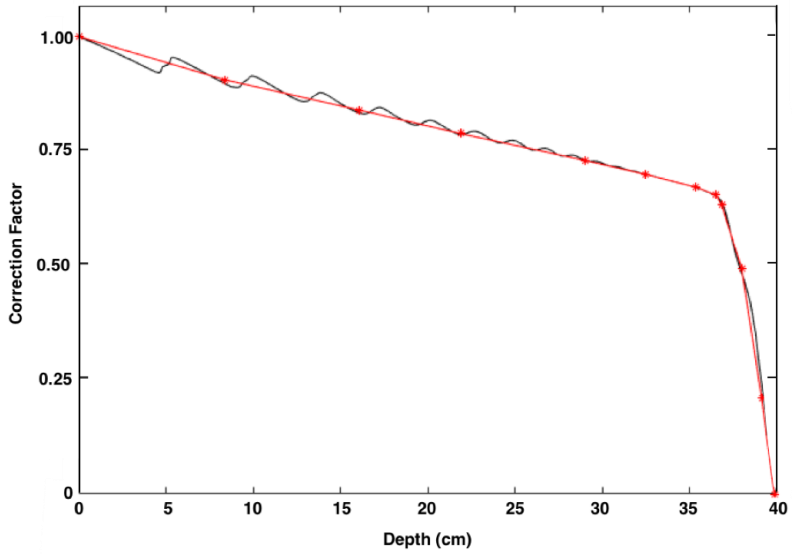

Figure 2.6. Plot comparing $C(Z_k; 250\ \text{MeV})$ (black) and $C^*(Z_k; 250\ \text{MeV})$ (red *).

2.3.4 Statistical Requirements

The primary dose model follows individual proton tracks over discrete steps in the phantom, which is expected to produce more accurate dose calculations compared to a purely analytical approach, such as a pencil beam algorithm (PBA). However, it is necessary to impose requirements on the number of particles simulated in order to ensure a desired level of statistical accuracy. The required number of protons per pixel in the beam-defining plane to achieve a desired statistical percentage accuracy of *u%* is given by:

$$n_{beamlet} = (u/100)^{-2}. \tag{30}$$

In this model, a statistical accuracy of 2% was used, yielding 2,500 particles per pixel in the beam-defining plane; hence, for a broad beam with field size FS_X by FS_Y and XY dose grid resolution ΔX by ΔY, the total number of particles required is

$$NPS = (u/100)^{-2} \frac{FS_X\, FS_Y}{\Delta X\, \Delta Y}. \quad (31)$$

An additional factor that must be taken into consideration is how the stopping power is sampled. Because we are using the CSDA to calculate stopping power, the precision of this calculation is inherently limited by the finite step size. For example, using a constant step size, it is possible to adequately sample the slowly varying entrance region of the stopping power curve, yet miss the rapidly changing features of the peak (reference Figure 1.2). One early approach we had to this problem involved ensuring the percent difference in linear stopping power between consecutive steps did not exceed some chosen percentage, which was typically set to 5%. However, we found that this adaptive step size calculation required excessive calculation time, so we instead chose to calculate on a grid using 0.1 cm steps from the surface to 77% of the range in water, with the step size decreasing to 0.025 cm steps beyond that. Selection of the value for the step size change (77%) was based on repeated simulations in water over a wide energy range (100-250 MeV) by comparing the agreement between the simulation of the present model and MC data. In these repeated simulations, the threshold depth for the change in step size was varied; ultimately, 77% of the range in water was selected as a compromise between agreement at the peak and extended calculation time due to the finer grid spacing in the depth direction. Additionally, in this calculation, a form of Geiger's rule was used to calculate range based on the nominal energy of the beam, as in $R_0^w(cm) = 2.2x10^{-3}(E_0(MeV))^{1.77}$ in water. Despite the use of the variable step size in our transport, the final dose was still accumulated in a dose grid with constant step size $\Delta Z = 0.1\ cm$.

2.3.5 Description of Evaluation Geometries

Our previous study showed that one of the major effects impacting the accuracy of analytical dose calculations was the CAXSIS approximation, which is particularly important for the primary proton dose calculation. The primary dose calculation presented in this chapter is intended to solve the limitations of the CAXSIS approximation. Thus, to assess the performance of the model we examined those geometries where the limitations of the CAXSIS approximation were found to be the most severe.

The evaluation scenarios focused on the highest energy (250 MeV), a rectangular field size (4x4 cm^2), and deep (Z=30 cm), thick (4 cm) heterogeneous slabs. As in our previous study, we tested the range of materials found in patient data by evaluating our model in both compact bone and air slabs. The slabs only extended over half of the calculation geometry because that is the most challenging scenario for the CAXSIS approximation. An evaluation in homogeneous water was also tested to ensure that our model could still calculate in simple geometries.

2.4 Secondary Proton Dose: The "Nuclear Halo" (Specific Aim 2)

In this section, we discuss the nuclear halo equation in the Chapman *et al* (2017) model (hereafter, the "original" model) and the modeling improvements made in the present work to achieve higher dosimetric accuracy in heterogeneous geometries. The original dose model only calculated the nuclear halo in water and scaled to other materials by using a simple one-dimensional effective depth calculation along the pencil-beam central-axis. In discussing how to improve the modeling of the material dependence in the nuclear halo, we note that the three following effects would ideally be incorporated into the model: (1) scaling dose in water to dose in the material of interest at the calculation point; (2) energy loss of the scattered secondary particles throughout the geometry; and (3) number of secondary protons produced, which is a function of both primary proton energy and material. Our solution in Specific Aim 2 addresses the first two of these effects (section 2.4.2). The specifics of how these improvements were added into the nuclear halo model are discussed in section 2.4.3.

2.4.1 Chapman *et al* (2017) Nuclear Halo Equation

In a previous publication (Chapman *et al* 2017), we presented the original nuclear halo model that was used in our proton dose pencil beam algorithm (PBA). The equation used for the nuclear halo was modeled empirically with coefficients determined by fitting the model to MC simulations of lateral dose profiles of a 0.1x0.1 cm^2 pencil beam of protons in water. It was found that the best fit was obtained by a sum of a Gaussian and a modified Cauchy-Lorentz term:

$$D_S^{FS_X,FS_Y}(X_i,Y_j,Z_k) = D_{SG}^{FS_X,FS_Y}(X_i,Y_j,Z_k) + D_{SCL}^{FS_X,FS_Y}(X_i,Y_j,Z_k), \quad (32)$$

where $D_S^{FS_X,FS_Y}$ is the total secondary dose for the field size FS_X by FS_Y. The remaining two terms have the following form:

$$D_{SG}^{FS_X,FS_Y}(X_i,Y_j,Z_k) = \sum_{l=1}^{n_X}\sum_{m=1}^{n_Y} w_{SG}\left(Z_{eff}^{l,m}(Z_k)\right)\left\{\left[D_{expt}^{SSE}\left(Z_{eff}^{l,m}(Z_k)\right)\right]_w^{FS_X,FS_Y}\right\}_{SG}.\left(\frac{S}{\rho}\right)_w^{mat}\left(X_i,Y_j,Z_k;\ \bar{E}(x_l,y_m,Z_k)\right) .\frac{1}{4}\left[\operatorname{erf}\left(\frac{x_l+\frac{\Delta X}{2}-X_i}{\sqrt{2}\,\sigma_{SG}^{l,m}\left(Z_{eff}^{l,m}(Z_k)\right)}\right)-\operatorname{erf}\left(\frac{x_l-\frac{\Delta X}{2}-X_i}{\sqrt{2}\,\sigma_{SG}^{l,m}\left(Z_{eff}^{l,m}(Z_k)\right)}\right)\right] .\left[\operatorname{erf}\left(\frac{y_m+\frac{\Delta Y}{2}-Y_j}{\sqrt{2}\,\sigma_{SG}^{l,m}\left(Z_{eff}^{l,m}(Z_k)\right)}\right)-\operatorname{erf}\left(\frac{y_m-\frac{\Delta Y}{2}-Y_j}{\sqrt{2}\,\sigma_{SG}^{l,m}\left(Z_{eff}^{l,m}(Z_k)\right)}\right)\right], \tag{33a}$$

$$D_{SCL}^{FS_X,FS_Y}(X_i,Y_j,Z_k) = \sum_{l=1}^{n_X}\sum_{m=1}^{n_Y} w_{SCL}\left(Z_{eff}^{l,m}(Z_k)\right)\left\{\left[D_{expt}^{SSE}\left(Z_{eff}^{l,m}(Z_k)\right)\right]_w^{FS_X,FS_Y}\right\}_{SCL}.\left(\frac{S}{\rho}\right)_w^{mat}\left(X_i,Y_j,Z_k;\ \bar{E}(x_l,y_m,Z_k)\right) .\frac{1}{4}\left[\operatorname{atan}\left(\frac{x_l+\frac{\Delta X}{2}-X_i}{\sigma_{SCL}^{l,m}\left(Z_{eff}^{l,m}(Z_k)\right)}\right)-\operatorname{atan}\left(\frac{x_l-\frac{\Delta X}{2}-X_i}{\sigma_{SG}^{l,m}\left(Z_{eff}^{l,m}(Z_k)\right)}\right)\right] .\left[\operatorname{atan}\left(\frac{y_m+\frac{\Delta Y}{2}-Y_j}{\sigma_{SG}^{l,m}\left(Z_{eff}^{l,m}(Z_k)\right)}\right)-\operatorname{atan}\left(\frac{y_m-\frac{\Delta Y}{2}-Y_j}{\sigma_{SG}^{l,m}\left(Z_{eff}^{l,m}(Z_k)\right)}\right)\right], \tag{33b}$$

where w_{SG}, w_{SCL}, σ_{SG}, and σ_{SCL} are left as free parameters of the model. n_X and n_Y refer to the number of pencil beams along the *X* and *Y* axes, respectively. Note the inclusion of the mass stopping power ratio, $\left(\frac{S}{\rho}\right)_w^{mat}$, addresses the need for calculating dose in the material of interest at the calculation point. Additionally, $\sigma_{SG}^{l,m}\left(Z_{eff}^{l,m}(Z_k)\right)$ and $\sigma_{SCL}^{l,m}\left(Z_{eff}^{l,m}(Z_k)\right)$ are used as shorthand for $\sigma_{SG}\left(x_l,y_m,Z_{eff}^{l,m}(Z_k)\right)$ and, $\sigma_{SCL}\left(x_l,y_m,Z_{eff}^{l,m}(Z_k)\right)$ respectively. The side-scatter equilibrium corrections for the central-axis terms were given by

$$\left\{\left[D_{expt}^{SSE}\left(Z_{eff}^{l,m}(Z_k)\right)\right]_w^{FS_X,FS_Y}\right\}_{SG} = \left[D_{expt}\left(Z_{eff}^{l,m}(Z_k)\right)\right]_w^{FS_X,FS_Y} \operatorname{erf}\left[\frac{FS_X}{2\sqrt{2}\,\sigma_{SG}^{w}(Z_{eff}^{l,m}(Z_k))}\right]^{-1}\operatorname{erf}\left[\frac{FS_Y}{2\sqrt{2}\,\sigma_{SG}^{w}(Z_{eff}^{l,m}(Z_k))}\right]^{-1}, \tag{34a}$$

$$\left\{\left[D_{expt}^{SSE}\left(Z_{eff}^{l,m}(Z_k)\right)\right]_w^{FS_X,FS_Y}\right\}_{SCL} = \left[D_{expt}\left(Z_{eff}^{l,m}(Z_k)\right)\right]_w^{FS_X,FS_Y} \operatorname{atan}\left[\frac{FS_X}{2\,\sigma_{SCL}^w(Z_{eff}^{l,m}(Z_k))}\right]^{-1} \operatorname{atan}\left[\frac{FS_Y}{2\,\sigma_{SCL}^w(Z_{eff}^{l,m}(Z_k))}\right]^{-1}. \quad (34b)$$

A least-squares fit was performed in water to determine the free parameters in the model as a function of depth. For all proton energies used in this study, the MC data from simulations of a 0.1x0.1 cm^2 pencil beam in water was used to parameterize the nuclear halo model. The MC data was calculated on a 0.025x0.025 cm^2 grid and spanned large lateral distances (+/- 10 cm off-axis) to characterize the off-axis distributions.

For the fitting procedure, MCNPX (Pelowitz 2011) simulations were used to generate a 0.1x0.1 cm^2 pencil beam of protons in water for two initial energies (100 and 250 MeV). Because the initial field size of 0.1x0.1 cm^2 was small compared to the lateral scattering of the pencil beam at depth, these simulations were treated as a single pencil beam; thus, the free parameters of our model were fit to equations 32-34 with $x_l = y_m = 0$, $n_x = n_y = 1$, $Z_{eff}^{l,m}(Z_k) = Z_k$, $\sigma_{SG}^{l,m} = \sigma_{SG}^w$, $\sigma_{SCL}^{l,m} = \sigma_{SCL}^w$, and $\left(\frac{S}{\rho}\right)_w^{mat} = 1$.

2.4.2 Improved Energy Loss Calculation

Although material dependence was included to some extent in the equations presented in the previous section, Chapman *et al* (2017) indicated that a more robust material dependence would further improve agreement with MC simulations.

The prior nuclear halo model (equations 32-34) only accounted for energy loss along the central-axis of the pencil beam via the effective depth in water. Because we are trying to model the energy loss of secondary protons, which lose energy over more complex paths than the pencil-beam central-axis, we instead used a water-equivalent calculation from the pencil beam at its origin to the point of interest. Figure 2.7(a) illustrates the proposed scenario in an example phantom that includes a bone slab in an otherwise homogeneous water geometry. To avoid cumbersome three-dimensional diagrams, we use the polar variable *R* to indicate transverse distance from the central-axis of the pencil beam; the more conventional Cartesian *X* and *Y* parameters can be easily obtained from this value.

The core idea of adding the new effective path calculation is that it defines a path in three-dimensional space which allows scaling of the fitted halo data in water for all three coordinate axes. In Figure 2.7(a), the intended calculation point, *P*, is shown in the phantom geometry. The objective for the new, three-dimensional approach is to transform point in the phantom geometry to a point described by effective coordinates in the water-equivalent geometry.

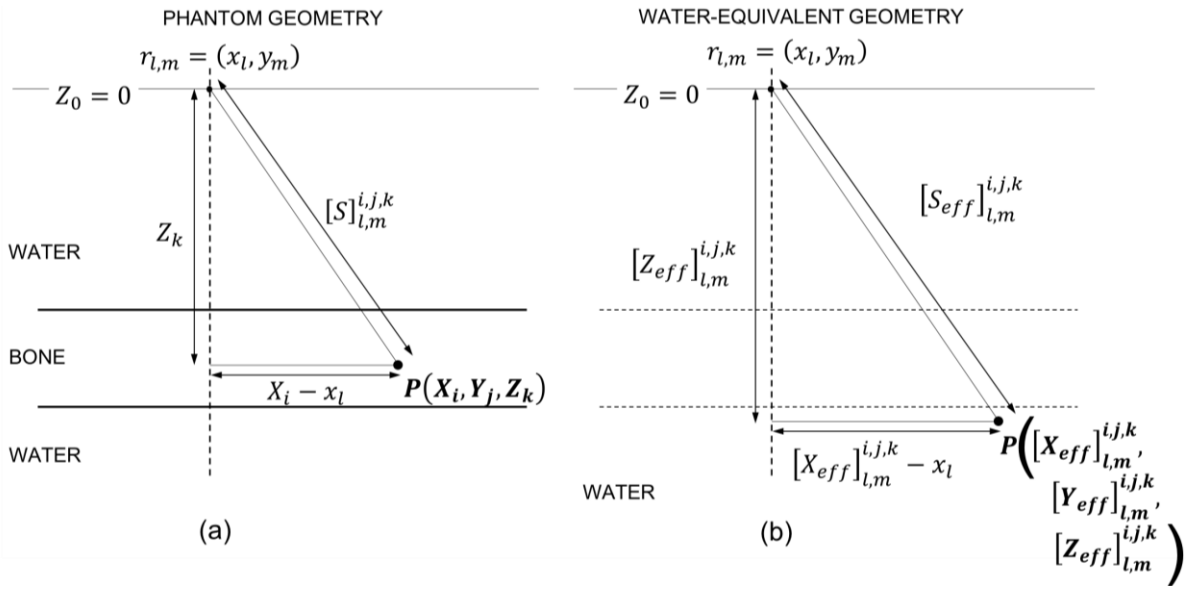

Figure 2.7. To calculate dose from the nuclear halo at point $P(R_{i,j}, Z_k)$ in the phantom geometry from the pencil beam centered at $r_{l,m} = (x_l, y_m)$, we use the effective path calculated in water, $[S_{eff}]_{l,m}^{i,j,k}$. Thus, we transform the geometry in (a) to the water-equivalent geometry in (b), which allows for a straightforward calculation of $[R_{eff}]_{l,m}^{i,j,k}$ (equation 35) and $[Z_{eff}]_{l,m}^{i,j,k}$ (equation 37). $[R_{eff}]_{l,m}^{i,j,k}$ (equation 35) can be used to calculate $[X_{eff}]_{l,m}^{i,j,k}$ and $[Y_{eff}]_{l,m}^{i,j,k}$ (equation 36a-b). The newly calculated $[X_{eff}]_{l,m}^{i,j,k}$, $[Y_{eff}]_{l,m}^{i,j,k}$, and $[Z_{eff}]_{l,m}^{i,j,k}$ are then substituted for (X_i, Y_j, Z_k) into the original halo dose model (equations 32-34), which scales the halo in water to the intended geometry.

In comparing the sub-figures shown in Figure 2.7(a,b), it is clear that both $[S]_{l,m}^{i,j,k}$ and $[S_{eff}]_{l,m}^{i,j,k}$ are at the same angle. This angle is ensured to be the same in both the phantom and water-equivalent geometry because the water-equivalent calculations in the water-equivalent geometry are simply scaling the values in the phantom geometry, not changing the direction in any way. Thus, equating the *sine* of the two angles, we obtain the following general scaling relationship by similar triangles:

$$\left[R_{eff}\right]_{l,m}^{i,j,k} = \left[\frac{S_{eff}}{S}\right]_{l,m}^{i,j,k} \left(R_{i,j} - r_{l,m}\right) + r_{l,m}, \tag{35}$$

where the subscript (l, m) indicates that the variable is calculated along a path originating at the pencil beam centered at (x_l, y_m) (at the phantom surface) and terminating at grid position $\left(X_i, Y_j, Z_k\right)$. Note that $\left[\frac{S_{eff}}{S}\right]_{l,m}^{i,j,k}$ is equivalent to $\left[S_{eff}\right]_{l,m}^{i,j,k} / [S]_{l,m}^{i,j,k}$.

As with the polar angle, the azimuthal angle is also preserved in transforming the phantom geometry to the water-equivalent geometry. Therefore, the ratios between polar coordinate *R* and Cartesian coordinates (*X, Y)* are also preserved. As a result, it is possible to transform equation (35) into the following expressions:

$$\left[X_{eff}\right]_{l,m}^{i,j,k} = \left[\frac{S_{eff}}{S}\right]_{l,m}^{i,j,k} \left(X_i - x_l\right) + x_l, \tag{36a}$$

$$\left[Y_{eff}\right]_{l,m}^{i,j,k} = \left[\frac{S_{eff}}{S}\right]_{l,m}^{i,j,k} \left(Y_j - y_m\right) + y_m. \tag{36b}$$

The scaling along *Z* has a slightly different form since the origin for all $[S]_{l,m}^{i,j,k}$ are at the phantom surface,

$$\left[Z_{eff}\right]_{l,m}^{i,j,k} = \left[\frac{S_{eff}}{S}\right]_{l,m}^{i,j,k} Z_k. \tag{37}$$

Note that this is not the same as $Z_{eff}^{l,m}(Z_k)$ (equation (8)), which is the effective depth in water as calculated along the central-axis of the pencil beam at (x_l, y_m). $\left[Z_{eff}\right]_{l,m}^{i,j,k}$ is the effective scaling along the *Z*-axis, as determined by equation (37).

In the special case of laterally infinite heterogeneities, both $\left[S_{eff}\right]_{l,m}^{i,j,k}$ and $Z_{eff}^{l,m}(Z_k)$ are scaled at the same rates because they traverse the same geometry; thus, $\left[\frac{S_{eff}}{S}\right]_{l,m}^{i,j,k}$ in equations (35-37) can be replaced with $Z_{eff}^{l,m}(Z_k)/Z_k$. Substitution of $Z_{eff}^{l,m}(Z_k)/Z_k$instead of $\left[\frac{S_{eff}}{S}\right]_{l,m}^{i,j,k}$ in equations (35-37) is equivalent to invoking the CAXSIS approximation in equations (35-37).

2.4.3 Modifications to the Nuclear Halo Equation

Recalling that the original nuclear halo was fit to water (equations 32-34), the intended calculation geometry must first be transformed to an equivalent water geometry before these terms can be used to calculate the halo in the desired geometry. In our previous model, this task was straightforward since we applied a one-dimensional depth scaling and used a multiplication by mass stopping power ratio to convert to dose in water to dose in arbitrary material. Now, the process of transforming equations (32-34) to a water-equivalent geometry is slightly more complex as we have three effective coordinates. This transformation can be achieved by replacing the coordinates of the calculation point in the intended geometry, (X_i, Y_j, Z_k), with the effective coordinates in the water-equivalent phantom, $\left(\left[X_{eff}\right]_{l,m}^{i,j,k}, \left[Y_{eff}\right]_{l,m}^{i,j,k}, \left[Z_{eff}\right]_{l,m}^{i,j,k}\right)$. However, because this form for the effective coordinates is cumbersome, we instead use the shorthand $\left(\left[X_{eff}, Y_{eff}, Z_{eff}\right]_{l,m}^{i,j,k}\right)$. Recall that ($l$, m) are meant to reference the pencil beam centered at (x_l, y_m) while (i, j, k) reference the calculation point (X_i, Y_j, Z_k). The superscripts for dose in the equations that follow indicate the calculation point and the subscripts indicate the point of origin (e.g., $\left[D_S^{FS_x,FS_y}\right]_{l,m}^{i,j,k}$). Thus, the secondary dose in equation (32) is modified in the following way:

$$\left[D_S^{FS_X,FS_Y}\right]_{l,m}^{i,j,k} = \left\{\left[D_{SG}^{FS_X,FS_Y}\right]_{l,m}^{i,j,k} + \left[D_{SCL}^{FS_X,FS_Y}\right]_{l,m}^{i,j,k}\right\} \left(\left[\frac{S}{S_{eff}}\right]_{l,m}^{i,j,k}\right)^2, \tag{38}$$

where

$$\begin{aligned}\left[D_{SG}^{FS_X,FS_Y}\right]_{l,m}^{i,j,k} = \sum_{l=1}^{n_x}\sum_{m=1}^{n_y} w_{SG}\left(\left[Z_{eff}\right]_{l,m}^{i,j,k}\right)\left\{\left[D_{expt}^{SSE}\left(\left[Z_{eff}\right]_{l,m}^{i,j,k}\right)\right]_w^{FS_X,FS_Y}\right\}_{SG} \\ \cdot\left(\frac{S}{\rho}\right)_w^{mat}\left(\left[X_{eff}, Y_{eff}, Z_{eff}\right]_{l,m}^{i,j,k};\ \bar{E}(x_l, y_m, Z_k)\right) \\ \cdot\frac{1}{4}\left[\operatorname{erf}\left(\frac{x_l + \frac{\Delta X}{2} - \left[X_{eff}\right]_{l,m}^{i,j,k}}{\sqrt{2}\,\sigma_{SG}^{l,m}\left(\left[Z_{eff}\right]_{l,m}^{i,j,k}\right)}\right) - \operatorname{erf}\left(\frac{x_l - \frac{\Delta X}{2} - \left[X_{eff}\right]_{l,m}^{i,j,k}}{\sqrt{2}\,\sigma_{SG}^{l,m}\left(\left[Z_{eff}\right]_{l,m}^{i,j,k}\right)}\right)\right] \\ \cdot\left[\operatorname{erf}\left(\frac{y_m + \frac{\Delta Y}{2} - \left[Y_{eff}\right]_{l,m}^{i,j,k}}{\sqrt{2}\,\sigma_{SG}^{l,m}\left(\left[Z_{eff}\right]_{l,m}^{i,j,k}\right)}\right) - \operatorname{erf}\left(\frac{y_m - \frac{\Delta Y}{2} - \left[Y_{eff}\right]_{l,m}^{i,j,k}}{\sqrt{2}\,\sigma_{SG}^{l,m}\left(\left[Z_{eff}\right]_{l,m}^{i,j,k}\right)}\right)\right]\end{aligned} \tag{39a}$$

$$\left[D_{SCL}^{FS_X,FS_Y}\right]_{l,m}^{i,j,k} = \sum_{l=1}^{n_x}\sum_{m=1}^{n_y} w_{SCL}\left(\left[Z_{eff}\right]_{l,m}^{i,j,k}\right)\left\{\left[D_{expt}^{SSE}\left(\left[Z_{eff}\right]_{l,m}^{i,j,k}\right)\right]_{w}^{FS_X,FS_Y}\right\}_{SCL}$$
$$\cdot\left(\frac{S}{\rho}\right)_{w}^{mat}\left(\left[X_{eff},Y_{eff},Z_{eff}\right]_{l,m}^{i,j,k};\ \bar{E}(x_l,y_m,Z_k)\right)$$
$$\cdot\frac{1}{4}\left[\operatorname{atan}\left(\frac{x_l+\frac{\Delta X}{2}-\left[X_{eff}\right]_{l,m}^{i,j,k}}{\sigma_{SCL}^{l,m}\left(\left[Z_{eff}\right]_{l,m}^{i,j,k}\right)}\right)-\operatorname{atan}\left(\frac{x_l-\frac{\Delta X}{2}-\left[X_{eff}\right]_{l,m}^{i,j,k}}{\sigma_{SCL}^{l,m}\left(\left[Z_{eff}\right]_{l,m}^{i,j,k}\right)}\right)\right] \quad (39b)$$
$$\cdot\left[\operatorname{atan}\left(\frac{y_m+\frac{\Delta Y}{2}-\left[Y_{eff}\right]_{l,m}^{i,j,k}}{\sigma_{SCL}^{l,m}\left(\left[Z_{eff}\right]_{l,m}^{i,j,k}\right)}\right)-\operatorname{atan}\left(\frac{y_m-\frac{\Delta Y}{2}-\left[Y_{eff}\right]_{l,m}^{i,j,k}}{\sigma_{SCL}^{l,m}\left(\left[Z_{eff}\right]_{l,m}^{i,j,k}\right)}\right)\right].$$

Note that for effective path calculations taking place in water $\left(\text{equivalently, } \left[S_{eff}\right]_{l,m}^{i,j,k} = [S]_{l,m}^{i,j,k}\right)$, all effective coordinates are simply equal to the coordinates of the calculation point in the intended geometry (i.e., equations 35-37 with $\left[S_{eff}\right]_{l,m}^{i,j,k} = [S]_{l,m}^{i,j,k}$), so $\left[D_S^{FS_X,FS_Y}\right]_{l,m}^{i,j,k} = D_S^{FS_X,FS_Y}(X_i,Y_j,Z_k)$, which reduces equation (38) to equation (32), the original nuclear halo equation.

2.4.4 Description of Evaluation Geometries

We evaluated geometries with laterally infinite slabs of both compact bone and air. As with the primary proton dose evaluations, we used the highest energy (250 MeV), a rectangular field size (4x4 cm^2), and deep, thick slabs. Variations in slab depth (z = 10, 20, 30 cm) and thickness (2, 4, 5 cm) were also explored to ensure the new nuclear halo model applied to a wide range of geometries.

2.5 Evaluation of Dose Model in Patient-Like Phantoms (Specific Aim 3)

Recall that in Specific Aim 1, evaluation geometries were selected to test the improvements over the CAXSIS approximation that is part of all PBAs. Only primary dose was calculated to eliminate influence from the nuclear halo model. In Specific Aim 2, we selected evaluation geometries which eliminated the error from the CAXSIS approximation so the improvement in accuracy was indicative of the improved nuclear halo model.

In Specific Aim 3, we compared dose between the present model (equation 38), original model (equation 32), and MCNPX simulations. Geometries used for comparisons in this Aim featured laterally finite heterogeneities and included dose from both the primary and secondary dose terms. Furthermore, the overall

goal in Specific Aim 3 is to characterize the dose accuracy levels achievable by the present model and the prior model in simple "patient-like" phantoms, where heterogeneities are meant to mimic some of the anatomical features one might find in a typical treatment scenario.

2.5.1 Checkerboard Phantom (2 cm x 2 cm)

The checkerboard phantom was designed with alternating 2 cm wide by 2 cm thick air / compact bone slabs. This sort of heterogeneity configuration could potentially be found in the sinus region of the head, where many small bones and air cavities are adjacent to one another. The schematic for the 2 cm x 2 cm checkerboard phantom is shown in Figure 2.8 below.

2.5.2 Prostate Phantom

We designed a prostate phantom by focusing on the major heterogeneities typically encountered in these treatments: the femoral head and the rectum. We approximated the femoral head as a 2 cm radius sphere centered at Z = 19 cm and composed of compact bone (see Table 2.2). The theoretical prostate planning target volume (PTV) was also designed as a 2 cm radius sphere which was centered at Z = 29 cm (the material of the "PTV" was assigned to water). Finally, the rectum was modeled as an ellipsoid with a major axis of 2.98 cm and a minor axis of 1.71 cm. The rectum heterogeneity was also centered at Z = 29 cm and was assigned to air (Table 2.2). The full schematic for the prostate phantom is shown in Figure 2.9 below.

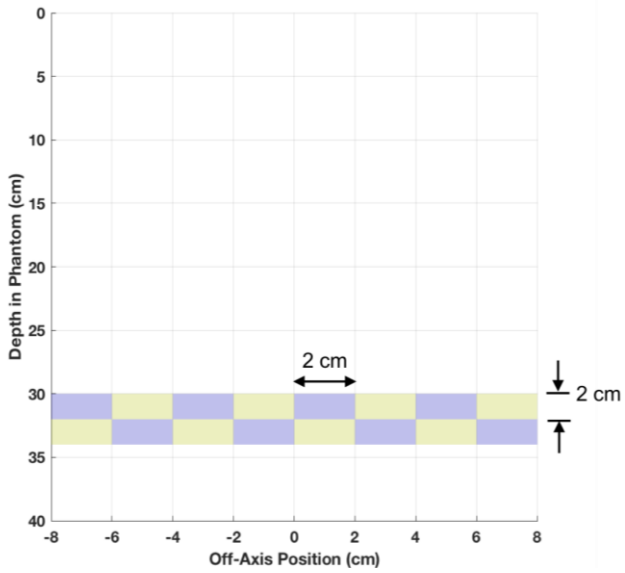

Figure 2.8. Geometry for the 2 cm x 2 cm checkerboard phantom. The phantom consists of 2 cm wide by 2 cm thick alternating slabs of air (blue) and compact bone (yellow).

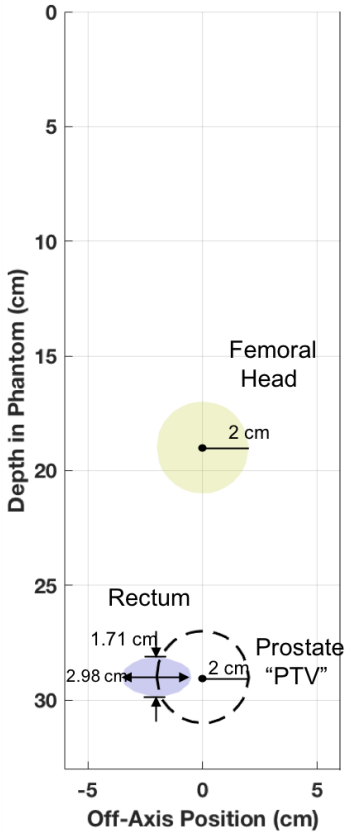

Figure 2.9. Geometry for the prostate phantom. The phantom consists of 2 cm radius femoral head heterogeneity (yellow) centered at Z = 19 cm and composed of compact bone, a 2 cm radius theoretical prostate PTV (black dashed circle) centered at Z = 29 cm (water), and a rectum heterogeneity (blue) that is an ellipse with a major axis of 2.98 cm and a minor axis of 1.71 cm, which is centered at Z = 29 cm and assigned to air. The figure is shown with an aspect ratio of 1:1 so that the distinction between circles and the ellipse is clear.

2.6 Monte Carlo Simulations

All required Monte Carlo data in this work was produced using Monte Carlo N-Particle eXtended (MCNPX) version 2.7e (Pelowitz 2011). The beam used in these simulations was modeled as a monoenergetic, parallel source of protons with uniform intensity. Dose was calculated in these simulations by utilizing the type 3 mesh tally option (MeV cm^{-3} $particle^{-1}$) in MCNPX and dividing the results by mass density (MeV g^{-1} $particle^{-1}$). Default options for both multiple Coulomb scatter and energy straggling were used in all simulations. As previously described in Chapman *et al* (2017), we additionally configured MCNPX to transport protons only while depositing dose from all other particles locally.

We utilized the high performance computing (HPC) cluster at Louisiana State University to run the MCNPX simulations in parallel and reduce the total time required. In each simulation, we selected the

appropriate number of initial histories needed for statistical uncertainties below 1%, which was typically 200x10^6 histories. The typical time required for one of these simulations was about 72 hours on 128 processors (9,216 processor-hours).

The PBA (section 2.2) was commissioned using simulated dose distributions from a model of a simplified proton therapy beamline in MCNPX. This approach was previously verified (Koch *et al* 2005 and Newhauser *et al* 2007). Specifically for the PBA, the central-axis percent depth dose (PDD) was extracted for two energies (100 and 250 MeV) and a field size of 4x4 cm^2, which provided the required $\left[D_{expt}(z)\right]_w^{FS_X,FS_Y}$ in section 2.2. As mentioned in section 2.3.3, the correction factors needed for intial energies (100 and 250 MeV), $C(Z_k;\ E_0)$, also required MC simulations. Finally, MC simulations were used both to parameterize the nuclear halo model (as discussed previously in Knutson *et al* 2012) and as the standard of comparison for both the previous model and the present model in the geometries selected for evaluation.

2.7 Evaluating the Dosimetric Accuracy of Present Model and Chapman *et al* (2017)

Dose calculated by the present model ("PM") was compared with the original, Chapman *et al* (2017) model ("OM"), using MCNPX data ("MC") as the gold standard for monoenergetic (100 and 250 MeV) beams and a spread-out Bragg peak with 5 cm of range modulation with a 4x4 cm^2 field size. Dose for each model was normalized to the maximum dose in a homogeneous water phantom for the same incident beam, which gave the relative dose

$$\left[RD^{FS_X,FS_Y}(X_i,Y_j,Z_k)\right]_{PM} = 100\,.\frac{\left[D^{FS_X,FS_Y}(X_i,Y_j,Z_k)\right]_{PM}}{\left[D_w^{FS_X,FS_Y}(0,0,Z_{max})\right]_{PM}}, \tag{40a}$$

$$\left[RD^{FS_X,FS_Y}(X_i,Y_j,Z_k)\right]_{OM} = 100\,.\frac{\left[D^{FS_X,FS_Y}(X_i,Y_j,Z_k)\right]_{OM}}{\left[D_w^{FS_X,FS_Y}(0,0,Z_{max})\right]_{OM}}, \tag{40b}$$

$$\left[RD^{FS_X,FS_Y}(X_i,Y_j,Z_k)\right]_{MC} = 100\,.\frac{\left[D^{FS_X,FS_Y}(X_i,Y_j,Z_k)\right]_{MC}}{\left[D_w^{FS_X,FS_Y}(0,0,Z_{max})\right]_{MC}}, \tag{40c}$$

where the subscripts (*PM*, *OM*, and *MC*) refer to the present model, original model, and MCNPX simulations, respectively. $D_w^{FS_X,FS_Y}$ is used to specify dose in a homogeneous water phantom, and Z_{max} is the depth along the central-axis at which the dose is maximum in the homogeneous water phantom. We compared all three models (*PM*, *OM*, and *MC*) using various geometries (chapter 3), and used the percentage of pixels passing 3% dose difference of 1 mm distance-to-agreement (DTA) as a measure of the improvements in the PM compared to the OM. Dose difference between MC and dose model *X* (meant as a generic label for either 'PM' or 'OM') was calculated using

$$\Delta RD_{MC-X}^{FS_X,FS_Y} = \left[RD^{FS_X,FS_Y}(X_i, Y_j, Z_k)\right]_{MC} - \left[RD^{FS_X,FS_Y}(X_i, Y_j, Z_k)\right]_X. \quad (41)$$

Distance-to-agreement was calculated using the method by Ju *et al* (2008).

CHAPTER 3. RESULTS

In this chapter, results are presented for each of the three aims in this work. Each section provides comparisons detailing the relative performance of three dose calculation approaches: (1) the model in the present work (hereafter referred to as the "present model," or "PM"); (2) the Chapman *et al* (2017) PBA (hereafter referred to as the "original model," or "OM"); and, (3) the Monte Carlo data that is used as the standard of comparison for PM and OM, denoted "MC" for this chapter. All data presented in this chapter compared dose between PM, OM, and MC.

The comparisons in this chapter are mostly based on the percentage of points that pass the 3% or 1 mm criteria set in the hypothesis. It should be further noted that most of these "pass rate" calculations are only tested on points that are below the distal edge of the last major heterogeneity and also within 1% isodose line (the "distal slab area"); this approach was chosen because the largest dosimetric differences between PM and OM are expected below the distal edge of the slab heterogeneity. Another geometry (5 cm bone slab at z = 30 cm) calculated the pass rate below the proximal slab edge and within the 1% isodose line because this particular slab covered most of the Bragg peak. Additional metrics for determining agreement between dose models include dose difference maps and histograms in the distal slab area, central-axis and lateral profiles, and the distance-to-agreement (DTA) of the 1% isodose lines.

3.1 Results for Specific Aim 1

For all of the results that follow for Specific Aim 1, all calculation approaches (PM, OM, and MC) were limited to primary dose only. Results are presented as inter-comparisons between these three models in a homogeneous water phantom, laterally finite compact bone / air slab phantoms, for a monoenergetic (250 MeV) beam. Table 3.1 summarizes the results for this aim.

Table 3.1. Results for homogenous water and laterally finite slabs. Columns in the table indicate the percentage of points passing our criteria of 3% or 1 mm.

GEOMETRY	Passrate (3% or 1 mm DTA)	
	PM (%)	OM (%)
Homogeneous Water	100.0	100.0
4 cm Bone Slab (z = 30 cm)	98.0	69.0
4 cm Air Slab (z = 30 cm)	99.5	69.5

3.1.1 Homogeneous Water Phantom

Our results for Specific Aim 1 begin with a homogeneous water geometry. For this phantom, a 250 MeV beam with a field size of 4x4 cm^2 was used. Figure 3.1 shows isodose comparisons of dose calculated using the PM relative to MC and dose calculated by the OM relative to MC. In both cases, 100.0% of points passed our criteria of 3% or 1 mm. Some statistical noise is evident at the 30% isodose line for the PM, but this could be reduced by using a higher number of initial protons (10^6 were used in this case). Central-axis (Figure 3.2) and lateral profiles at the depth of maximum dose (Figure 3.3) are also shown. Agreement was excellent between all models in water.

3.1.2 Laterally Finite Slabs

For laterally finite slabs (compact bone and air) of 4 cm thickness at *z=30* cm extending from *x=0* cm to the right phantom edge, we tested a 250 MeV, 4x4 cm^2 beam and compared the results between PM, OM, and MC. For the compact bone case (Figure 3.4), 98.0% of points calculated by the PM were within 3% or 1 mm of MC calculations. In contrast, the agreement between the OM and MC was 69.0%. The improvement of the PM in addressing the limitations associated with the CAXSIS approximation is evident comparing the dose difference maps and histograms in Figure 3.5. The PM, which is not limited by the CAXSIS approximation, models the deposition of proton dose in a more physically realistic way than the OM.

We also compared the lateral profiles at *z=34.5* cm (Figure 3.6) for all three calculation models (PM, OM, MC). We found that the PM matched the MC profile to within +0.5% and -3.0% dose difference and it is visually evident in Figure 3.6(a) that the PM correctly modeled primary dose changes due to the water-bone interface near the slab. Because the OM was based on the CAXSIS approximation, inaccurate pencil beam modeling near the slab edge (*x=0* cm) averaged out the dose between all the contributing pencil beams, resulting in dose differences within +8.5% and -13.5%.

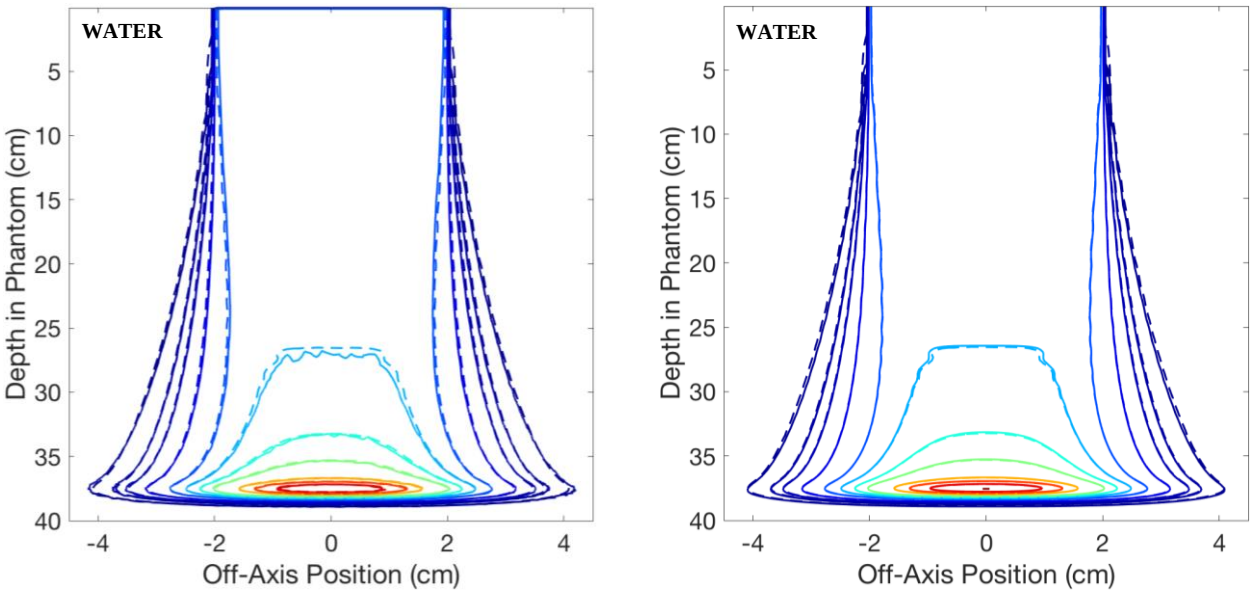

(a) (b)

Figure 3.1. Primary dose calculation for a 250 MeV, 4x4 cm^2 beam in water, shown using (a) PM (solid) vs MC (dashed), and (b) OM (solid) and MC (dashed). 100.0% of points in both (a) and (b) satisfied 3% or 1 mm. Isodose lines shown include 1, 2, 5, 10, 20, 30, 40, 50, 70, 90, and 100 %.

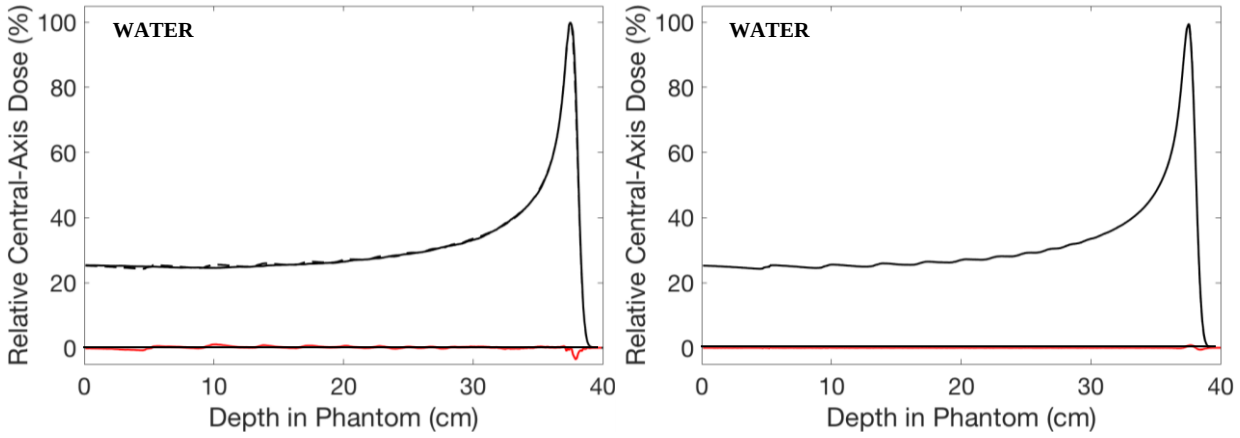

(a) (b)

Figure 3.2. Central-axis depth dose profiles for the homogeneous water geometry (Figure 3.1). Data shown using (a) PM (solid) vs MC (dashed), and (b) OM (solid) vs MC (dashed). The red plot in each panel indicates dose difference in this profile. The dose difference in (a) is within +1.0% to -3.0% and (b) within +/-1.0% for all points.

For the laterally finite air slab case (Figure 3.7), 99.5% of points calculated by the PM were within 3% or 1 mm of MC. In contrast, agreement between OM and MC was 69.5%. As with the bone slab, the PM overcomes limitations imposed by the CAXSIS approximation in the OM, which is evident comparing the dose difference maps and histograms in Figure 3.8.

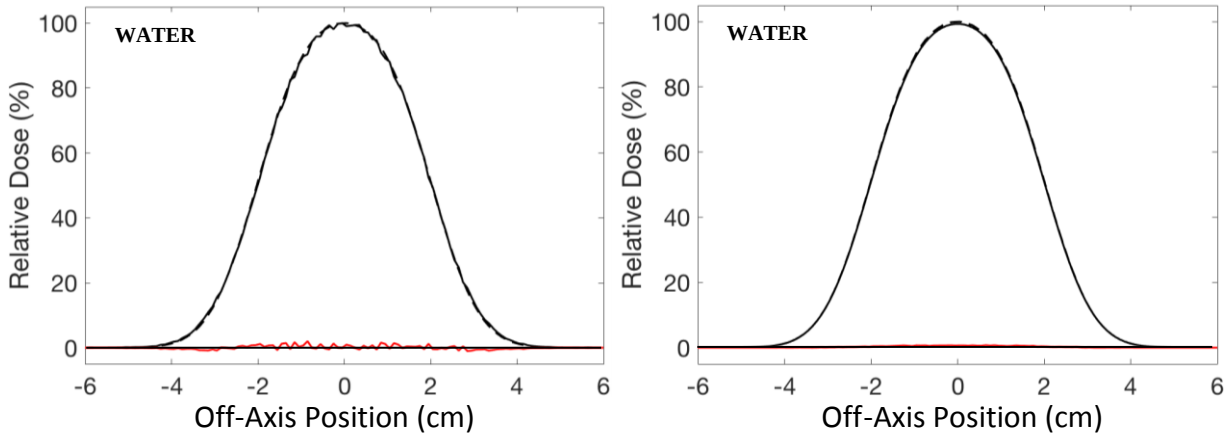

(a) (b)

Figure 3.3. Lateral dose profiles at the depth of maximum dose for the homogeneous water geometry (Figure 3.1). Data shown using (a) PM (solid) vs MC (dashed), and (b) OM (solid) vs MC (dashed). The red plot in each panel indicates dose difference in this profile. The dose difference in (a) is within +/-1.5% and in (b) is within +/-0.5%.

In comparing the lateral profiles at *z=34.5* cm (Figure 3.9) for all three calculation models (PM, OM, MC), we found that the PM matched the MC profile to within +1.0% and -2.0% dose difference and it is visually evident in Figure 3.9(a) that the PM correctly modeled primary dose changes due to the water-air interface near the slab. Because the OM was based on the CAXSIS approximation, the convolution of multiple, inaccurate pencil beams near the slab edge (*x=0* cm) averaged out the dose between all the contributing pencil beams, resulting in dose differences within +2.0% and -5.0%.

3.2 Results for Specific Aim 2

For all of the results that follow for Specific Aim 2, all calculation approaches (PM, OM, and MC) included both primary and secondary dose (i.e., total dose). The presentation of results for Specific Aim 2 here are broken down into thin (2 cm) and thick (4, 5 cm) slab sections (additional comparisons are shown in the Appendix). The general trend observed was improvement in low isodose lines for all slabs, and in-field improvement for deep slabs only. For this reason, the figures in this section will only feature deep slabs (z = 30 cm).

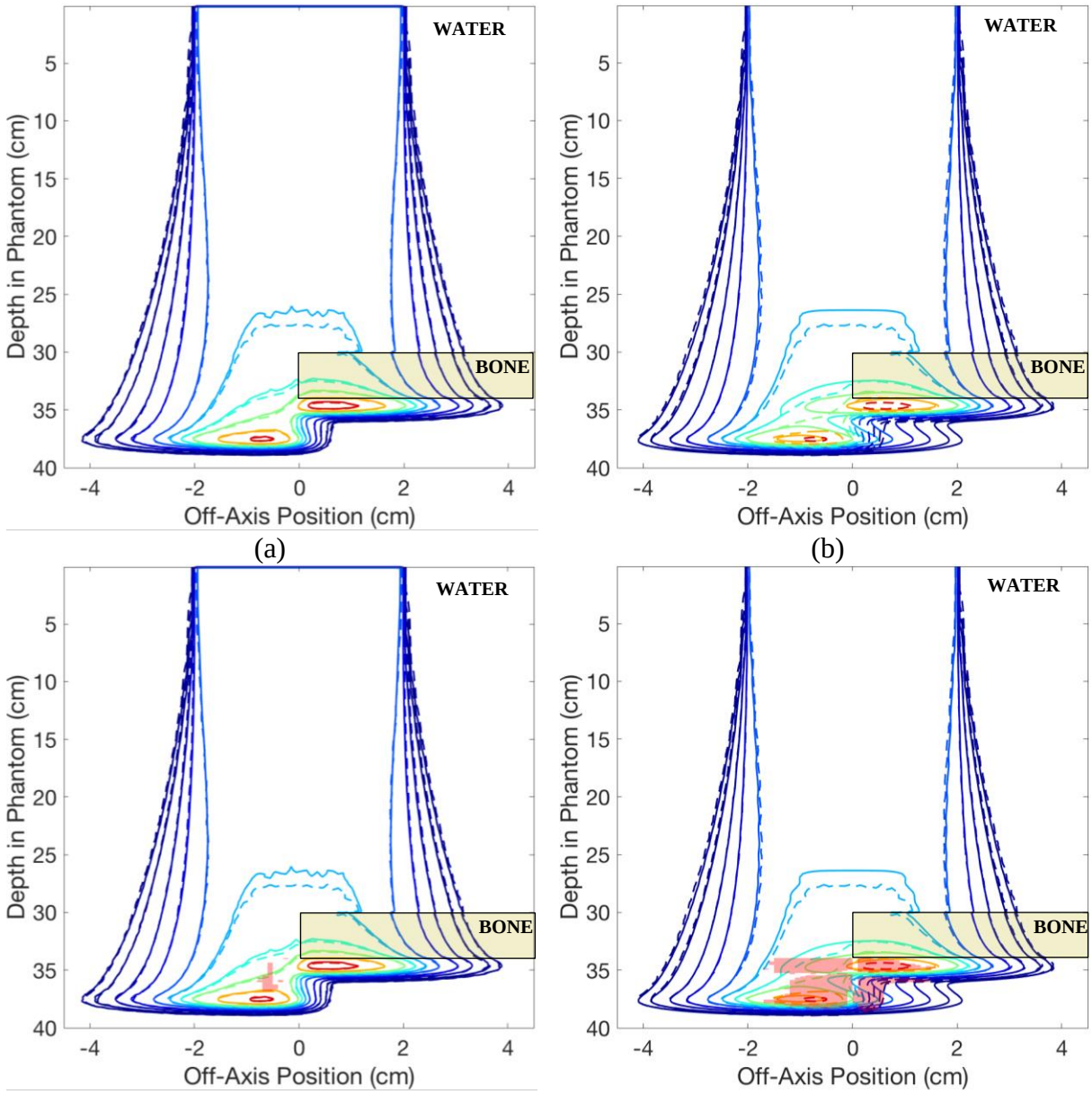

Figure 3.4. Isodose comparisons (1, 2, 5, 10, 20, 30, 40, 50, 70, 90, and 100 %) for a 250 MeV, 4x4 cm^2 beam in a water phantom with a 4 cm compact bone slab at *z=30 cm* that stretches from *x=0 cm* to the right phantom edge. Shown using (a,c) PM (solid) vs MC (dashed), and (b,d) OM (solid) vs MC (dashed). Pass rates were 98.0% (a,c) and 69.0% (b,d) and areas of failure are indicated in translucent red shading (c,d). The compact bone slab is indicated as a translucent yellow rectangle.

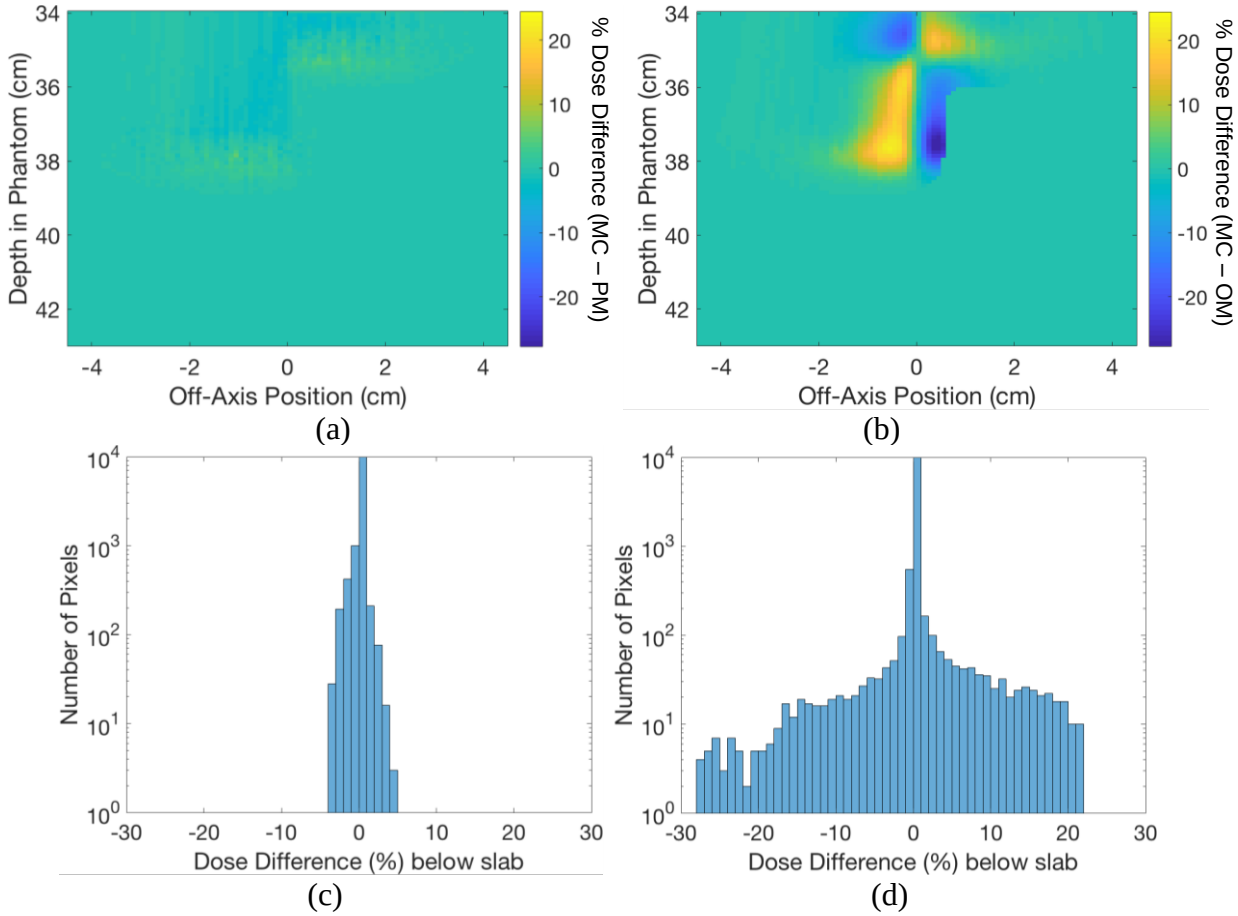

Figure 3.5. Dose difference maps between the PM and MC (a) and between OM and MC (b) for the 4 cm laterally finite bone slab at z = 30 cm (Figure 3.4). Note that dose differences in all panels of this figure are only calculated below the slab. Both dose difference maps use the same color scale, which is indicated in the bars to the right of (a) and (b). This data is also histogrammed for the PM vs MC (c) and OM vs MC (d).

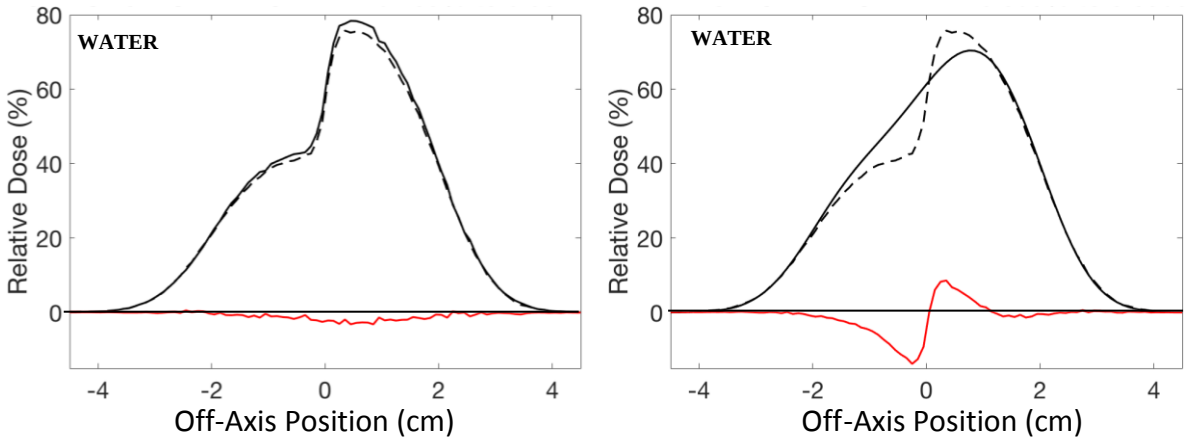

Figure 3.6. Lateral dose profiles at *z=34.05* cm for (a) the PM (solid black) vs MC (dashed), and (b) OM (solid black) vs MC (dashed) for the 4 cm laterally finite bone slab at z = 30 cm (Figure 3.4). The red plot in each panel indicates dose difference in this profile. The dose difference in (a) is within +0.5% to -3.0% and (b) within +8.5% to -13.5%.

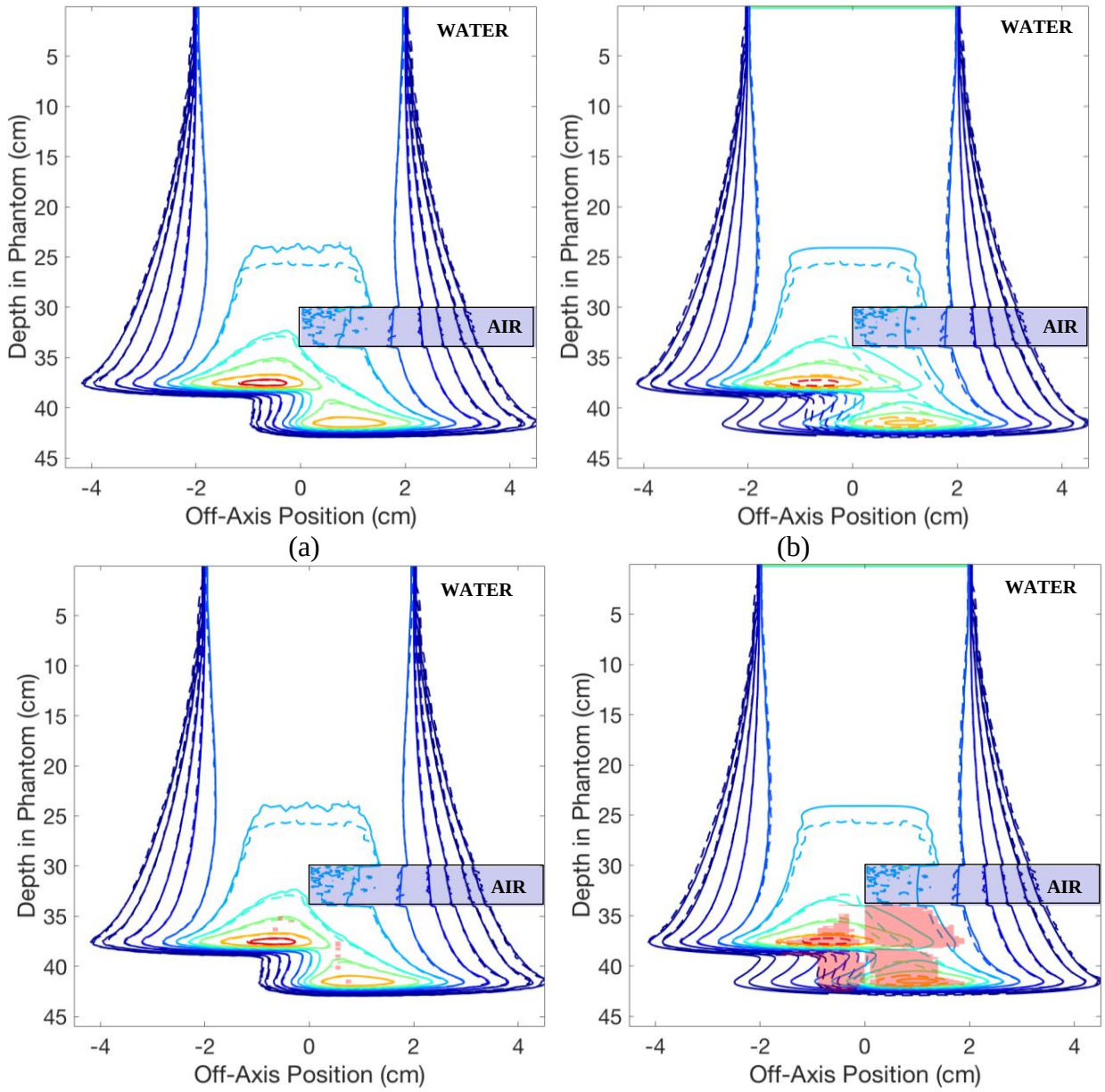

Figure 3.7. Isodose comparisons (1, 2, 5, 10, 20, 30, 40, 50, 70, 90, and 100 %) for a 250 MeV, 4x4 cm^2 beam in a water phantom with a 4 cm air slab at *z=30 cm* that stretches from *x=0 cm* to the right phantom edge. Shown using (a,c) PM (solid) vs MC (dashed), and (b,d) OM model (solid) and MC (dashed). Pass rates were 99.5% (a,c) and 69.5% (b,d) and areas of failure are indicated in translucent red shading (c,d). The air slab is indicated as a translucent blue rectangle.

3.2.1 Thin Slab (2 cm) Results

For thin slabs (2 cm thick), little difference was observed between the accuracy of the PM and the OM. Differences became more evident as slab depth increased toward the end of range. The primary difference noted in thin slab evaluations was improved modeling of the low isodose lines (e.g., 1% of dose maximum) in or distal to the heterogeneity in the PM. For brevity, we will omit dose difference maps and histograms from this

section as the PM and OM models resulted in similar dose values. Because results were similar for thin slabs at all depths (z = 10, 20, 30 cm), we examine the results for the z = 30 cm case and specify differences at other depths where necessary. In discussing these results, if no slab depth is mentioned the implication is that the result applies to all slab depths equally. A comprehensive data summary for thin slab results is in Table 3.2.

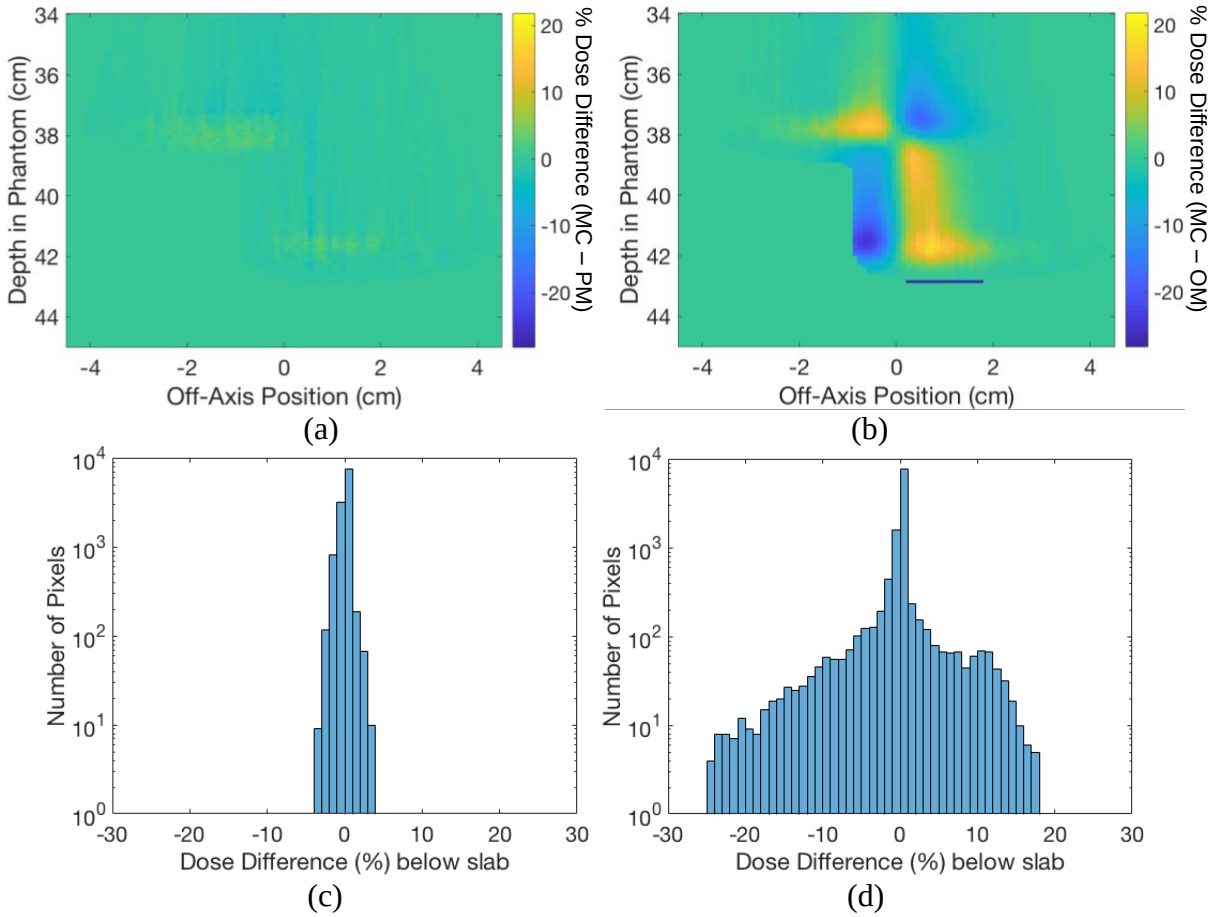

Figure 3.8. Dose difference maps between the PM and MC (a) and between OM and MC (b) for the 4 cm laterally finite air slab at z = 30 cm (Figure 3.7). Note that dose differences in all panels of this figure are only calculated below the slab. Both dose difference maps use the same color scale, which is indicated in the bars to the right of (a) and (b). This data is also histogrammed for the PM vs MC (c) and OM vs MC (d).

For a 250 MeV, 4x4 cm^2 beam in a water phantom with a 2 cm bone slab, we tested slab depths of z = 10, 20, 30 cm (z = 30 cm data shown in Figure 3.10). Both the PM and the OM had pass rates of 100.0% (z = 10, 20, 30 cm) compared to MC data. The percent differences observed between the PM vs MC and the OM vs MC were within +/-1.0% of each other distal to the slabs (z = 10, 20, 30 cm), and the PM exhibited slightly higher maximum percentage differences distal to the slab than the OM (<1.0%). Additionally, a slight shift was noted (0.5 mm deeper) in the position of the Bragg peak calculated by the PM in geometries with a 2 cm bone

slab compared to MC. In Figure 3.11, the OM overestimates dose immediately proximal to the peak and underestimates dose at the peak. Lateral profiles below the distal edge of the slab (z = 32.5 cm) are shown in Figure 3.12.

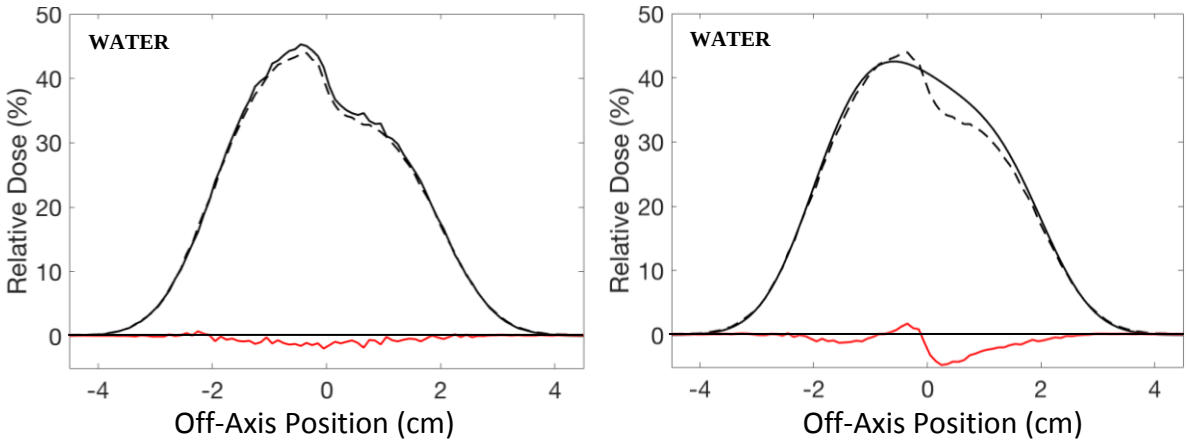

(a) (b)

Figure 3.9. Lateral dose profiles at *z=34.5* cm for (a) the PM (solid black) vs MC (dashed), and (b) OM (solid black) vs MC (dashed) for the 4 cm laterally finite air slab at z = 30 cm (Figure 3.7). The red plot in each panel indicates dose difference in this profile. The dose difference in (a) is within +1.0% to -2.0% and (b) within +2.0% to -5.0%.

Table 3.2. Results for thin (2 cm) compact bone and air slabs. Columns in the table indicate the percentage of points passing our criteria of 3% or 1 mm, and the improvement (negative values: worsening) in the DTA of the 1% isodose line (calculated by subtracting the DTA of the OM vs MC from the DTA of the PM vs MC).

2 cm BONE Slab				
DEPTH (cm)	Passrate (3% or 1 mm)		DTA improvement at 1% (PM - OM)	
	PM (%)	OM (%)	Distal Slab Edge (mm)	Beyond Slab (mm)
10	100.0	100.0	3.9	0.6 to 4.2
20	100.0	100.0	2.1	0.6 to 2.7
30	100.0	100.0	1.5	1.6 to 1.9
2 cm AIR Slab				
DEPTH (cm)	Passrate (3% or 1 mm)		DTA improvement at 1% (PM - OM)	
	PM (%)	OM (%)	Distal Slab Edge (mm)	Beyond Slab (mm)
10	100.0	99.8	6.6	-0.3 to -6.5
20	100.0	99.8	4.5	-0.6 to -3.2
30	99.6	99.3	3.1	0.4 to 2.6

The DTA of the 1% isodose line at the distal edge of the bone slab between the PM and MC improved by 3.9 mm (z = 10 cm), 2.1 mm (z = 20 cm), or 1.5 mm (z = 30 cm) relative to the DTA between the OM and MC. The DTA improvement at all depths further downstream was between 0.6 and 4.2 mm (z = 10 cm), between 0.6 and 2.7 mm (z = 20 cm), or between 1.6 and 1.9 mm (z = 30 cm). The improved DTA at the 1%

isodose line of the PM for these geometries compared to the OM is due to secondary protons in the nuclear halo being modeled over more realistic paths than the central-axis of pencil beams.

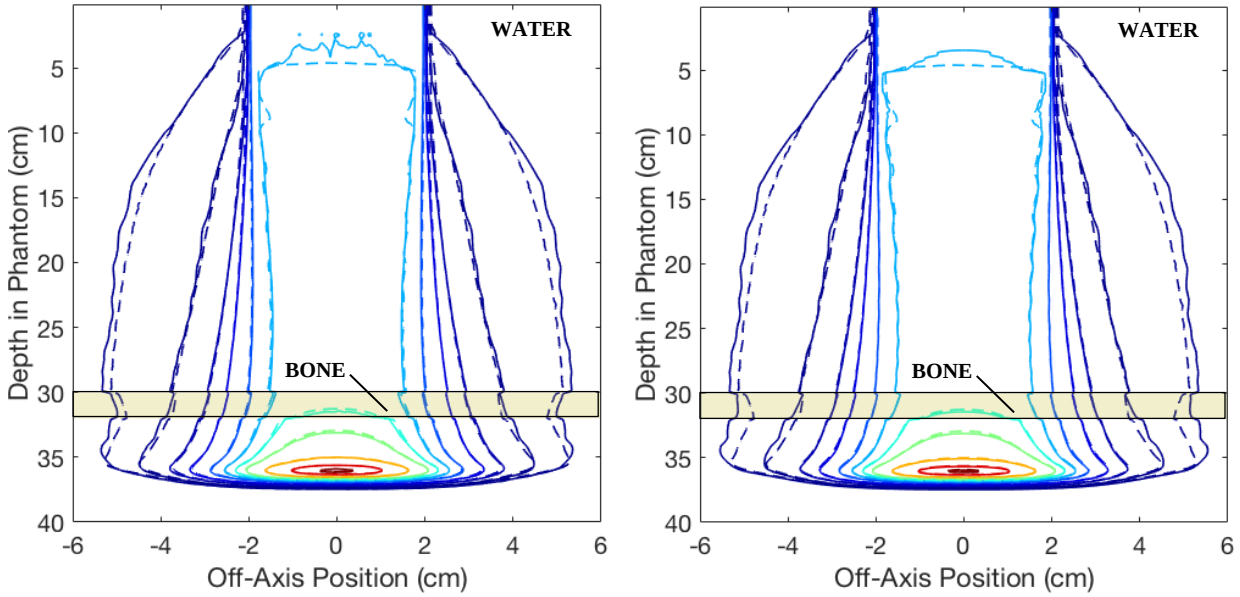

(a) (b)

Figure 3.10. Isodose (1, 2, 5, 10, 20, 30, 40, 50, 70, 90, and 100%) comparisons for a 250 MeV, 4x4 cm^2 beam in a water phantom with a 2 cm compact bone slab at *z=30 cm* (translucent yellow rectangle). Shown using (a) the PM (solid) vs MC (dashed), and (b) OM (solid) vs MC (dashed). Pass rates were 100.0% in both (a) and (b).

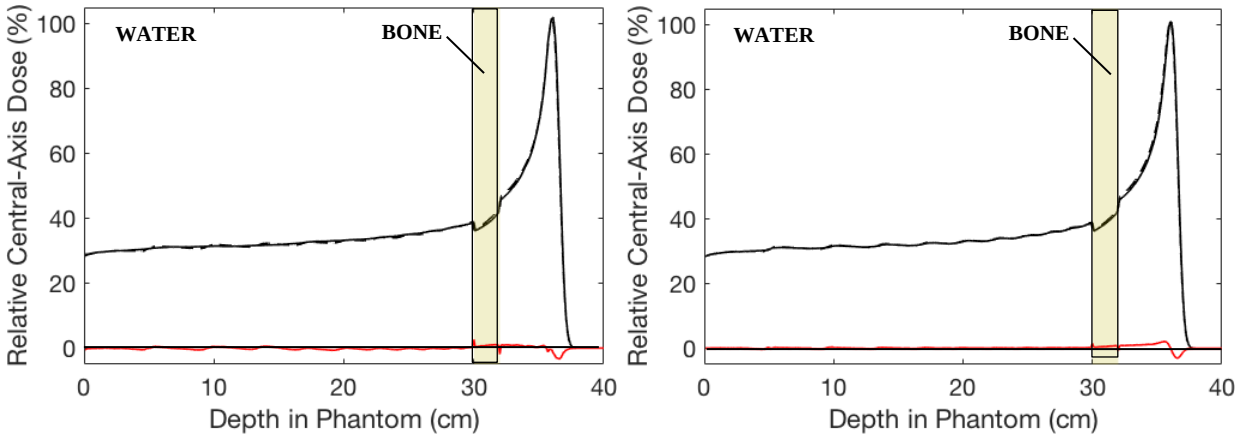

(a) (b)

Figure 3.11. Central-axis depth dose profiles for the 2 cm laterally infinite bone slab at z = 30 cm (Figure 3.10). Data shown using (a) PM (solid) vs MC (dashed), and (b) OM (solid) vs MC (dashed). The bone slab in both plots is indicated as a translucent yellow rectangle. Dose difference between each analytical model and MC in both plots is shown in red. Agreement in the profile shown in (a) is within +2.5% and -3.5% and agreement in (b) is +2.0% and -3.0% for all points.

With a 2 cm air slab at z = 10 cm, the PM had a 100.0% pass rate (z = 10 and 20 cm) and the OM had a 99.8% pass rate (z = 10 and 20 cm). For a slab depth of 30 cm, the PM had a pass rate of 99.6% while the OM had a pass rate of 99.3%. The maximum dose difference distal to the slab heterogeneity decreased from 4.2%

(OM vs MC) to 2.8% (PM vs MC) (z = 10 cm), 4.5% (OM vs MC) to 2.4% (PM vs MC) (z = 20 cm), and 7.4% (OM vs MC) to 5.6% (PM vs MC) (z = 30 cm). Furthermore, for the 2 cm air slab at z = 10 cm, improvement of the 1% isodose line in the slab (6.6 mm DTA) caused a downstream overestimation of the 1% isodose line (0.3-6.5 mm DTA). When this slab was placed at z = 20 cm, there was a 4.5 mm DTA improvement in the slab for the 1% isodose lines and a downstream overestimation of 0.6-3.2 mm. Finally, placing the 2 cm air slab at z = 30 cm (Figure 3.13), the improvement of the 1% isodose lines in the slab (3.1 mm DTA) was observed distal to the slab and was improved by 0.4-2.6 mm further downstream. The improved DTA at the 1% isodose line at the distal edge of the PM for these geometries compared to the OM is due to secondary protons in the nuclear halo being modeled over more realistic paths than the central-axis of pencil beams. However, the PM had worse agreement in the DTA of the 1% isodose line further downstream. This was probably due to neglecting the changes due to heterogeneities in the number of secondary particles produced from non-elastic nuclear interactions. Interestingly, the worsened DTA in the 1% isodose line distal to the air slab was not observed for the same 4 cm air slab at z = 30 cm. This may be due to low scatter out of the pencil beam central-axis below the slabs at z = 10 cm and 20 cm compared to the high scatter at z = 30 cm. The scatter at z = 10 cm and 20 cm is perhaps not large enough to re-establish side scatter and charged particle equilibrium.

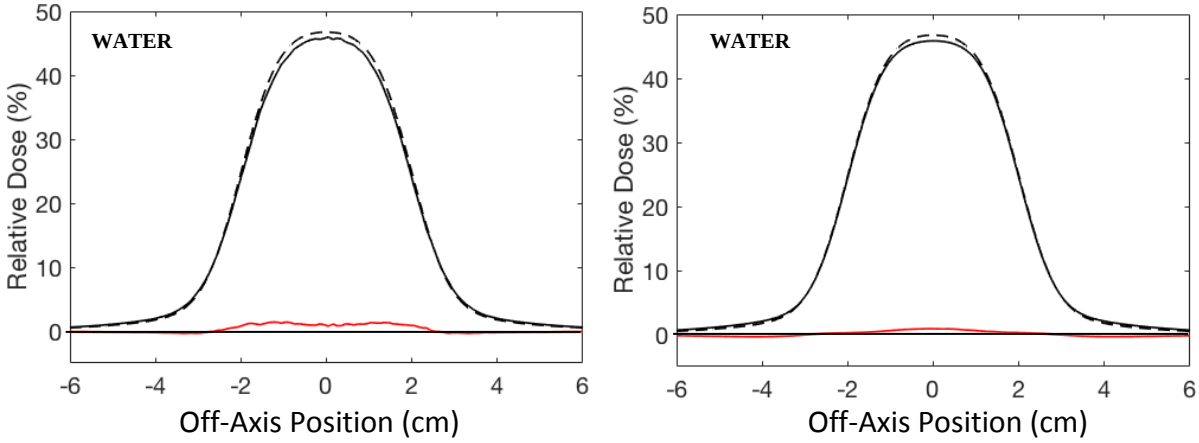

(a) (b)

Figure 3.12. Lateral dose profiles taken at z = 32.5 cm for the 2 cm laterally infinite bone slab at z = 30 cm (Figure 3.10). Data shown using (a) PM (solid) vs MC (dashed), and (b) OM (solid) vs MC (dashed). The red plot in each panel indicates dose difference in this profile. Agreement in the profile shown in (a) is within +1.5% to -0.5% and agreement in (b) is +1.0% and -0.5% for all points.

Because the areas of failure in this geometry covered very small areas that did not obscure underlying data, Figure 3.13 shows the data with areas of failure indicated in red. Examining the central-axis profiles in Figure 3.14, these maximum dose differences distal to the slab seem to be manifested in modeling of the Bragg peak. Lateral profiles are also shown in Figure 3.15.

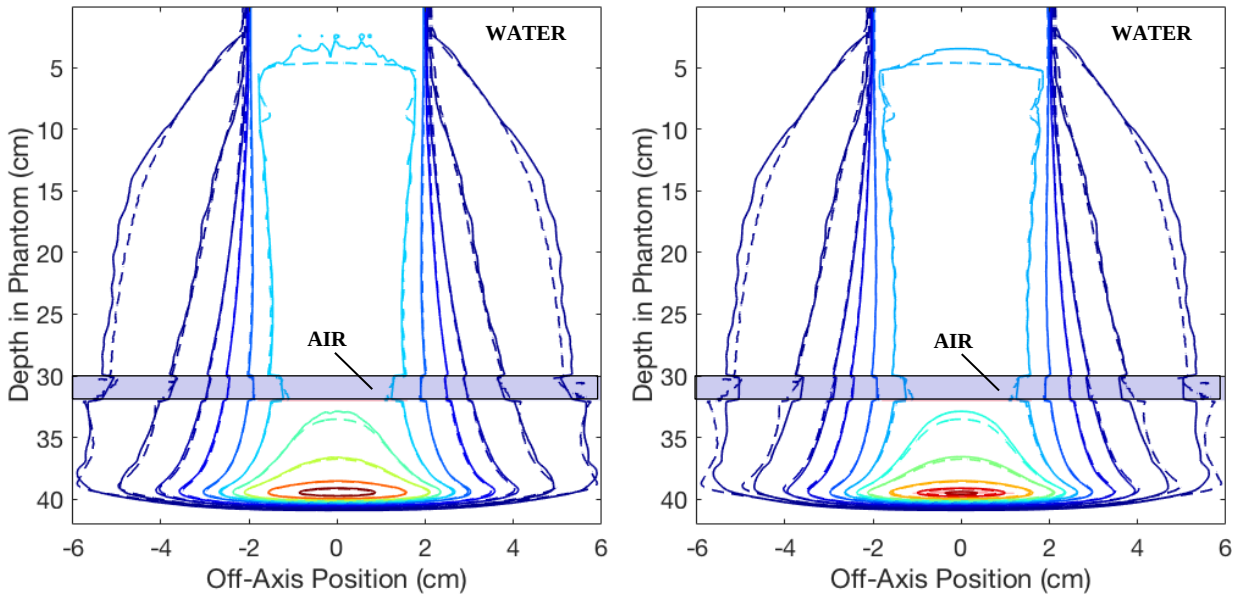

(a) (b)

Figure 3.13. Isodose (1, 2, 5, 10, 20, 30, 40, 50, 70, 90, and 100%) comparisons for a 250 MeV, 4x4 cm^2 beam in a water phantom with a 2 cm air slab at *z=30 cm* (translucent blue rectangle). Shown using (a) the PM (solid) vs MC (dashed), and (b) OM (solid) vs MC (dashed). Pass rates were 99.6% (a) and 99.3% (b). Areas of failure are indicated in translucent red shading. Failures are at the distal edge of the slab in (a) and (b) and near the Bragg peak in (b).

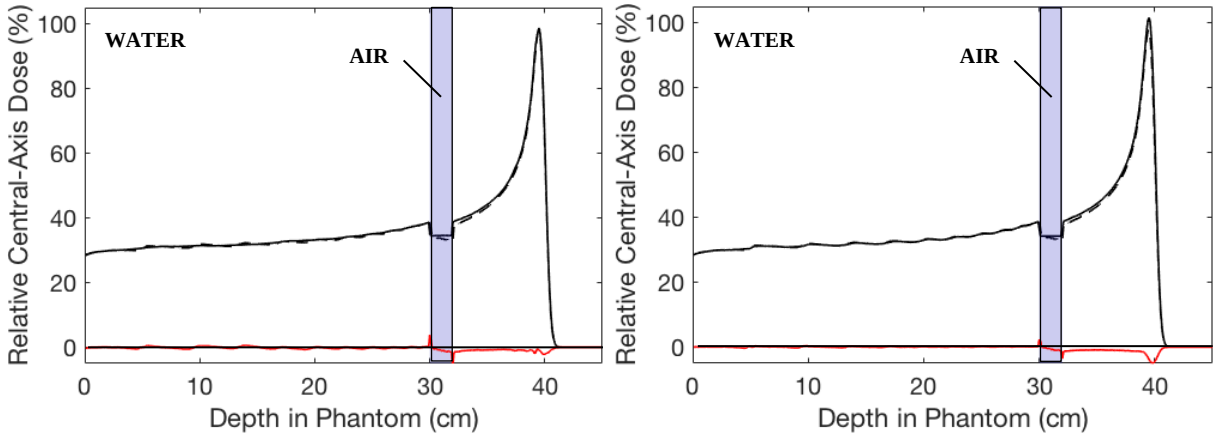

(a) (b)

Figure 3.14. Central-axis depth dose profiles for the 2 cm laterally infinite air slab at z = 30 cm (Figure 3.13). Data shown using (a) PM (solid) vs MC (dashed), and (b) OM (solid) vs MC (dashed). The air slab in both plots is indicated as a translucent blue rectangle. The red plot in each panel indicates dose difference in this profile. Agreement in the profile shown in (a) is within +4.0% and -5.5% and agreement in (b) is +2.5% and -5.0% for all points. The highest dose differences in (a) were at material interfaces; however, the dose difference at the peak is much smaller.

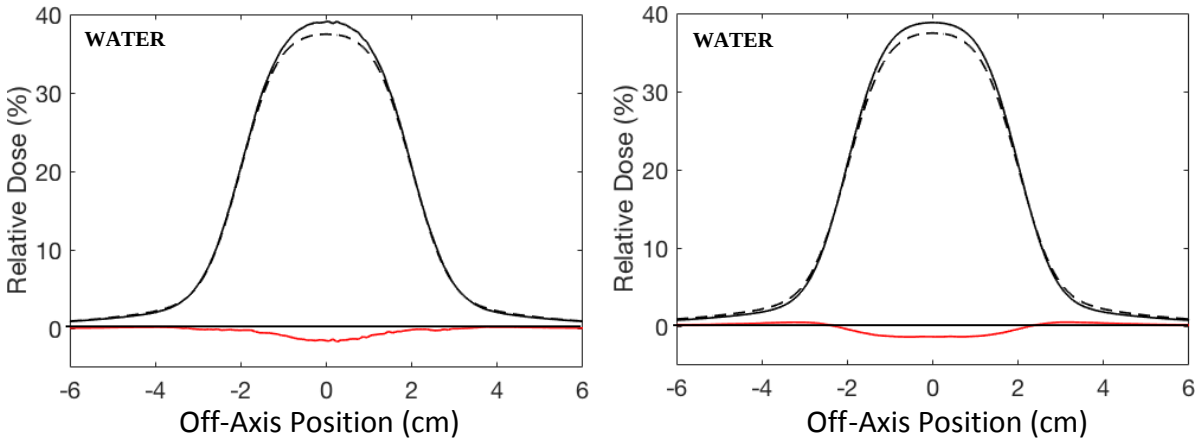

(a) (b)

Figure 3.15. Lateral dose profiles taken at z = 32.5 cm for the 2 cm laterally infinite air slab at z = 30 cm (Figure 3.13). Data shown using (a) PM (solid) vs MC (dashed), and (b) OM (solid) vs MC (dashed). The red plot in each panel indicates dose difference in this profile. Agreement in the profiles shown in (a) and (b) are within 0.5% to -1.5%.

3.2.2 Thick Slab (4, 5 cm) Results

For a 250 MeV, 4x4 cm^2 beam in a water phantom with a 4 cm bone slab, we tested slab depths of z = 10, 20, 30 cm. Both the PM and OM had pass rates of 100.0% (z = 10, 20 cm) and for z = 30 cm, the PM had a pass rate of 100.0% whereas the OM had a pass rate of 98.6% compared to MC. The percent dose difference between the PM and MC was within +/-2.5% of the dose difference between the OM vs MC distal to the slabs (z = 10, 20, 30 cm). A slight shift was noted (1 mm deeper) in the position of the Bragg peak (z = 10, 20 cm) calculated by the PM in geometries with a 4 cm bone slab compared to MC. However, for a 4 cm bone slab at z = 30 cm (Figure 3.16), the PM better matched dose at the Bragg peak compared to the OM (by 1.6%). A summary of all data for thick slabs is in Table 3.3.

To understand the differences between PM and OM in this geometry, Figure 3.17 shows dose difference maps and histrograms for PM-MC (Figure 3.17(a,c)) and OM-MC (Figure 3.17(b,d)). In Figure 3.17, differences are evident between the PM and OM both laterally and in depth. The lateral dose differences in the OM can be attributed to accounting for material-dependence using the one-dimensional effective depth, as this approach inherently neglects broadening of the secondary protons. In contrast, the PM accounts for the broadening of secondary particles both by virtue of calculating effective (x, y) coordinates, and by the inverse-square factor. As a result of the OM neglecting broadening, dose differences are extended over larger areas

compared to the same dose difference values in the PM. For instance, the +2.0% dose difference between OM and MC (Figure 3.17(b)) are distributed over a wider area compared to the +2.0% dose difference between PM and MC (Figure 3.17(a)). This is also evident by examining the dose difference bin extending from 1.0% to 2.0% in Figure 3.17(c,d). Additionally, the DTA for the 1.0% isodose line at the distal edge of the bone slab between the PM and MC decreased by 2.5 mm (z = 10 cm), 2.3 mm (z = 20 cm), or 2.4 mm (z = 30 cm) compared to the DTA between the OM and MC. The DTA improvement further downstream was 0.7 to 3.1 mm (z = 10 cm), 0.9 to 2.3 mm (z = 20 cm), or 2.2 to 2.4 mm (z = 30 cm). Thus, secondary proton broadening impacted dose at far off-axis values as well.

Table 3.3. Results for thick (4 and 5 cm) compact bone and air slabs. Columns in the table indicate the percentage of points passing our criteria of 3% dose difference or 1 mm distance-to-agreement, and the improvement (negative values: worsening) in the DTA of the 1% isodose line (calculated by subtracting the DTA of the OM vs MC from the DTA of the PM vs MC).

4, 5 cm BONE Slab				
GEOMETRY	Passrate (3% or 1 mm)		DTA improvement at 1% (PM - OM)	
	PM (%)	OM (%)	Distal Slab Edge (mm)	Beyond Slab (mm)
4 cm Slab at z = 10 cm	100.0	100.0	2.5	0.7 to 3.1
4 cm Slab at z = 20 cm	100.0	100.0	2.3	0.9 to 2.3
4 cm Slab at z = 30 cm	100.0	98.6	2.4	2.2 to 2.4
5 cm Slab at z = 30 cm	99.4	99.0	2.9 at z = 34 cm	
4, 5 cm AIR Slab				
GEOMETRY	Passrate (3% or 1 mm)		DTA improvement at 1% (PM - OM)	
	PM (%)	OM (%)	Distal Slab Edge (mm)	Beyond Slab (mm)
4 cm Slab at z = 10 cm	99.6	99.6	1.9	-2.4 to -8.5
4 cm Slab at z = 20 cm	99.6	99.0	2.2	-2.8 to 3.4
4 cm Slab at z = 30 cm	98.6	85.6	6.7	2.4 to 7.6
5 cm Slab at z = 30 cm	94.6	78.5	6.2	2.2 to 6.0

Differences between the PM and OM were also observed along the central-axis (Figure 3.18). Comparing the central-axis plots for the PM and OM relative to MC, it is clear that distal to the slab heterogeneity, the PM better matches MC than the OM. For instance, at the Bragg peak, the PM had a dose difference of -0.2%. In contrast, the OM had a dose difference of +1.8% at the Bragg peak. Note that along the central-axis ($x = y = 0$), equations (36A-B) do *not* result in $\left[X_{eff}\right]_{l,m}^{i,j,k} = \left[Y_{eff}\right]_{l,m}^{i,j,k} = 0$, because these effective coordinates are functions of pencil beam position (x_l, y_m). Thus, the PM results in differences along depth, including the central-axis, compared to the OM. The inverse-square factor in equation 38 is an additional factor

that contributes to differences between PM and OM along depth. Lateral profiles for this geometry are shown in Figure 3.19.

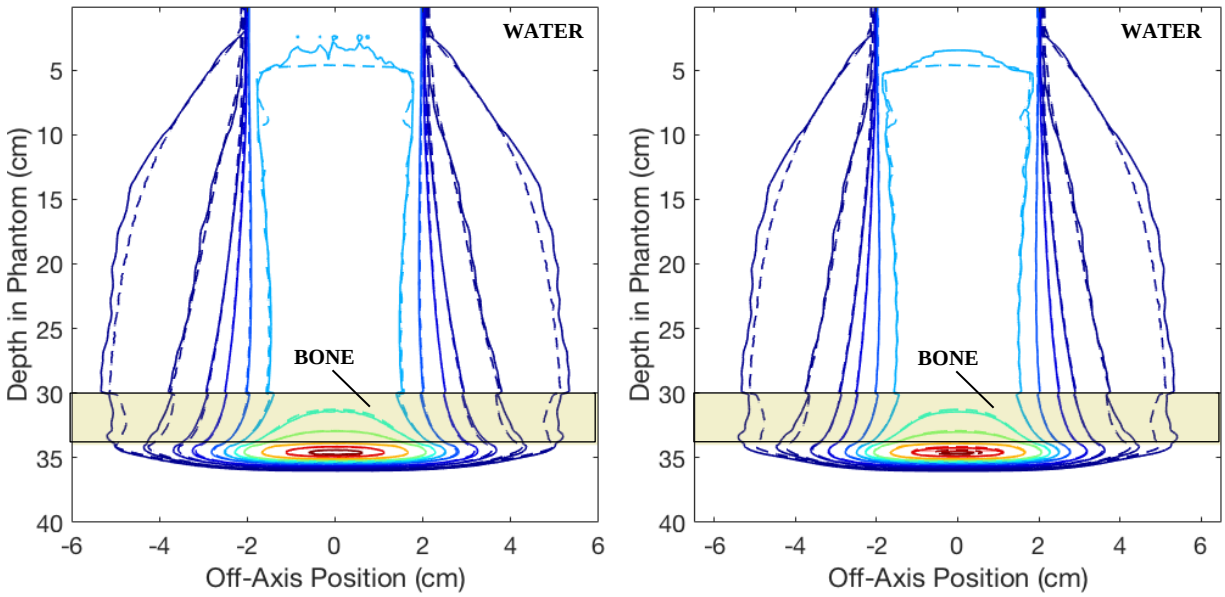

(a) (b)

Figure 3.16. Isodose (1, 2, 5, 10, 20, 30, 40, 50, 70, 90, and 100%) comparisons for a 250 MeV, 4x4 cm^2 beam in a water phantom with a 4 cm compact bone slab at *z=30 cm* (translucent yellow rectangle). Shown using (a) the PM (solid) vs MC (dashed), and (b) OM (solid) vs MC (dashed). Pass rates were 100.0% (a) and 98.6% (b). Areas of failure are indicated in translucent red shading. Failures are near the high dose area in (b).

For a 5 cm bone slab at z = 30 cm, the results were similar to those for the 4 cm bone slab at z = 30 cm. The pass rates in this geometry were 99.4% (PM) vs 99.0% (OM) (Figure 3.20). We also examined dose difference maps and histograms (Figure 3.21) below the *proximal* edge of the slab. The PM was found to improve the dose difference at the Bragg peak compared to the OM (by ~8%) (Figure 3.22). Additionally, the DTA of the 1% isodose line at z = 34 cm of the bone slab between the PM and MC improved by 2.9 mm relative to the DTA between OM and MC. We chose to compare the DTA of the 1% isodose line at z = 34 cm because the distal edge of the slab is beyond the Bragg peak.

For a 250 MeV, 4x4 cm^2 beam in a water phantom with a 4 cm air slab, we tested slab depths of z = 10, 20, 30 cm. Both the PM and the OM had pass rates of 99.6% compared to MC for the slab at z = 10 cm. At z = 20 cm, the pass rate was 99.6% for the PM and 99.0% for the OM. With the air slab at z = 30 cm (Figure 3.23), the pass rate seen was 98.6% (PM) vs 85.6% (OM). There are significantly higher areas of failure using the OM for this geometry (4 cm air slab at z = 30 cm) compared to the OM in the 4 cm bone slab geometry. The reason

for this disparity includes the negligible energy loss and scatter across air slabs of a few cm (i.e., S_w^{air} and the scattering power in air are both very small) whereas the energy loss and scatter across bone slabs are greater than in water. Thus, in the OM, the halo dose at the distal edge of the air slab is nearly equal to the halo dose at the proximal edge of the air slab (by virtue of their effective depths being nearly equal), regardless of slab thickness (for thicknesses up to a few cm). The low scattering power in air slabs causes each pencil beam in the OM to be transported across the air slab along the central-axis of the pencil beam, and there is loss of side scatter and charged particle equilibrium. The PM model transports particles over more complex paths because dose calculated by the PM at the distal edge of the air slab is a function of the relative position between the central-axis of each pencil beam and the calculation point of interest and is further scaled by the inverse-square factor.

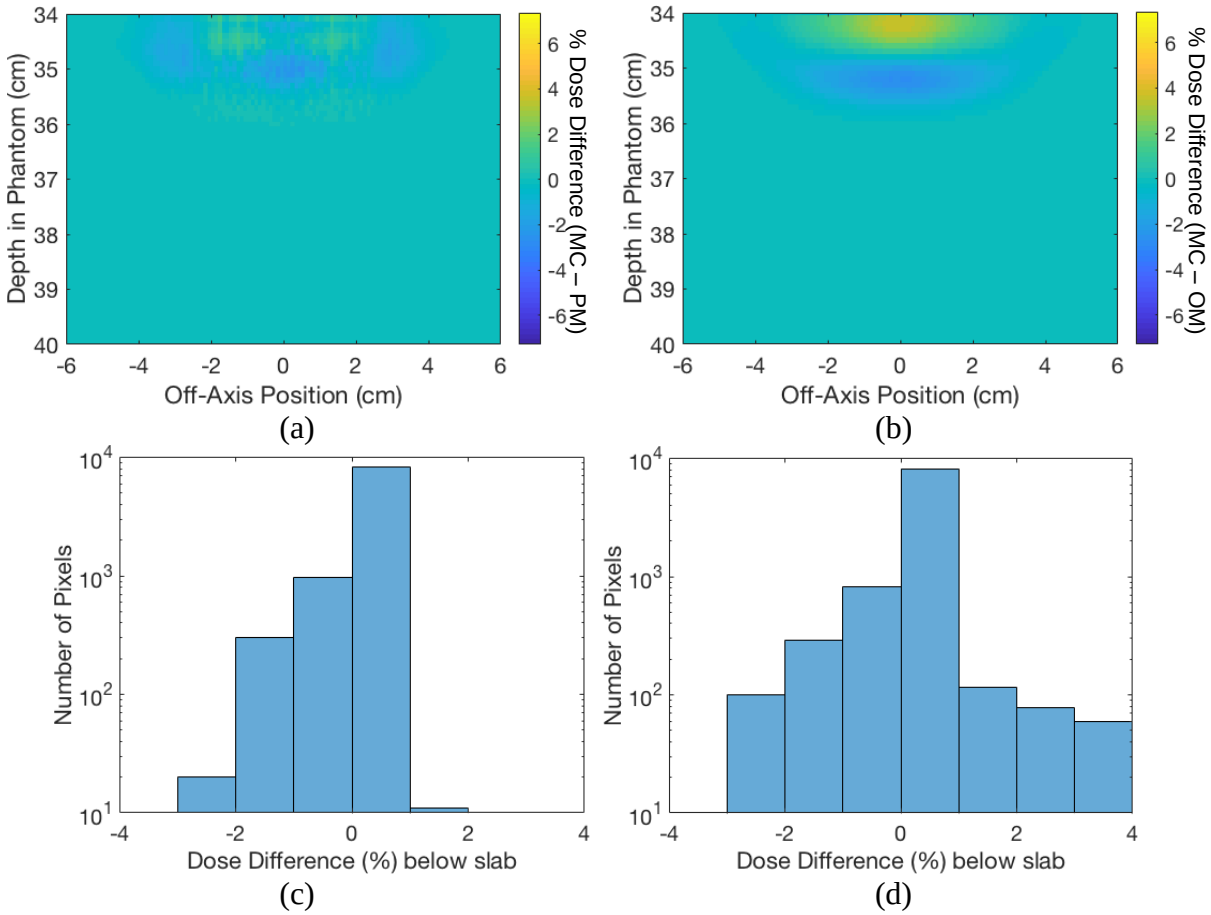

Figure 3.17. Dose difference maps between the PM and MC (a) and between OM and MC (b) for the 4 cm laterally infinite bone slab at z = 30 cm (Figure 3.16). Note that dose differences in all panels of this figure are only calculated below the slab. Both dose difference maps use the same color scale, which is indicated in the bars to the right of (a) and (b). This data is also histogrammed for the PM vs MC (c) and OM vs MC (d).

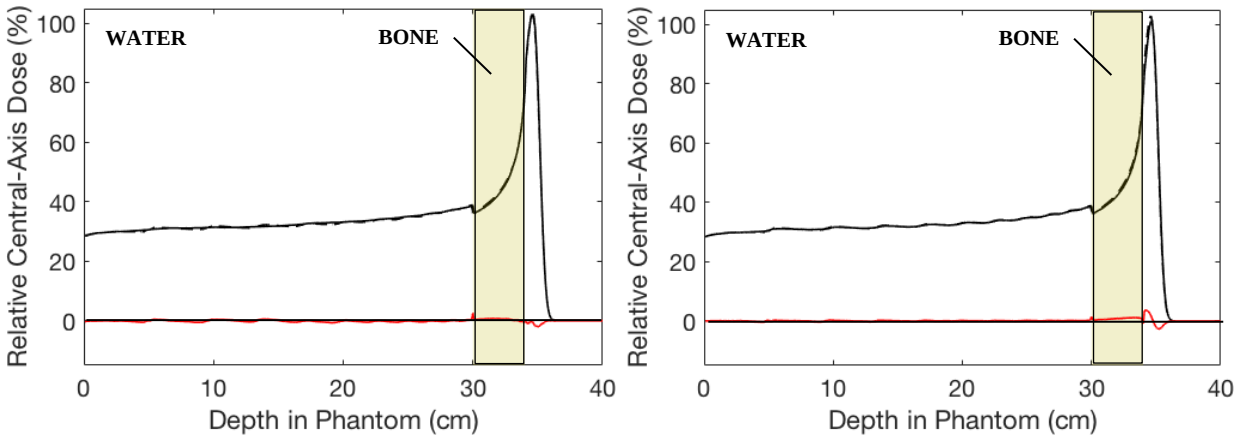

(a) (b)

Figure 3.18. Central-axis depth dose profiles for the 4 cm laterally infinite bone slab at z = 30 cm (Figure 3.16). Data shown using (a) PM (solid) vs MC (dashed), and (b) OM (solid) vs MC (dashed). The bone slab in both plots is indicated as a translucent yellow rectangle. The red plot in each panel indicates dose difference in this profile. Agreement in the profile shown in (a) is within +2.5% and -2.0% and agreement in (b) is +3.5% and -2.5% for all points.

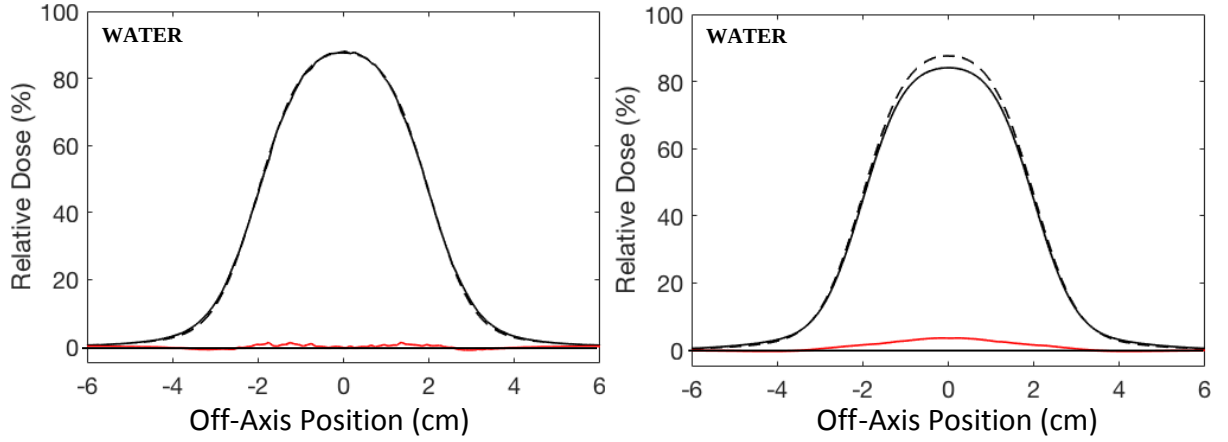

(a) (b)

Figure 3.19. Lateral dose profiles taken at z = 34.5 cm for the 4 cm laterally infinite bone slab at z = 30 cm (Figure 3.16). Data shown using (a) PM (solid) vs MC (dashed), and (b) OM (solid) vs MC (dashed). The red plot in each panel indicates dose difference in this profile. Agreement in the profiles are within 1.5% to -1.0% (a) or 3.5% to -0.5% (b).

As with the bone slab, the OM resulted in dose differences extended over larger areas compared to equivalent dose differences in the PM (Figure 3.24). However, the dose difference for the OM in the distal slab area (Figure 3.24(b)) is systematically underestimated. For instance, the -2.0% to 0.0% dose difference between the PM and MC (Figure 3.24(a)) in this area increased to a consistent -4.0% to -5.0% dose difference between the OM and MC (Figure 3.24(b)). This underesimation is also seen in Figure 3.25(b). Note that in the central-axis profile of Figure 3.25(a), the PM significantly improves dosimetric agreement distal to the slab.

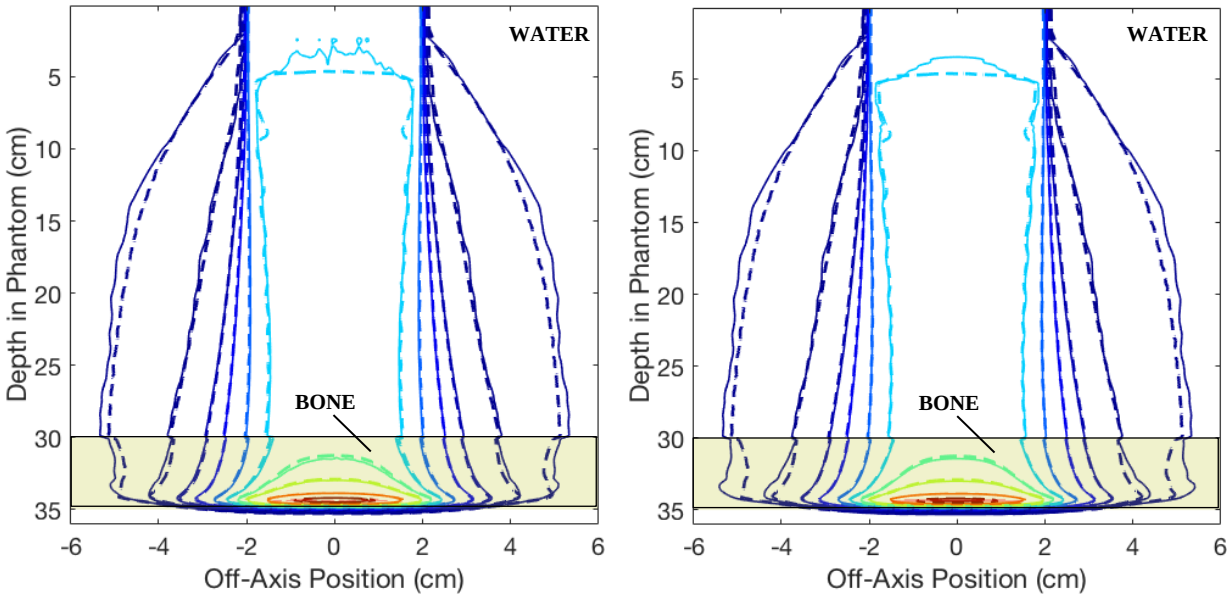

(a) (b)

Figure 3.20. Isodose (1, 2, 5, 10, 20, 30, 40, 50, 70, 90, and 100%) comparisons for a 250 MeV, 4x4 cm^2 beam in a water phantom with a 5 cm compact bone slab at *z=30 cm* (translucent yellow rectangle). Shown using (a) the PM (solid) vs MC (dashed), and (b) OM (solid) vs MC (dashed). Pass rates were 99.4% (a) and 99.0% (b). Areas of failure are indicated in translucent red shading. Failures were near the distal edge of the Bragg peak in (a) and at the Bragg peak in (b).

The DTA for the 1% isodose line at the distal edge of the air slab between the PM and OM decreased by 1.9 mm (z = 10 cm), 2.2 mm (z = 20 cm), and 6.7 mm (z = 30 cm) compared to the DTA between the OM and MC. Beyond the distal edge of the slab, the DTA of the 1% isodose line between the PM and MC was overestimated by 2.4 to 8.5 mm (z = 10 cm) compared to the DTA between the OM and MC. For the slab at z = 20 cm, the DTA of the 1% isodose line between the PM and MC beyond the distal edge of the slab ranged from values that overestimated the DTA by 2.8 mm to improvements of 3.4 mm compared to the DTA between the OM and MC. For the slab at z = 30 cm, the DTA of the 1% isodose line between the PM and MC beyond the distal edge of the slab improved by 2.4 to 7.6 mm (z = 30 cm) compared to the DTA between the OM and MC. Thus, the broadening of secondary protons accounted for in the PM impacted dose at far off-axis values.

For a 5 cm air slab at z = 30 cm, the results were similar to those for the 4 cm air slab at z = 30 cm. The pass-rates in this geometry were 94.6% for the PM and 78.5% for the OM (Figure 3.26). Dose difference maps and histograms are shown in Figure 3.27. Maximum dose differences were at the Bragg peak (Figure 3.28). Lateral profiles are shown in Figure 3.29.

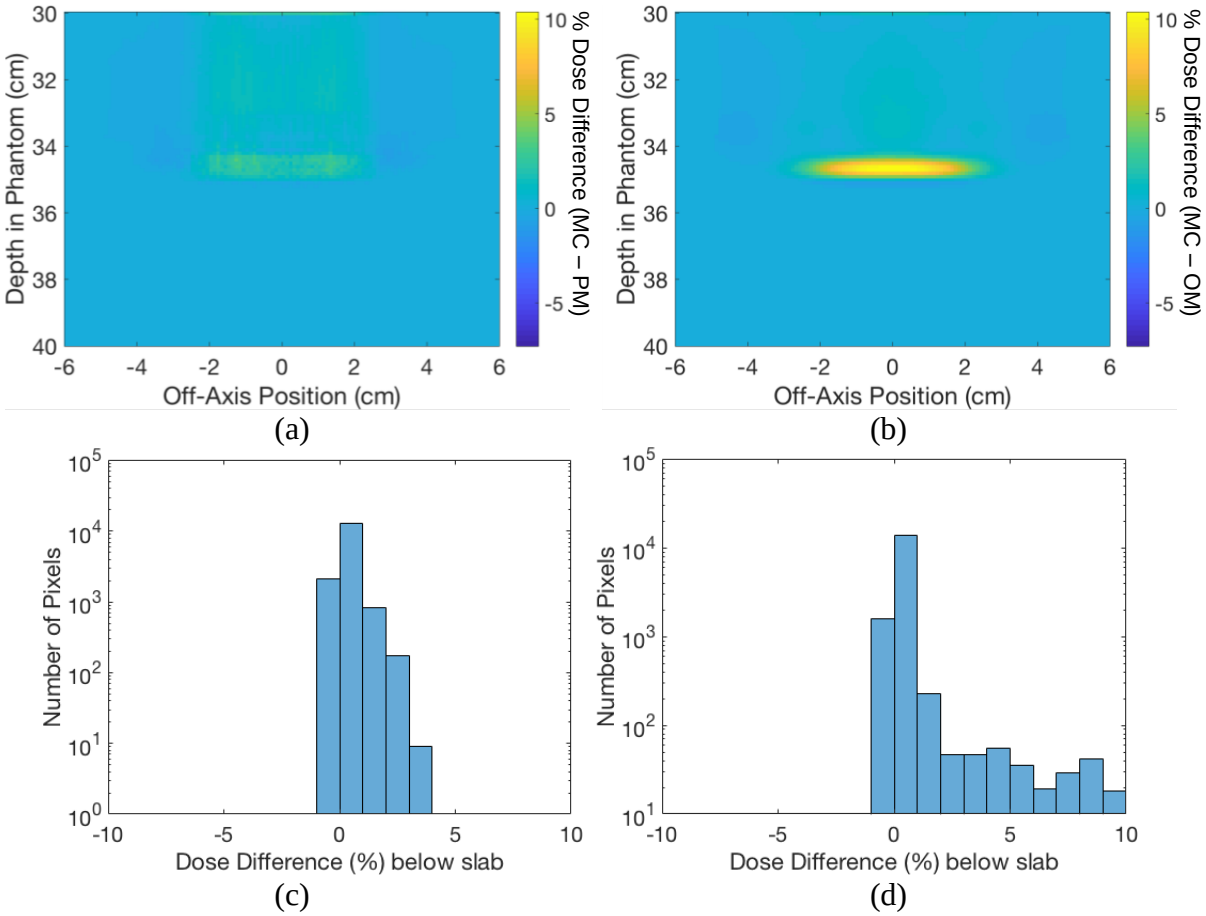

Figure 3.21. Dose difference maps between the PM and MC (a) and between OM and MC (b) for the 5 cm laterally infinite bone slab at z = 30 cm (Figure 3.20). Note that dose differences in all panels of this figure are only calculated below the slab. Both dose difference maps use the same color scale, which is indicated in the bars to the right of (a) and (b). This data is also histogrammed for the PM vs MC (c) and OM vs MC (d).

The DTA of the 1% isodose line at the distal edge of the bone slab between the PM and MC improved by 6.2 mm relative to the DTA between OM and MC. Beyond the slab, the DTA improvement of the 1% isodose lines was 2.2 to 6.0 mm.

3.3 Results for Specific Aim 3

For all of the results that follow for Specific Aim 3, all calculation approaches (PM, OM, and MC) included both primary and secondary dose (i.e., total dose). The results include calculations in a 2 cm x 2 cm checkerboard phantom, a prostate phantom, and a paranasal phantom. All geometries were tested using monoenergetic beams, and the checkerboard and prostate phantoms additionally tested a SOBP beam. A summary for all the data for Specific Aim 3 is in Table 3.4.

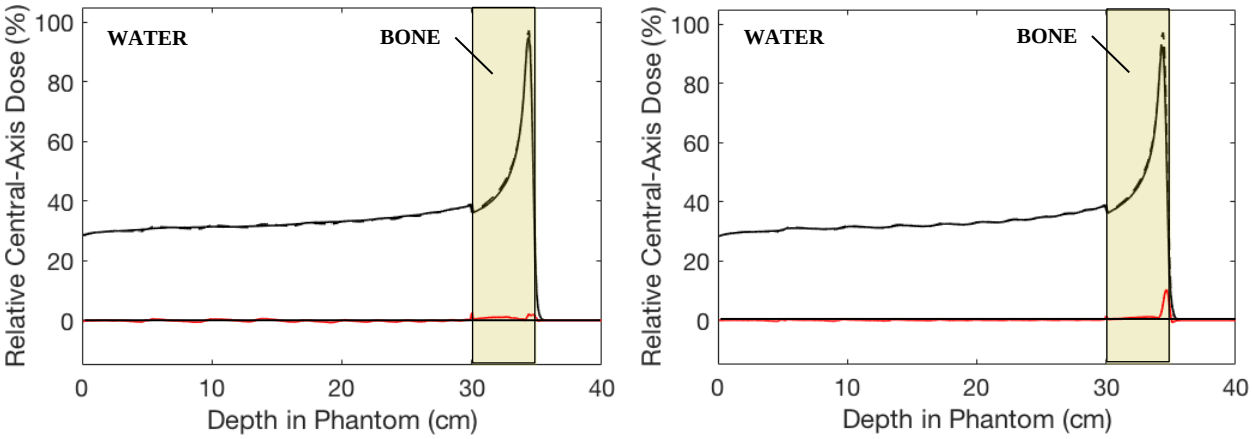

(a) (b)

Figure 3.22. Central-axis depth dose profiles for the 5 cm laterally infinite bone slab at z = 30 cm (Figure 3.20). Data shown using (a) PM (solid) vs MC (dashed), and (b) OM (solid) vs MC (dashed). The bone slab in both plots is indicated as a translucent yellow rectangle. The red plot in each panel indicates dose difference in this profile. Agreement in the profile shown in (a) is within +2.5% and -0.5% and agreement in (b) is +10.5% and -1.0% for all points.

3.3.1 Checkerboard Phantom (2 cm x 2 cm)

For a 250 MeV, 4x4 cm^2 beam in our 2 cm x 2 cm checkerboard phantom, pass rates were 99.0% (PM) vs 84.0% (OM) (Figure 3.31). Additionally, dose difference maps and histograms are shown in Figure 3.32. To better evaluate how well the PM improved compared to the limitations imposed by the CAXSIS approximation in the OM, we observed depth dose profiles (x = +/- 1 cm) and a lateral dose profile just below the checkered slab configuration (z = 34.05 cm). Comparing the depth dose profiles at x = -1 cm for both models (Figure 3.33), the PM is shown to agree within +3.0% and -4.5% relative to MC, whereas the OM agrees within +3.0% to -10.5% of MC; furthermore, the -10.5% percent difference seen with the OM is at the peak. At x = 1 cm (Figure 3.33), the depth profile shows a similar result: the PM percent differences range from +4.0% to -3.0% and the OM ranges from +2.0% to -12.5%, again with the -12.5% at the peak. These differences are mostly due to the CAXSIS approximation applied to the OM whereas the PM is not dependent on this approximation. To a lesser extent, these differences are impacted by the differences in material-dependence of the nuclear halo between the PM and OM.

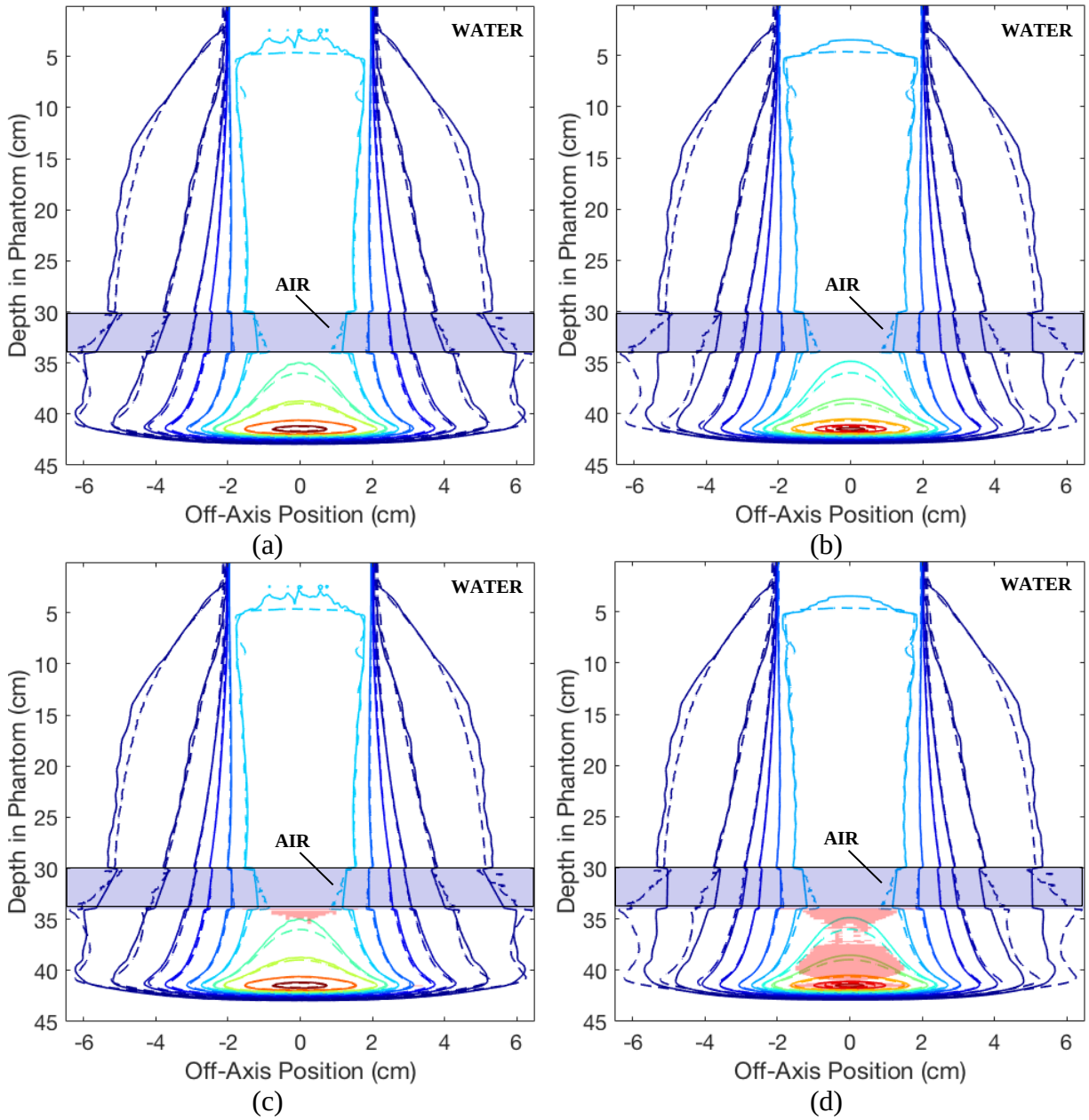

Figure 3.23. Isodose (1, 2, 5, 10, 20, 30, 40, 50, 70, 90, and 100%) comparisons for a 250 MeV, 4x4 cm^2 beam in a water phantom with a 4 cm air slab at *z=30 cm* (translucent blue rectangle). Shown using (a,c) the PM (solid) vs MC (dashed), and (b,d) OM (solid) vs MC (dashed). Pass rates were 98.6% (a,c) and 85.6% (b,d). Areas of failure are indicated in translucent red shading.

From the lateral profile comparisons (Figure 3.34), it can be seen that the PM accounted for the interface between bone and air heterogeneities whereas the OM smoothed out the dose at the interfaces. The percent difference for this profile in the PM was within +5.5% to -2.0% whereas the OM was within +3.5% to -5.0%. The DTA of the 1% isodose line between the PM and MC in the checkered slabs improved by 0.5 mm, and further downstream improved by 0.84 to 0.85 mm relative to the DTA between OM and MC.

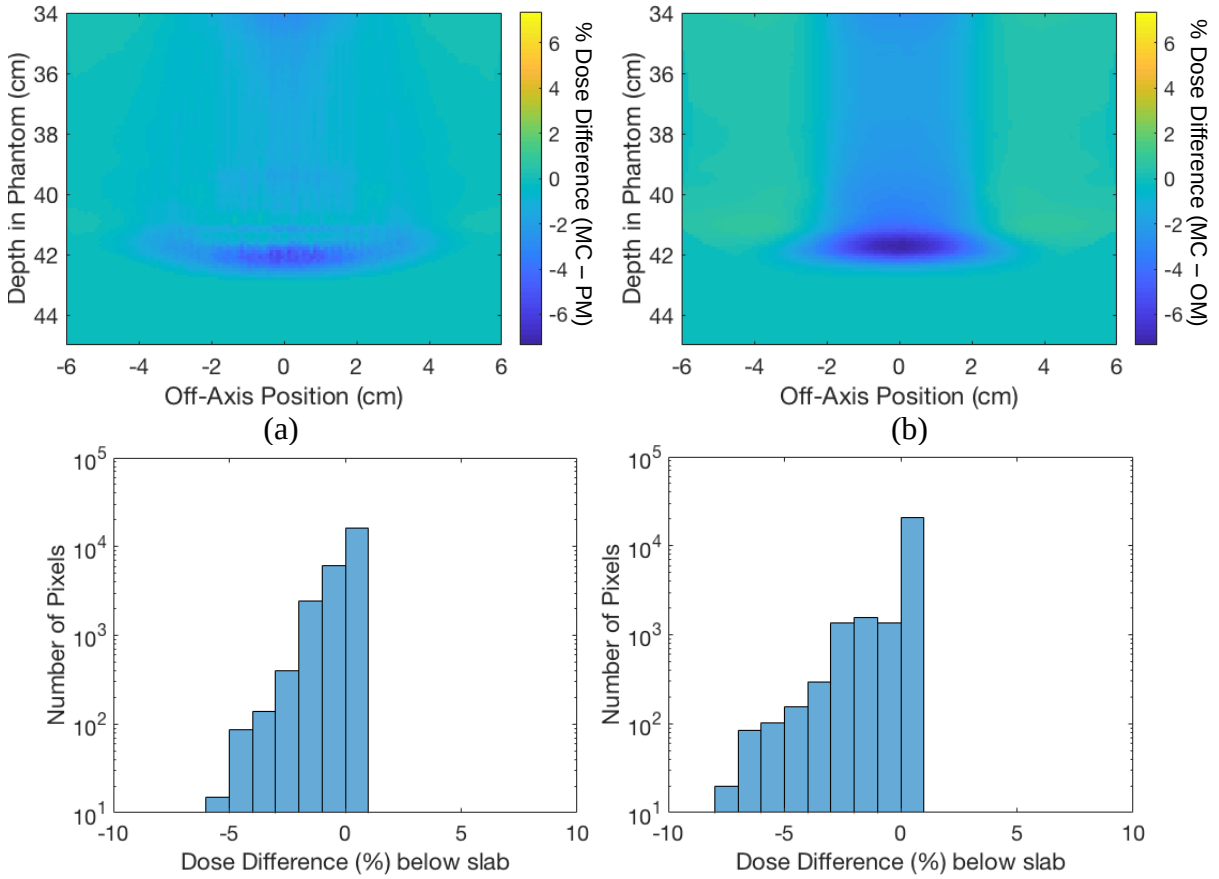

Figure 3.24. Dose difference maps between the PM and MC (a) and between OM and MC (b) for the 4 cm laterally infinite air slab at z = 30 cm (Figure 3.23). Note that dose differences in all panels of this figure are only calculated below the slab. Both dose difference maps use the same color scale, which is indicated in the bars to the right of (a) and (b). This data is also histogrammed for the PM vs MC (c) and OM vs MC (d).

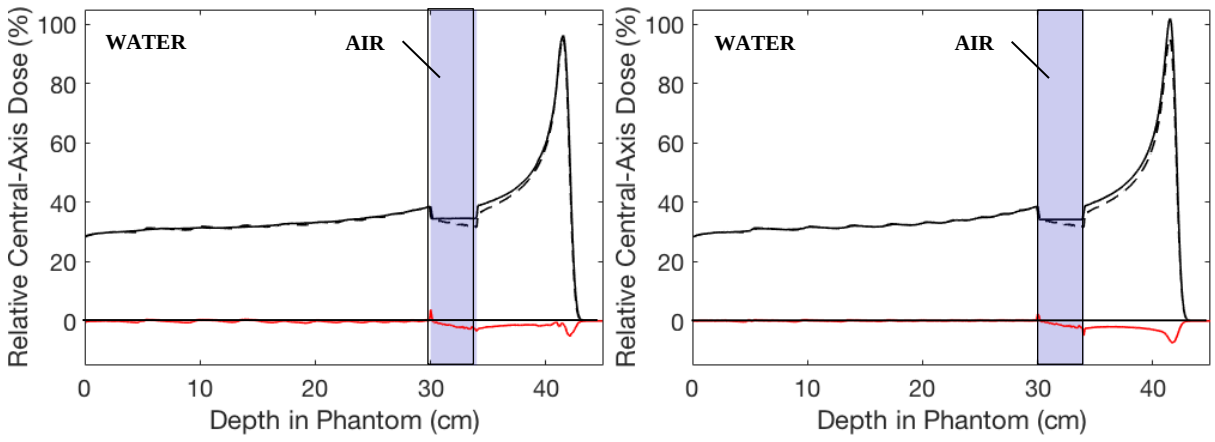

Figure 3.25. Central-axis depth dose profiles for the 4 cm laterally infinite air slab at z = 30 cm (Figure 3.23). Data shown using (a) PM (solid) vs MC (dashed), and (b) OM (solid) vs MC (dashed). The air slab in both plots is indicated as a translucent blue rectangle. The red plot in each panel indicates dose difference in this profile. Agreement in the profile shown in (a) is within +4.0% and -5.0% and agreement in (b) is +2.5% and -7.5% for all points.

For a SOBP (with 5 cm of range modulation), 4x4 cm^2 beam in our 2 cm x 2 cm checkerboard phantom, pass rates for this geometry were 94.0% (PM) vs 65.0% (OM) (Figure 3.35). Additionally, dose difference maps and histograms are shown in Figure 3.36. To better evaluate how well the PM improved compared to the central-axis approximation limitation of the OM, we observed depth profiles (x = +/- 1 cm) and a lateral profile just below the checkered slab configuration (z = 34.5 cm). Comparing the depth profiles at x = -1 cm for both models (Figure 3.37), the PM is shown to have percent differences within +2.5% and -5.0% whereas the OM ranges from 2.0% to -12.5%; furthermore, the -12.5% percent difference seen with the OM seems to be at the peak. At x = 1 cm (Figure 3.37), the depth profile shows a similar result: the PM percent differences range from +2.0% to -6.5% and the OM ranges from +0.5% to -15.0%, again with the -15.0% at the peak. From the lateral profile comparisons (Figure 3.38), the profiles make it clear that the PM accounts for the interface between bone and air heterogeneities whereas the OM smooths out the dose at the interfaces. For this lateral profile, the percent difference in the PM is within +4.0% and -8.5% whereas the OM ranges from +1.0% to -17.5%. The improvement of the PM over the OM was more pronounced for a SOBP compared to the monoenergetic beam. The errors observed in the monoenergetic case, therefore, did not average out with energy modulation, but actually worsened, at least in the OM. The DTA of the 1% isodose line between PM and MC at the distal edge of the checkered heterogeneity and beyond improved by 0.8 mm relative to the DTA between OM and MC.

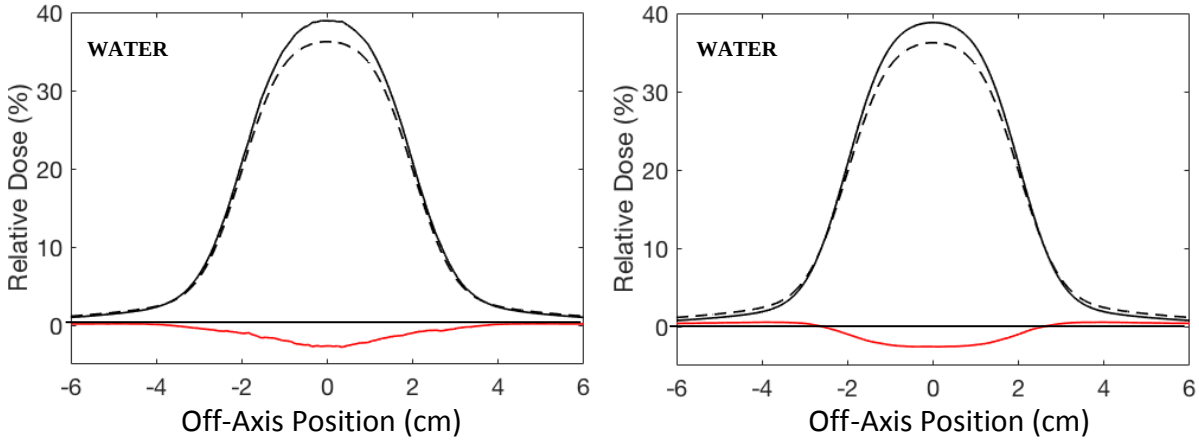

Figure 3.26. Lateral dose profiles taken at z = 34.5 cm for the 4 cm laterally infinite air slab at z = 30 cm (Figure 3.23). Data shown using (a) PM (solid) vs MC (dashed), and (b) OM (solid) vs MC (dashed). The red plot in each panel indicates dose difference in this profile. Agreement in the profiles are within 0.5% to -3.0% for (a) and (b).

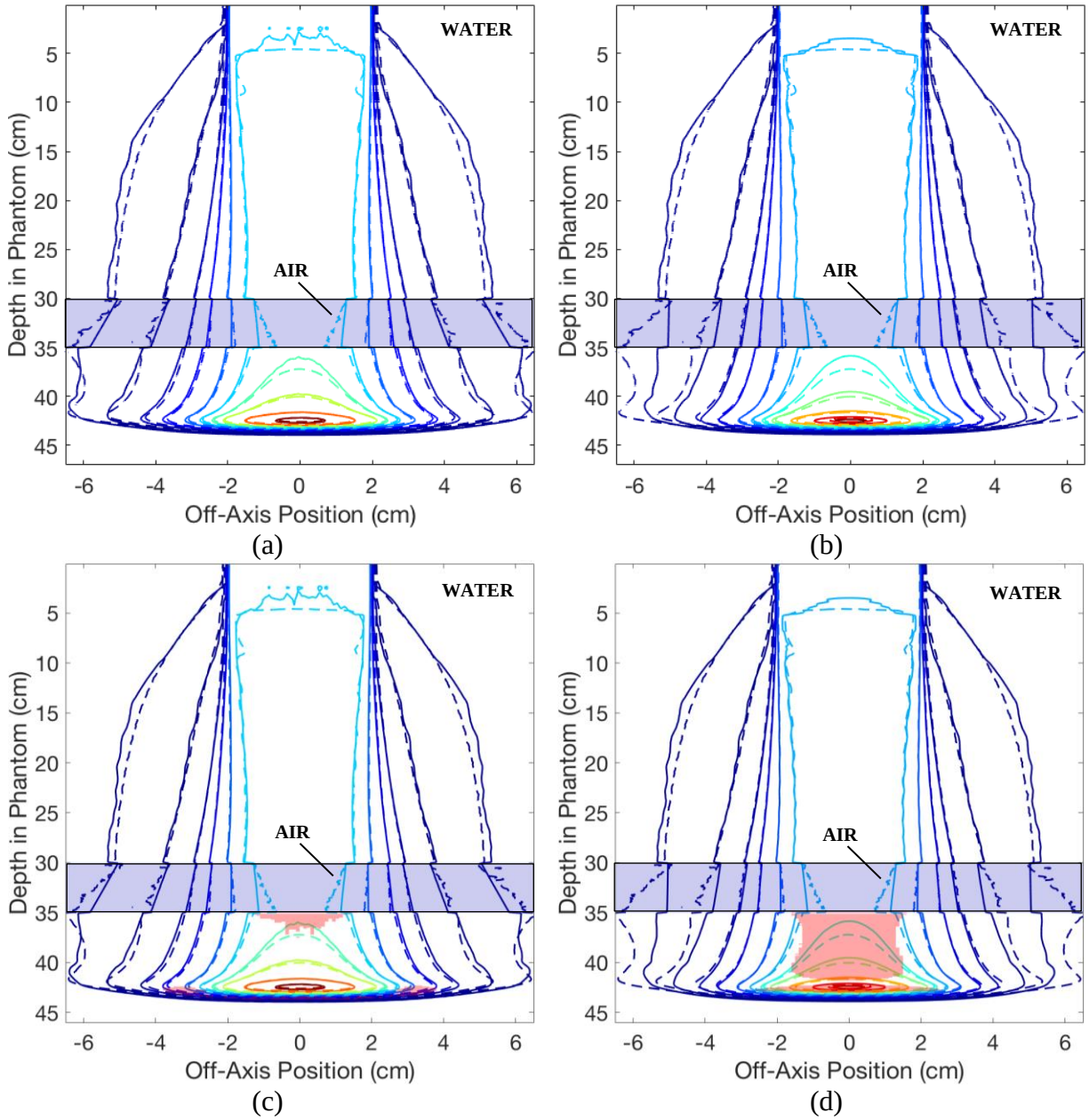

Figure 3.27. Isodose (1, 2, 5, 10, 20, 30, 40, 50, 70, 90, and 100%) comparisons for a 250 MeV, 4x4 cm^2 beam in a water phantom with a 5 cm air slab at *z=30 cm* (translucent blue rectangle). Shown using (a,c) the PM (solid) vs MC (dashed), and (b,d) OM (solid) vs MC (dashed). Pass rates were 94.6% (a) and 78.5% (b). Areas of failure are indicated in red shading.

3.3.2 Prostate Phantom

For a 250 MeV, 4x4 cm^2 beam in the prostate phantom, pass rates were 96.0% (PM) vs 77.5% (OM) (Figure 3.39). Dose difference maps and histograms are shown in Figure 3.40. Virtually all the failing regions in Figure 3.39 have corresponding percent differences up to +/-10% in Figure 3.40. Most evident in Figure 3.40 is the degradation of the Bragg peak in both the femoral head and rectal heterogeneity when predicted by the OM.

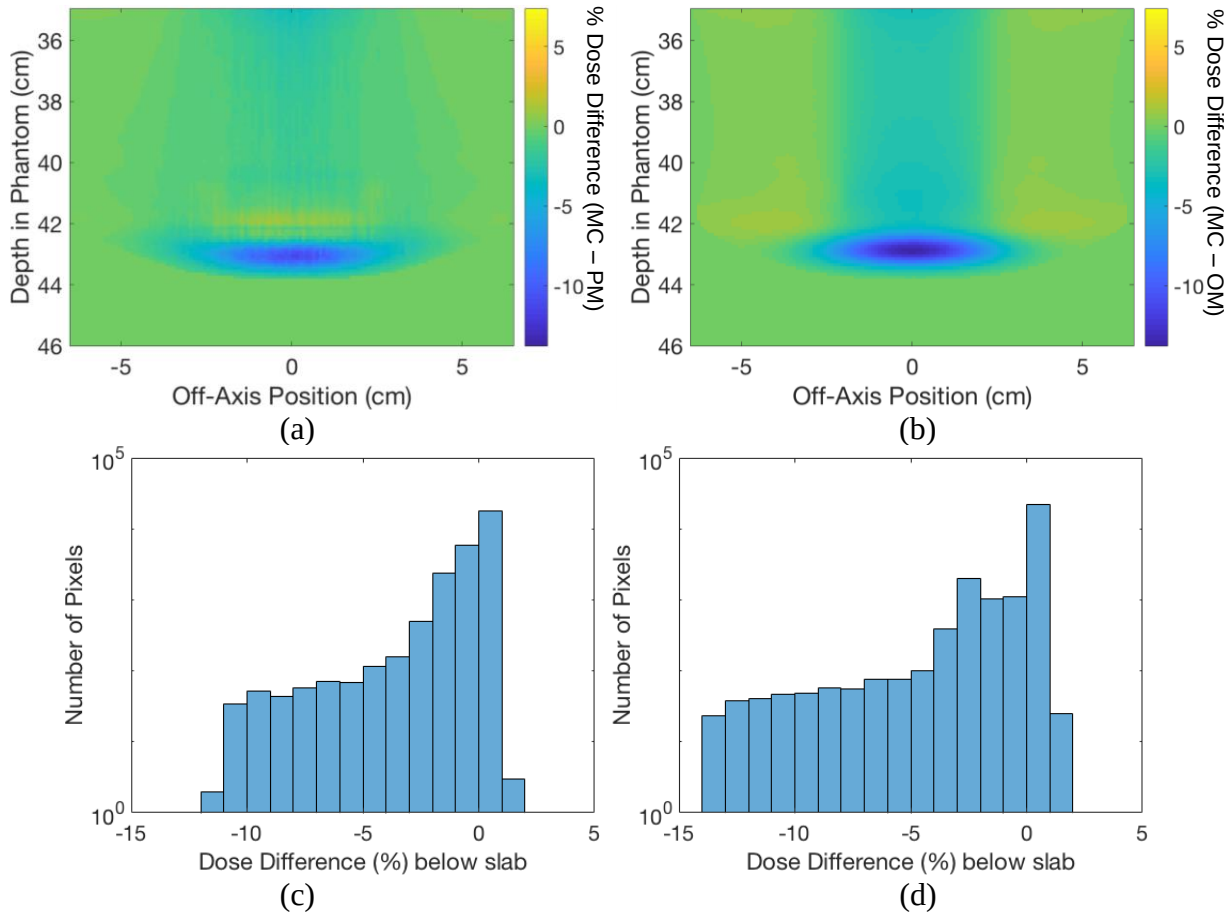

Figure 3.28. Dose difference maps between the PM and MC (a) and between OM and MC (b) for the 5 cm laterally infinite air slab at z = 30 cm (Figure 3.27). Note that dose differences in all panels of this figure are only calculated below the slab. Both dose difference maps use the same color scale, which is indicated in the bars to the right of (a) and (b). This data is also histogrammed for the PM vs MC (c) and OM vs MC (d).

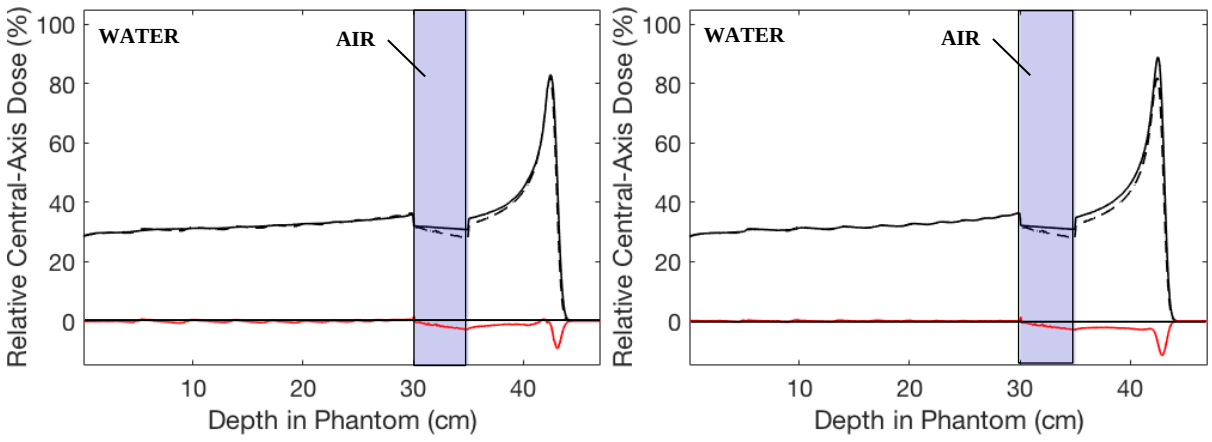

Figure 3.29. Central-axis depth dose profiles for the 5 cm laterally infinite air slab at z = 30 cm (Figure 3.27). Data shown using (a) PM (solid) vs MC (dashed), and (b) OM (solid) vs MC (dashed). The air slab in both plots is indicated as a translucent blue rectangle. The red plot in each panel indicates dose difference in this profile. Agreement in the profile shown in (a) is within +1.5% and -9.5% and agreement in (b) is +1.5% and -11.5% for all points.

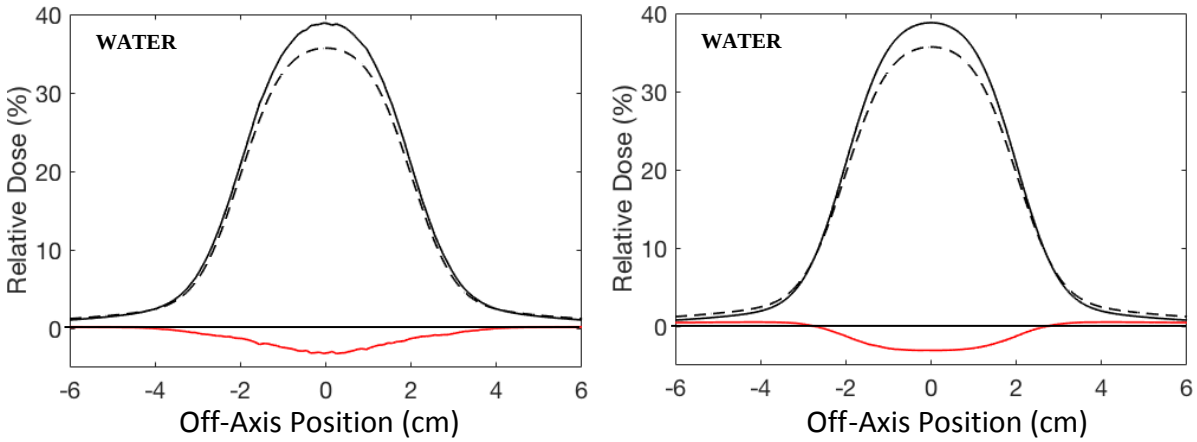

(a) (b)

Figure 3.30. Lateral dose profiles taken at z = 35.05 cm for the 5 cm laterally infinite air slab at z = 30 cm (Figure 3.27). Data shown using (a) PM (solid) vs MC (dashed), and (b) OM (solid) vs MC (dashed). The red plot in each panel indicates dose difference in this profile. Agreement in the profiles are within 0.5% to -3.5% for (a) and (b).

Table 3.4. Results for evaluation geometries in Specific Aim 3. Columns in the table indicate the percentage of points passing our criteria of 3% or 1 mm, and the improvement (negative values: worsening) in the DTA of the 1% isodose line (calculated by subtracting the DTA of the OM vs MC from the DTA of the PM vs MC).

GEOMETRY	Passrate (3% or 1 mm)		DTA improvement at 1% (PM - OM)	
	PM (%)	OM (%)	Distal Slab Edge (mm)	Beyond Slab (mm)
Checkerboard Phantom (Monoenergetic)	99.0	84.0	0.5	0.84 to 0.85
Checkerboard Phantom (SOBP)	94.0	65.0	0.8	0.8
Prostate Phantom (Monoenergetic)	96.0	77.5	2.1 at z = 30.05 cm	
Prostate Phantom (SOBP)	99.4	99.0	2.9 at z = 30.05 cm	

To better evaluate how well the PM improved compared to the central-axis approximation limitation of the OM, we observed a central-axis profile and a lateral profile just below the rectal heterogeneity (z = 30 cm). Comparing the central-axis profiles for both models (Figure 3.41), the PM is shown to have percent differences within +1.5% and -5.0% whereas the OM ranges from +9.5% to -15.5%; furthermore, there is significant degradation in the Bragg peak by the OM. From the lateral profile comparisons (Figure 3.42), it is clear that the PM accounts for the interface between the air heterogeneity of the rectum and water, whereas the OM smooths out the dose at the interfaces. For this lateral profile, the percent difference in the PM is within +1.0% and -0.5% whereas the OM ranges from +1.0% to -1.5%.

Additionally, the DTA of the 1% isodose line between the PM and MC distal to both the femoral head and rectum heterogeneity (z = 30.05 cm) improved by 2.1 mm relative to the DTA between OM and MC. Further downstream, the DTA of the 1% isodose line improved between 0.9 mm to 2.7 mm.

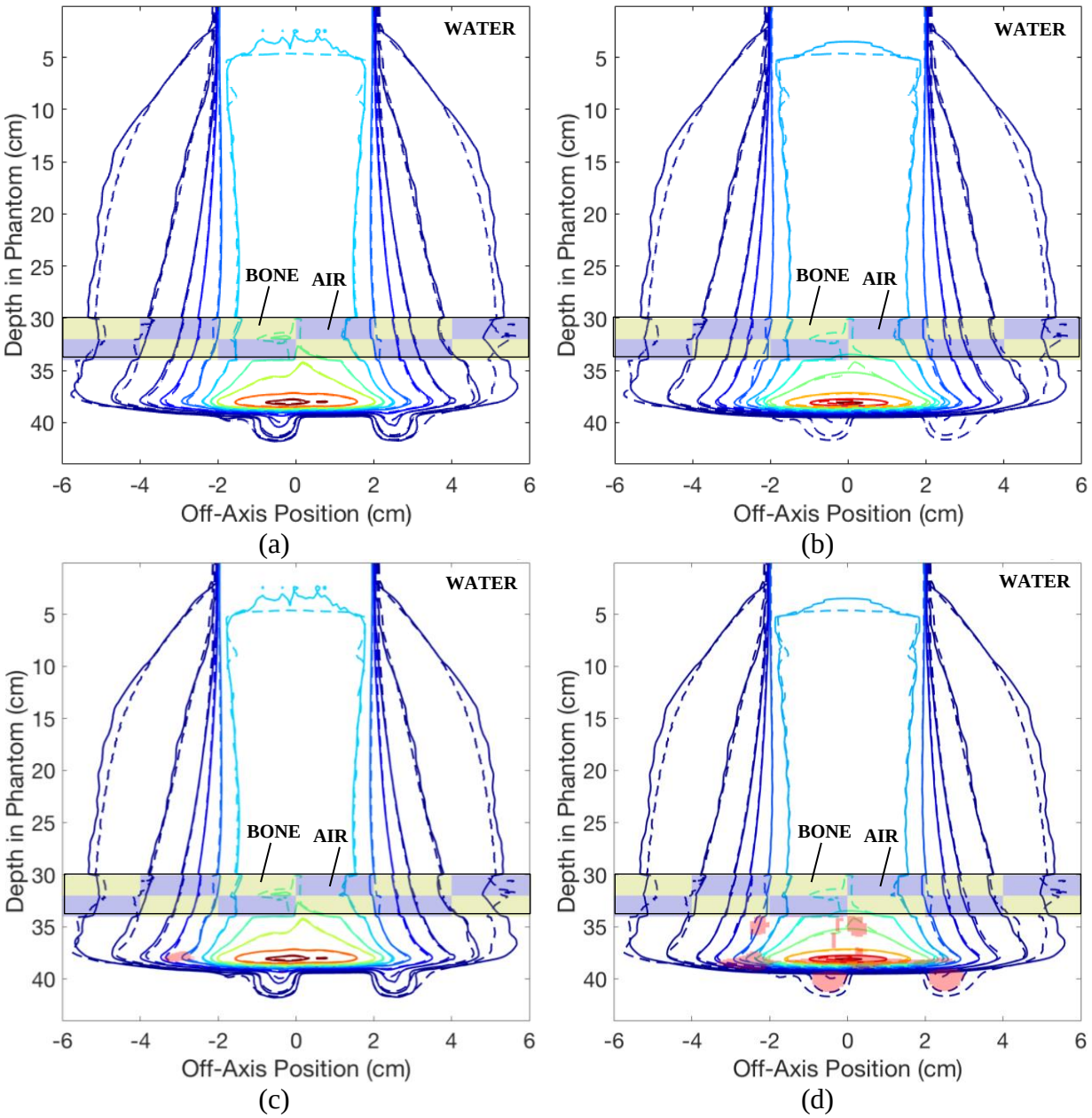

Figure 3.31. Isodose (1, 2, 5, 10, 20, 30, 40, 50, 70, 90, and 100%) comparisons for a 250 MeV, 4x4 cm^2 beam in a water phantom with a 2 cm wide by 2 cm deep alternating air / bone checkerboard phantom at *z=30 cm.* The air slabs are indicated by translucent blue rectangles whereas bone slabs are indicated in yellow. Shown using (a,c) the PM (solid) vs MC (dashed), and (b,d) OM (solid) vs MC (dashed). Pass rates were 99.0% (a,c) and 84.0% (b,d) and areas of failure are indicated in red shading (c,d).

For a SOBP (5 cm of range modulation), 4x4 cm^2 beam in our prostate phantom, pass-rates were 89.0% (PM) vs 57.0% (OM) (Figure 3.43). Dose difference maps and histograms are shown in Figure 3.44. Virtually all failing regions for the OM in Figure 3.44 have corresponding areas of percent differences up to ~+/-15% in Figure 3.43. Most evident in Figure 3.45 is the degradation of the distal end of the SOBP from both the femoral head heterogeneity and the laterally finite rectum heterogeneity in the OM.

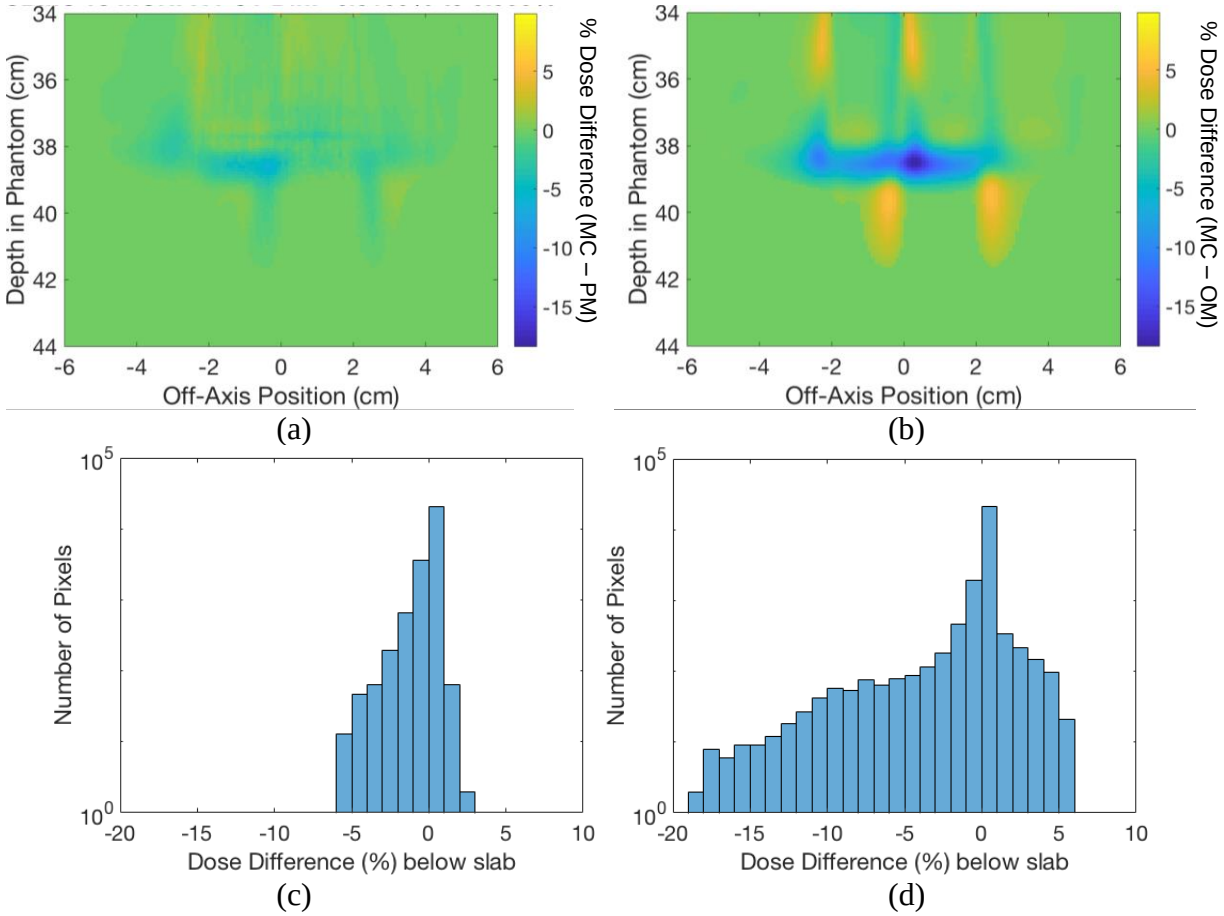

Figure 3.32. Dose difference maps between the PM and MC (a) and between OM and MC (b) for the checkerboard phantom (Figure 3.31). Note that dose differences in all panels of this figure are only calculated below the slab. Both dose difference maps use the same color scale, which is indicated in the bars to the right of (a) and (b). This data is also histogrammed for the PM vs MC (c) and OM vs MC (d).

To better evaluate how well the PM improved compared to the central-axis approximation limitation of the OM, we observed a central-axis profile and a lateral profile below the rectal heterogeneity and below the distal 90% line of the SOBP (z = 31.75 cm). Comparing the central-axis profiles for both models (Figure 3.45), the PM is shown to have percent differences within +1.5% and -6.0% whereas the OM ranges from +2.5% to -28%; furthermore, there is degradation of the Bragg peak as calculated by the OM. From the lateral profile comparisons (Figure 3.46), it is clear that the PM accounts for the interface between the rectal edge and water, whereas the OM smooths out the dose at interfaces. For the lateral profile, the percent difference in the PM is within +3.5% and -5.5% whereas the OM ranges from +1.0% to -5.0%. Most of the differences between the PM and OM are due to limitations imposed by the CAXSIS approximation and a lack of material dependence for the nuclear halo term.

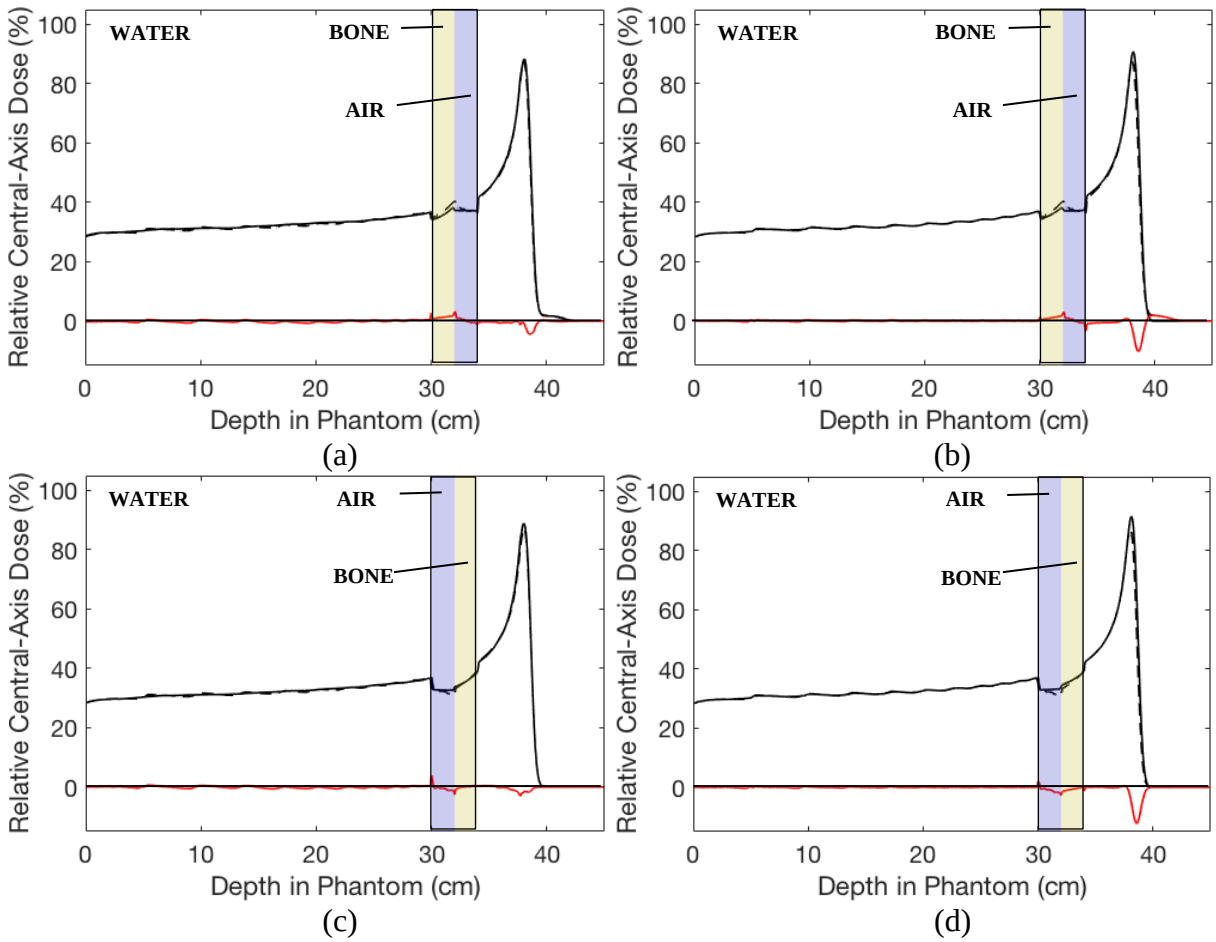

Figure 3.33. Depth dose profiles at x = -1 cm (a,b) and x = 1 cm (c,d) for the checkerboard phantom (Figure 3.31). Data shown using (a,c) PM (solid) vs MC (dashed), and (b,d) OM (solid) vs MC (dashed). The air slab is indicated by a translucent blue rectangle and the bone slab is in yellow. The red plot in each panel indicates dose difference in this profile. Agreement in the profiles is within +3.0% to -4.5% (a), +3.0% to -10.5% (b), +4.0% to -3.0% (c), and +2.0% to -12.5%.

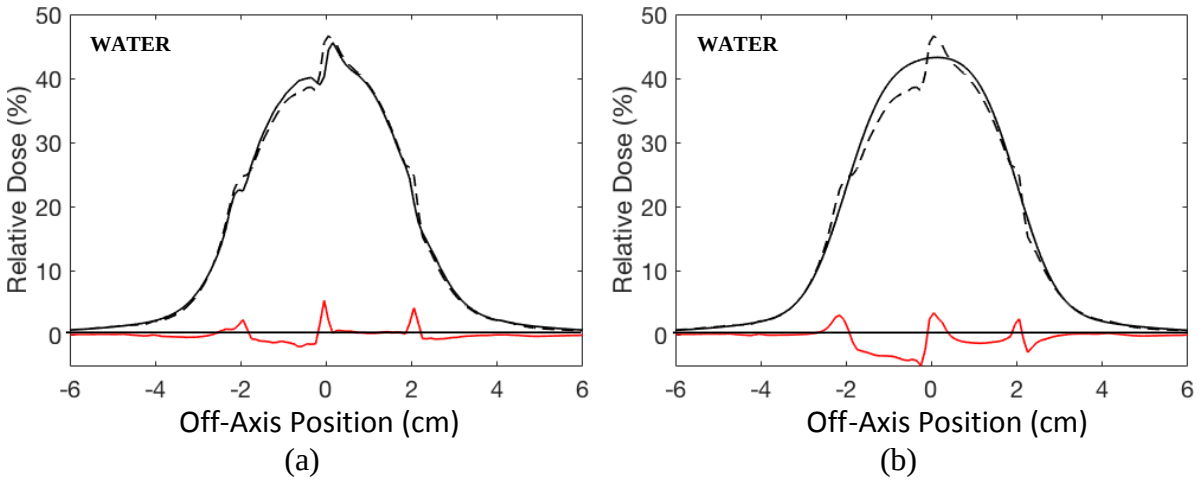

Figure 3.34. Lateral dose profiles at *z=34.05* cm for (a) the PM (solid black) vs MC (dashed), and (b) OM (solid black) vs MC (dashed) for the checkerboard phantom (Figure 3.31). The red plot in each panel indicates dose difference in this profile. The dose difference in (a) is within +5.5% to -2.0% and (b) within +3.5% to -5.0%.

Additionally, the results indicated that the DTA of the 1% isodose line between the PM and MC distal to both the femoral head and rectum heterogeneity (z = 30.05 cm) improved by 2.9 mm relative to the DTA between OM and MC. Further downstream, the DTA of the 1% isodose line between the PM and MC was overestimated by up to 1.3 mm but reached improvements up to 7.2 mm.

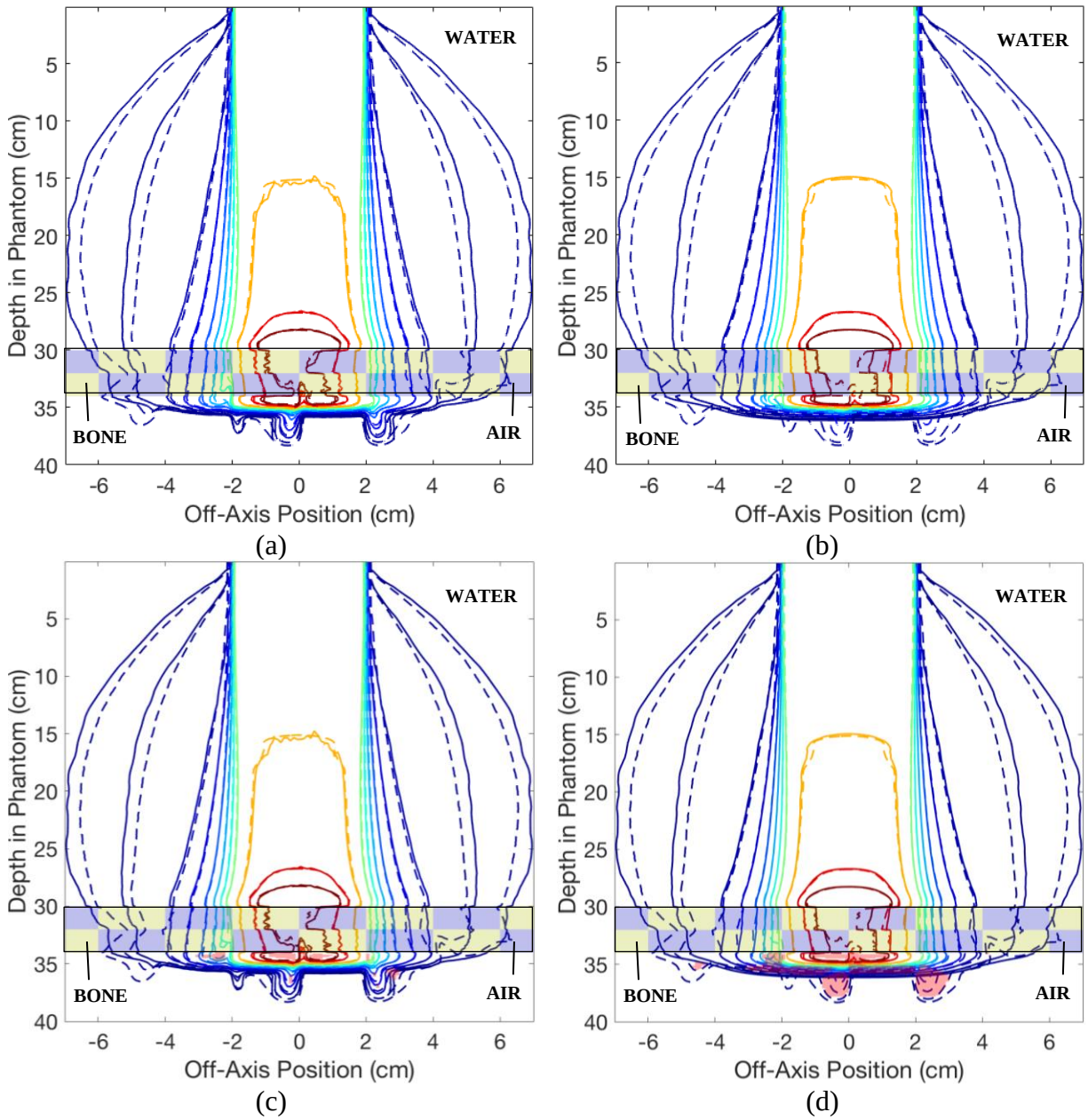

Figure 3.35. Isodose (1, 2, 5, 10, 20, 30, 40, 50, 70, 90, and 100%) comparisons for a SOBP (216-236 MeV in 2 MeV steps (5 cm of range modulation)), 4x4 cm^2 beam in a water phantom with a 2 cm wide by 2 cm deep alternating air / bone checker phantom at *z=30 cm.* The air slabs are indicated by translucent blue rectangles whereas bone slabs are indicated in yellow. Shown using (a,c) the PM (solid) vs MC (dashed), and (b,d) OM (solid) vs MC (dashed). Pass rates were 94.0% (a,c) and 65.0% (b,d) and areas of failure are indicated in red shading (c,d).

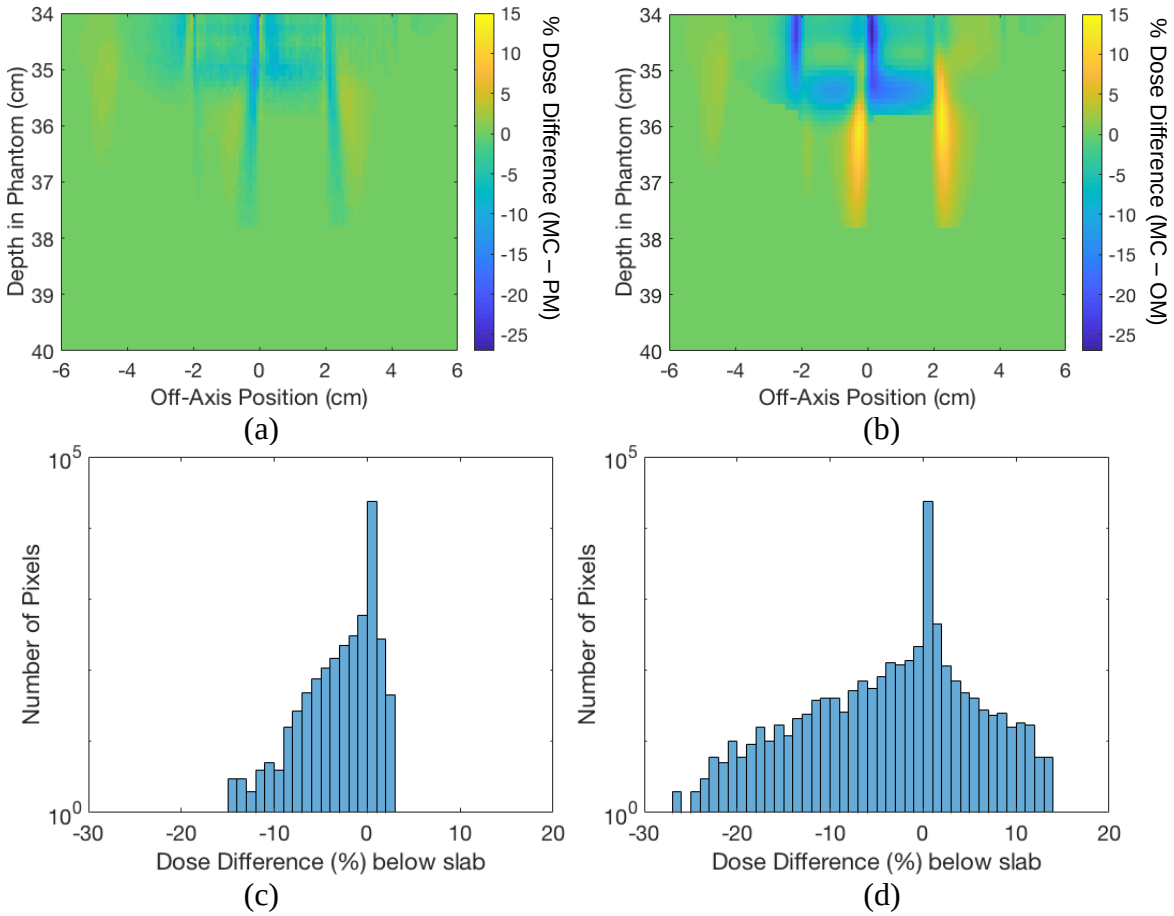

Figure 3.36. Dose difference maps between the PM and MC (a) and between OM and MC (b) for the checkerboard phantom and the SOBP beam in Figure 3.35. Note that dose differences in all panels of this figure are only calculated below the slab. Both dose difference maps use the same color scale, which is indicated in the bars to the right of (a) and (b). This data is also histogrammed for the PM vs MC (c) and OM vs MC (d).

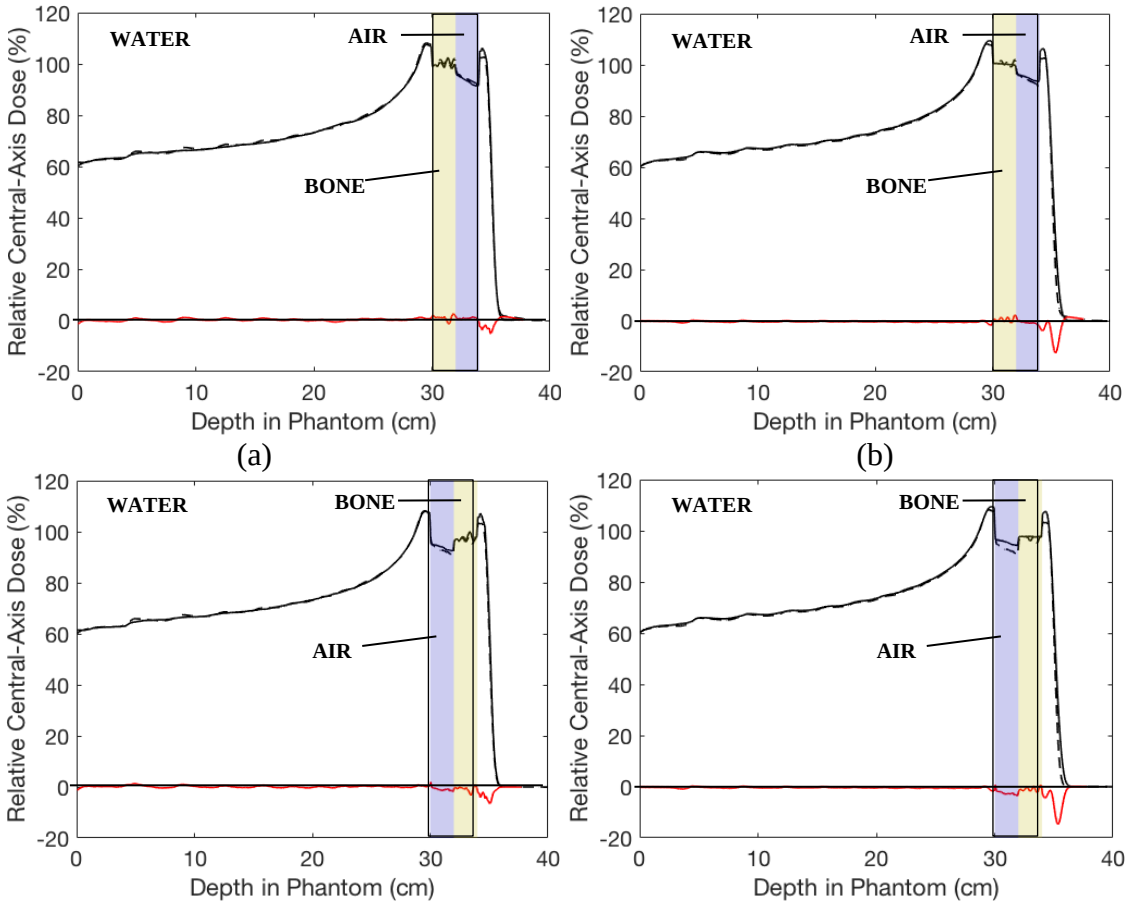

Figure 3.37. Depth dose profiles at x = -1 cm (a,b) and x = 1 cm (c,d) for the checkerboard phantom and the SOBP beam in Figure 3.35. Data shown using (a,c) PM (solid) vs MC (dashed), and (b,d) OM (solid) vs MC (dashed). The air slab is indicated by a translucent blue rectangle and the bone slab is in yellow. The red plot in each panel indicates dose difference in this profile. Agreement in the profiles is within +2.5% to -5.0% (a), +2.0% to -12.5% (b), +2.0% to -6.5% (c), and +0.5% to -15.0% (d).

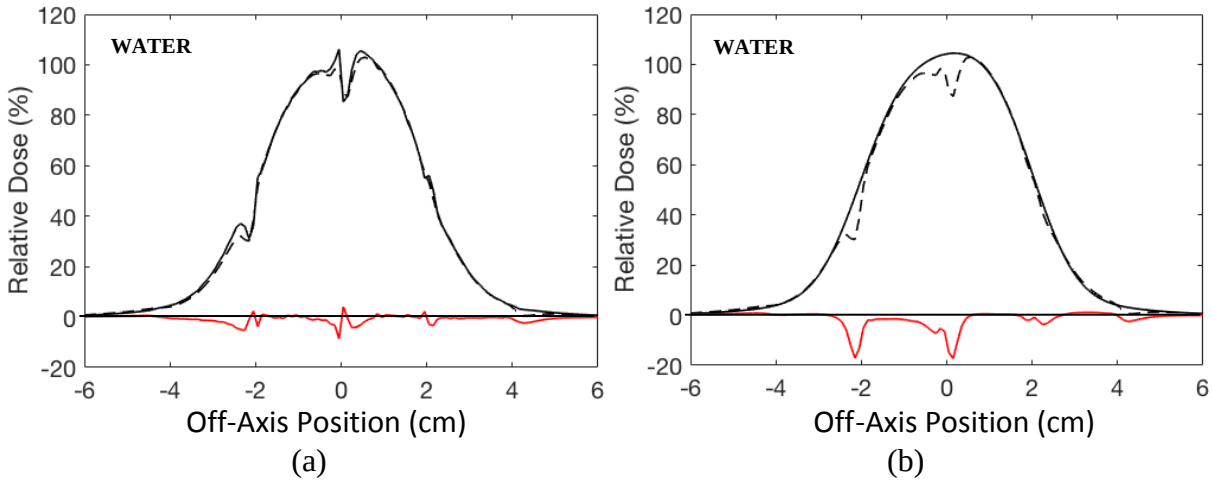

Figure 3.38. Lateral dose profiles at *z=34.5* cm for (a) the PM (solid black) vs MC (dashed), and (b) OM (solid black) vs MC (dashed) for the geometry in Figure 3.35. The red plot in each panel indicates dose difference in this profile. The dose difference in (a) is within +4.0% to -8.5% and (b) within +1.0% to -17.5%.

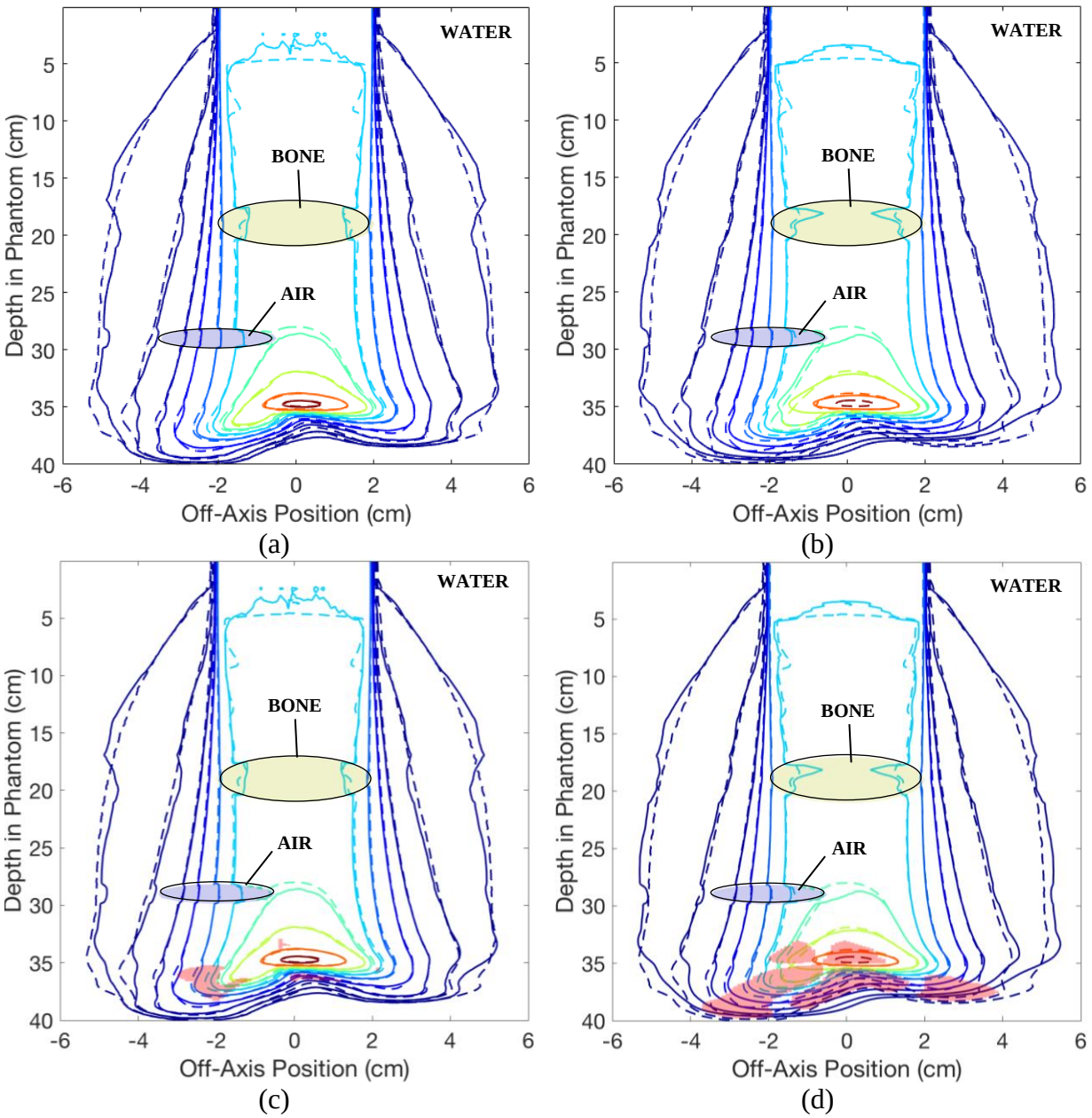

Figure 3.39. Isodose (1, 2, 5, 10, 20, 30, 40, 50, 70, 90, and 100%) comparisons for a 250 MeV, 4x4 cm^2 beam in a prostate phantom with a bone heterogeneity (femoral head) modeled by a 2 cm radius circle centered at z = 19 cm (yellow), an air heterogeneity (rectum) modeled by an ellipse (major axis: 2.98 cm, minor axis: 1.71 cm) centered at z = 29 cm (blue). Shown using (a, c) the PM (solid) vs MC (dashed), and (b, d) OM (solid) vs MC (dashed). Pass rates were 96.0% (a, c) and 77.5% (b, d).

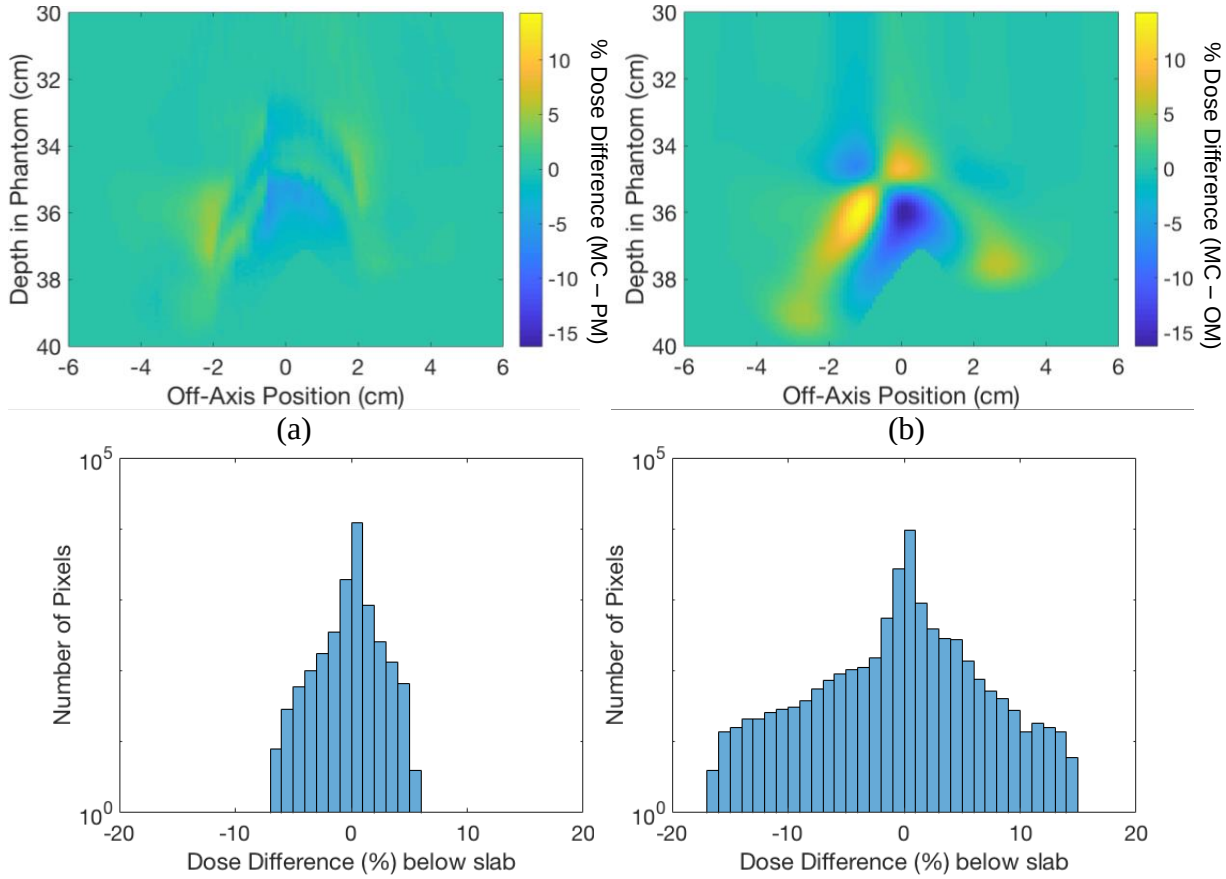

Figure 3.40. Dose difference maps between the PM and MC (a) and between OM and MC (b) for the prostate phantom (Figure 3.39). Note that dose differences in all panels of this figure are only calculated below the slab. Both dose difference maps use the same color scale, which is indicated in the bars to the right of (a) and (b). This data is also histogrammed for the PM vs MC (c) and OM vs MC (d).

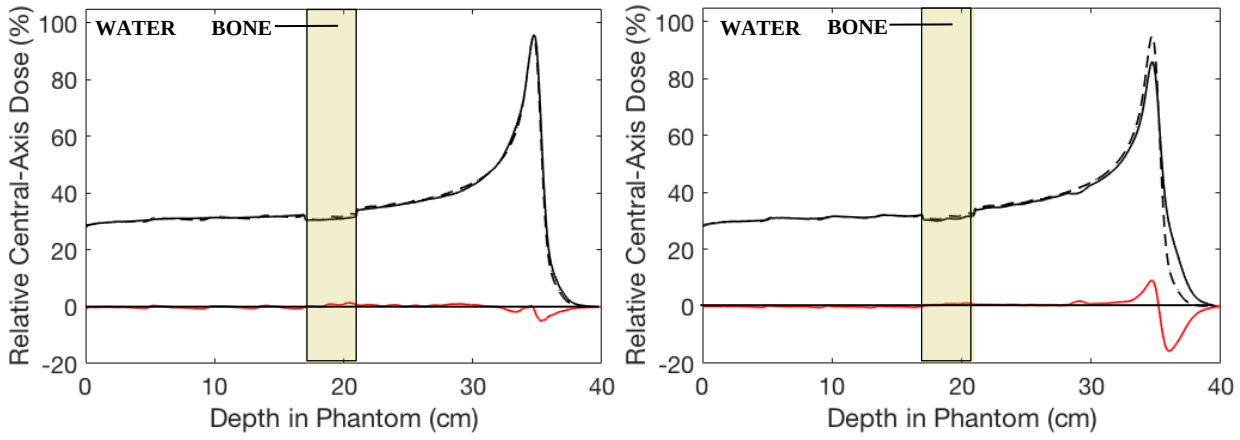

Figure 3.41. Central-axis depth dose profiles for the prostate phantom (Figure 3.39). Data shown using (a) PM (solid) vs MC (dashed), and (b) OM (solid) vs MC (dashed). The femoral head heterogeneity in both plots is indicated as a translucent yellow. The red plot in each panel indicates dose difference in this profile. Agreement in the profile shown in (a) is within +1.5% and -5.0% and agreement in (b) is +9.5% and -15.5% for all points.

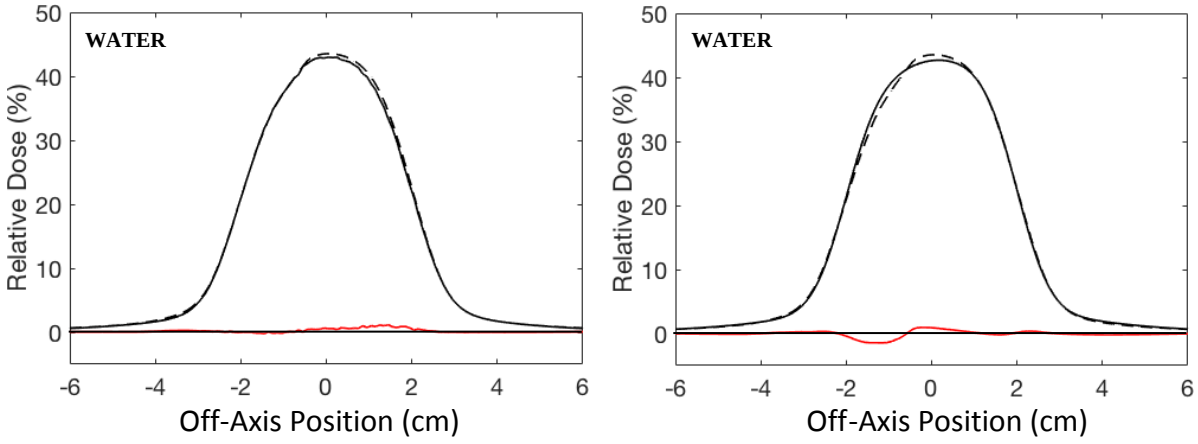

(a) (b)

Figure 3.42. Lateral dose profiles under the rectum heterogeneity at z = 30 cm for the prostate phantom (Figure 3.39). Data shown using (a) PM (solid) vs MC (dashed), and (b) OM (solid) vs MC (dashed). The red plot in each panel indicates dose difference in this profile. Agreement in the profile in (a) is within +1.0% and -0.5% and agreement in (b) is within +1.0% and -1.5%.

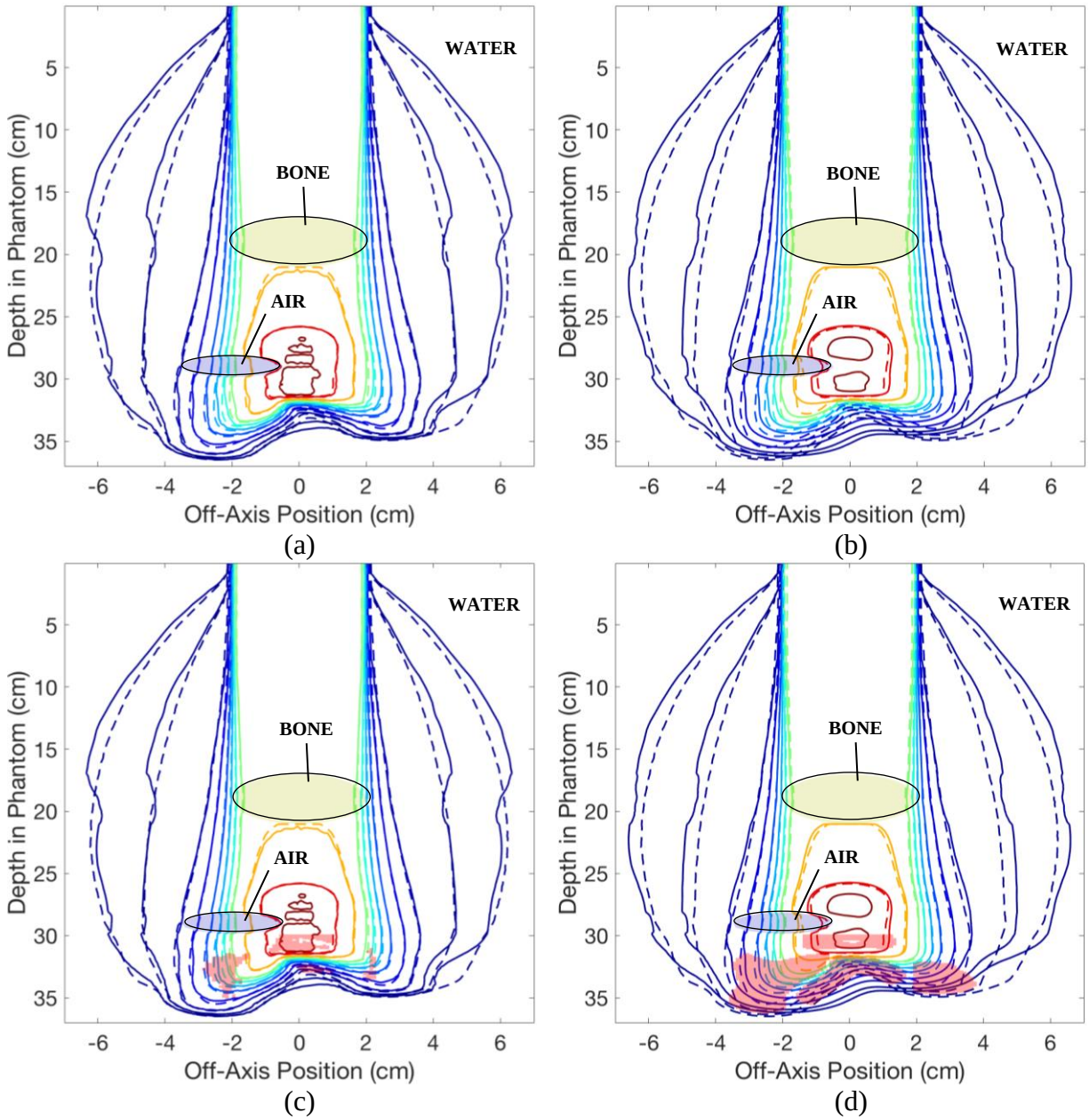

Figure 3.43. Isodose (1, 2, 5, 10, 20, 30, 40, 50, 70, 90, and 100%) comparisons for a SOBP (216-236 MeV) in 2 MeV steps (5 cm of range modulation)), 4x4 cm^2 beam in a prostate phantom with a bone heterogeneity (femoral head) modeled by a 2 cm radius circle centered at z = 19 cm (yellow), an air heterogeneity (rectum) modeled by an ellipse (major axis: 2.98 cm, minor axis: 1.71 cm) centered at z = 29 cm (blue). Shown using (a,c) PM (solid) vs MC (dashed), and (b,d) OM (solid) vs MC (dashed). Pass rates were 89.0% (a,c) and 57.0% (b,d).

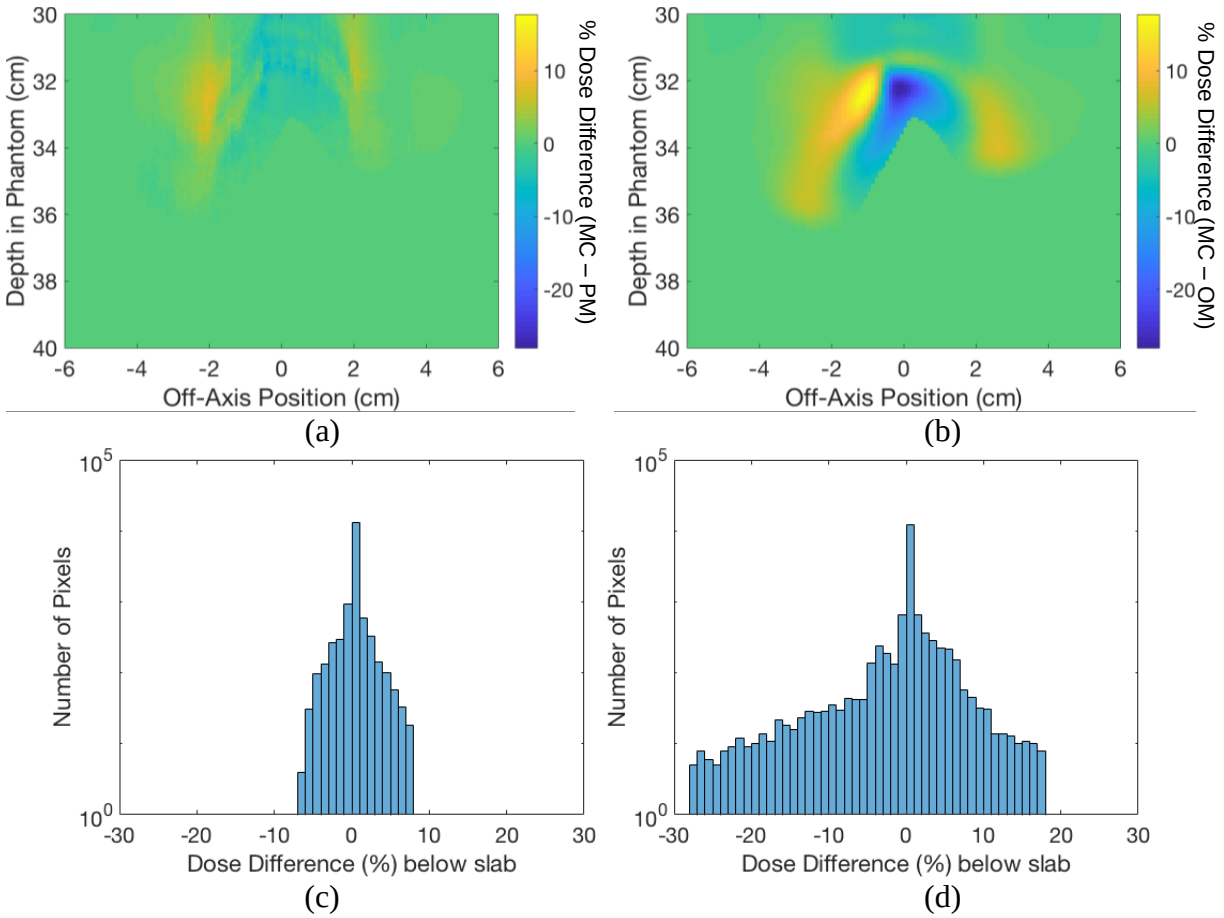

Figure 3.44. Dose difference maps between the PM and MC (a) and between OM and MC (b) for the prostate phantom and SOBP in Figure 3.43. Note that dose differences in all panels of this figure are only calculated below the slab. Both dose difference maps use the same color scale, which is indicated in the bars to the right of (a) and (b). This data is also histogrammed for the PM vs MC (c) and OM vs MC (d).

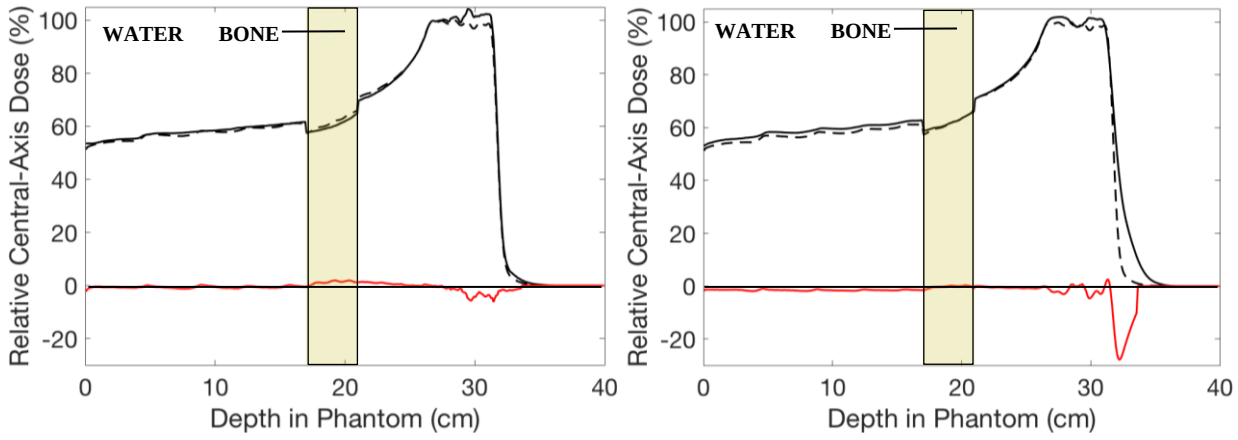

Figure 3.45. Central-axis depth dose profiles for the prostate phantom and SOBP in Figure 3.43. Data shown using (a) PM (solid) vs MC (dashed), and (b) OM (solid) vs MC (dashed). The femoral head heterogeneity in both plots is indicated in translucent yellow. The red plot in each panel indicates dose difference in this profile. Agreement in the profile shown in (a) is within +1.5% and -6.0% and agreement in (b) is +2.5% and -28.0% for all points.

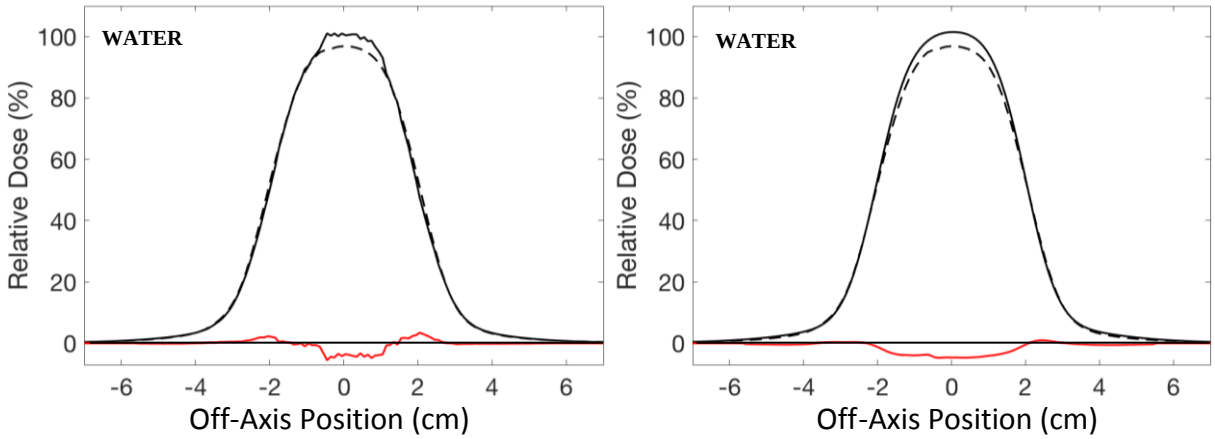

(a) (b)

Figure 3.46. Lateral dose profiles under the rectum heterogeneity at z = 31.75 cm for the prostate phantom and SOBP in Figure 3.43. Data shown using (a) PM (solid) vs MC (dashed), and (b) OM (solid) vs MC (dashed). The red plot in each panel indicates dose difference in this profile. Agreement in the profile in (a) is within +3.5% and -5.5% and agreement in (b) is within +1.0% and -5.0%.

CHAPTER 4. DISCUSSION

In this work, we developed a stochastic dose calculation model that eliminated the CAXSIS approximation in calculating primary dose (Specific Aim 1) and added material-dependence to the calculation of the nuclear halo of secondary protons (Specific Aim 2).

Removing the CAXSIS approximation in our primary transport model was shown to significantly reduce dose difference below laterally finite heterogeneities compared to the previous model (Chapman *et al* 2017), and robust material-dependence in the nuclear halo resulted in significant improvements in the dose difference below laterally infinite heterogeneities compared to the previous one-dimensional implementation. Overall, resulting dose differences and distances-to-agreement were shown to improve agreement with Monte Carlo data in a wide variety of geometries (Specific Aims 1, 2, and 3) compared to Chapman *et al* (2017).

Our study provided new insight into the basic physics of material-dependence in the nuclear halo. Transport of secondary particles through heterogeneities was shown to be more accurately modeled by the material dependent nuclear halo in this work compared to the original, one-dimensional implementation. This improvement resulted in decreased dose differences using the present model compared to the original model. Our results strongly suggest that robust material dependence in the nuclear halo will be important in heterogeneous patient anatomy. For instance, a rectal heterogeneity in a prostate treatment plan for a large patient could have a diameter on the order of 4-5 cm, which our results indicate would cause significant dose errors beyond the heterogeneity using the original model.

In our previous study (Chapman *et al* 2017), we reported large dose differences between the PBA and Monte Carlo calculations in volumes downstream of thick heterogeneities, particularly air slabs. Correspondingly, the improvement of the present model relative to the PBA was most significant following large air heterogeneities.

Dose differences calculated by the present geometry indicated higher accuracy compared to the Tourovsky *et al* (2005) model. For instance, in all geometries, 88.0%, 97.0%, and 99.7% of points calculated by the present model were within +/-2%, +/-5%, and +/-10%, respectively. In contrast, the Tourovsky *et al* (2005)

model resulted in 69.0%, 93.0%, and 98.0% of points within +/-2%, +/-5%, and +/-10%, respectively. While the geometries tested in this work were not completely analogous to those of Tourovsky (their evaluations were in patient data), both models were designed primarily to eliminate the central-axis semi-infinite slab approximation and were tested in geometries challenging for this approximation. We attribute that additional accuracy achieved by our model to the improvements we made in the material-dependence added to the nuclear halo and the reduced step size toward the end of range.

In the most recent publication on the fast dose calculator (FDC) by Yepes *et al* (2018), over 525 patient cases were examined. It was shown that the Eclipse TPS, based on a pencil beam algorithm, over-estimated the maximum dose by 10-15% in some patient cases compared to the FDC. These results are consistent with our observations in the patient-like phantoms that we studied, especially those using a SOBP (10-20%).

Jia *et al* (2012) reported that greater than 98.7% of the points in all geometries were within 2% or 2 mm (above the 10% dose level), except for geometries with low-density air regions. Agreement below the 10% isodose level was not reported. Our work showed a distinct improvement in the distance-to-agreement of the 1% isodose line below heterogeneities. The nuclear halo implementation in Fippel and Soukup (2004) and Jia *et al* (2012) was limited to water.

Souris *et al* 2016 stated that their model was within 2% or 1 mm of GEANT 4, which is higher accuracy than we were able to achieve (3% or 1 mm compared to MCNPX). However, Souris *et al* 2016 relied on a complex physical model, including stochastic transport for secondary protons characterizing the nuclear halo, which necessitated a multi-core implementation to achieve reasonable calculation times. Though our model did not achieve the levels of accuracy stated in Souris *et al* (2016), we think that our model strikes a good balance between speed and accuracy without requiring a multi-core or GPU implementation.

The model in this work has some limitations. Evaluations were performed in simple geometries, which was intentional to characterize the underlying transport physics. It could be argued that our evaluations were not tested in clinically realistic geometries, like voxellized patient anatomy. However, this is not a major limitation because in the example geometries that we studied, we carefully selected them to be severe tests. Because our

evaluations were inherently more sensitive than what would be encountered in patient geometry, we expect that dose errors from our model in patient anatomy would be smaller than what was observed in the geometries in this work. Thus, limiting our study to simple geometries was also a strength.

Many of the limitations in the present model could be resolved by ensuring agreement between stopping power calculations in the present model and MC and incorporating a material-dependent range straggling correction. Addition of both of these features to the model in this work would improve the dose differences even further, especially in areas distal to the depth of maximum dose. Another significant addition that should be made is including changes in secondary proton production as a function of material and energy. The present model neglected this effect; however, MCNPX output files indicated changes in the number of secondary particles produced due to non-elastic nuclear interactions in heterogeneities compared to water. In addition to the suggested modeling improvements, future work in this area should perform evaluations in patient data.

Finally, one remaining topic of discussion is the calculation time of the present model compared to general purpose Monte Carlo. This dissertation has largely been focused on presenting the improved accuracy of this model, but that presentation is predicated on calculating dose in a shorter timeframe than general-purpose Monte Carlo calculations. Using our 2.3GHz Intel Core i5 based system, a monoenergetic 250 MeV, 4x4 cm^2 field calculated in water for the model developed in this work required 5.6 minutes, or 0.09 processor-hours. In contrast, MCNPX simulations used 256 parallel 2.6 GHz 8-Core Sandy Bridge Xeon 64-bit processors to calculate this same geometry in about 42.3 minutes, or 180.5 processor-hours. Thus, our model achieved significant speedup compared with MCNPX. Calculation times for our dose model in other geometries varied mainly with the initial number of protons and the resolution of the dose grid.

CHAPTER 5. CONCLUSIONS

In this work, we have detailed approaches to improving both the primary and nuclear halo components of a proton dose model, with the aims of reducing the two sources of errors observed in Chapman *et al* (2017): (1) the central-axis semi-infinite slab approximation; and, (2) the lack of material dependence in the nuclear halo model. In Specific Aim 1, we introduced a primary dose model that was stochastically based to reduce errors due to the central-axis approximation. The simplified approach to predict fluence loss of primary protons and particle transport enabled our model to reduce calculation times without sacrificing much accuracy relative to a general-purpose Monte Carlo code. In Specific Aim 2, we presented an improved energy loss calculation method that allowed transformation of the calculation geometry to an equivalent water phantom in three dimensions. This method allowed transformation of the original nuclear halo equation (Chapman *et al* 2017) for any desired calculation geometry. In Specific Aim 3, we compared our improved primary and nuclear halo dose model with Monte Carlo simulations from MCNPX in three patient-like phantoms. Contrasting our improved primary and nuclear halo dose model against the PBA (Chapman *et al* 2017) showed the amount of improvement our new model achieved.

The hypothesis of this work was found to be false: the present model did not result in 100% of points passing our 3% or 1 mm criteria for each geometry that we tested. However, we did see improved pass rates for the present model compared to the PBA in virtually every case. Furthermore, dose differences between the present model and MC distal to heterogeneities sometimes exceeded 5% (laterally finite) and 3% (laterally infinite). It was seen that some systematic differences between stopping power data in MCNPX vs the present model for compact bone resulted in a shift of the Bragg peak. The present model also overestimated Bragg peak dose, which was further amplified by both the effective lateral distance calculation and the inverse square factor introduced in the improved energy loss calculation in Specific Aim 2. These confounding factors are likely the reason that we were not able to achieve dose differences less than 3% distal to laterally infinite heterogeneities in all cases. However, dose difference between the present model and MC distal to air slabs was reduced compared to the dose difference between the PBA and MC. Most significantly, in-field improvements, as well

as improvement in distance-to-agreement of the 1% isodose line, were observed for depths distal to deep (z = 30 cm), thick (4, 5 cm) air slabs.

Given the improvements and limitations observed in our work, future work in this area would benefit from investigating approaches to include changes in secondary particle production due to heterogeneities. Any model implementing this effect should include a fast and reliable approach to performing the additional energy loss calculations needed as this could result in a significant slowdown. Additionally, any future models would benefit from ensuring identical stopping power data between both the calculation model and the standard of comparison. Systematic differences between the two in our study likely contributed to the 0.5-1 mm discrepancy observed in Bragg peaks distal to compact bone heterogeneities. Finally, incorporating a material-dependent range straggling correction would likely address small differences in the Bragg peak that were observed in Specific Aim 2.

Overall, our results indicate significant improvement in dose calculation accuracy compared to our previous PBA (Chapman *et al* 2017) and suggest that these improvements will be dosimetrically important in heterogeneous patient anatomy. We attribute this additional accuracy to the improvements our model made to removing dependence on the central-axis semi-infinite slab approximation and the improved energy loss calculation that added in a material-dependence to the nuclear halo model.

REFERENCES

Agostinelli S., Allison J., Amako K., and Apostolakis J., 2003. Geant4 – a simulation toolkit. *Nucl. Instrum. Methods A.,* 506, 250-303.

Anand A., Sahoo N., Zhu X.R., Sawakuchi G.O., Poenisch F., Amos R.A., Ciangaru G., Titt U., Suzuki K., Mohan R., and Gillin M.T., 2012. A procedure to determine the planar integral spot dose values of proton pencil beam spots. *Med. Phys.,* 39, 891-900.

Berger, M.J., 1993. Penetration of proton beams through water I. Depth dose distribution, spectra and LET distribution. *NISTIR 5226.*

Berger, M.J., Coursey, J.S., Zucker, M.A., and Chang J., 2005. *ESTAR, PSTAR, and ASTAR: Computer Programs for Calculating Stopping-Power and Range Tables for Electrons, Protons, and Helium Ions* (version 1.2.3). [Online] Available: http://physics.nist.gov/Star [2011, September 14], National Institute of Standards and Technology, Gaithersburg, MD.

Bertini H.W., et. al., 1968. *Nucl. Instr. and Meth.*, 66.

Bethe, H.A., 1930. Zur theorie des durchgangs schneller korpuskularstrahlen durch materie. *Ann. Phys.,* 5, 324-400.

Bethe, H.A., 1953. Moliere's theory of multiple scatting. *Phys. Rev.,* 89, 1256-66.

Bloch, F., 1933. Zur bremsung rasch bewegter teilchen beim durchgang durch materie. *Ann. Phys.,* 16, 285-320.

Bohr, N., 1915. On the decrease of velocity of swiftly moving electrified particles in passing through matter. *Phil. Mag.,* 30, 581-612.

Bohr, N., 1948. The penetration of atomic particles through matter. *K. Dan. Vidensk. Selsk. Mat. Fys. Medd.,* 18(8), 1-144.

Box G.E.P. and Muller M.E., 1958. A Note on the Generation of Random Normal Deviates. *The Annals of Mathematical Statistics.*, 29(2), 610-11.

Bragg W. and Kleemen R., 1905. On the alpha particles of radium and their loss of range in passing through various atoms and molecules. *Phil. Mag.*, 10, 318-40.

Chadwick, M.B. *et al,* 2011. ENDF/B-VII.1 Nuclear data for science and technology: cross sections, covariances, fission product yields and decay data. *Nuclear Data Sheets*, 112, 2887-996.

Chapman, J.W., Knutson N.C., Fontenot J.D., Newhauser W.D., and Hogstrom K.R., 2017. Evaluating the accuracy of a three-term pencil beam algorithm in heterogeneous media. *Phys. Med. Biol.*, 62, 1172-91.

Chu W.T., Ludewigt B.A., and Renner T.R., 1993. Instrumentation for treatment of cancer using proton and light-ion beams. *Rev. Sci. Instrum.,* 65, 2055-2122.

Ciangaru G., Polf J.C., Bues M., and Smith A.R., 2005. Benchmarking analytical calculations of proton doses in heterogeneous matter. *Med. Phys.*, 32(12), 3511-23.

Clasie B., Depauw N., Fransen M., Goma C., Panahandeh H.R., Seco J., Flanz J.B., and Kooy H.M., 2012. Golden beam data for proton pencil-beam scanning. *Phys. Med. Biol.*, 57, 1147-58.

Deasy, J.O., 1998. A proton dose calculation algorithm for conformal therapy simulations based on Moliere's theory of lateral deflections. *Med. Phys.*, 32(12), 3511-23.

Donahue W., Newhauser W.D., and Ziegler J.F., 2016. Analytical model for ion stopping power and range in therapeutic energy interval for beams of hydrogen and heavier ions. *Phys. Med. Biol.*, 61(17), 6570-84.

Egashira Y., Nishio T., Hotta K., Kohno R., and Uesaka M., 2013. Application of the pencil-beam redefinition algorithm in heterogeneous media for proton beam therapy. *Phys. Med. Biol.*, 58, 1169-84.

Eyes, L., 1948. Multiple scattering with energy loss. *Phys. Rev.*, 74, 1534-35.

Ferrari A., Fasso A., Ranft J., and Sala P., 2005. FLUKA: a multi-particle transport code. *CERN, SLAC-R-773.*

Fippel M., 1999. Fast Monte Carlo dose calculation for photon beams based on the VMC electron algorithm. *Med. Phys.*, 26, 1466-75.

Fippel M. and Soukup M., 2004. A Monte Carlo dose calculation algorithm for proton therapy. *Med. Phys.*, 31(8), 2263-73.

Giantsoudi D., Schuemann J, Jia X., Dowdell S., Jian S., and Paganetti H., 2015. Validation of a GPU-based Monte Carlo code (gPMC) for proton radiation therapy: clinical cases study. *Phys. Med. Biol.*, 60, 2257-69.

Goiten M. and Busse J., 1975. Immobilization error: Some theoretical considerations. *Radiology*, 117, 407-12.

Gottschalk B., Koehler A.M., Schneider R.J., Sisterson J.M., and Wagner M.S., 1993. Multiple Coulomb scattering of 160 MeV protons. *Nucl. Instrum. Meth.* B74, 467-90.

Gottschalk, B., 2004. Passive Beam Spreading in Proton Radiation Therapy. *Unpublished book.* Available: http://physics.harvard.edu/~gottschalk.

Gottschalk, B., 2010. On the scattering power of radiotherapy protons. *Med. Phys.*, 37(1), 352-67.

Gottschalk B., Cascio E.W., Daartz J., Wagner M.S., 2015. On the nuclear halo of a proton pencil beam stopping in water. *Phys. Med. Biol.*, 60, 5627-54.

Hogstrom K.R., Mills M.D., and Almond P.R., 1981. Electron beam dose calculations. *Phys. Med. Biol.*, 26, 445-59.

Hong L., Goiten M., Bucciolini M., Comiskey R., Gottschalk B., Rosenthal S., Serago C., and Urie M., 1996. A pencil beam algorithm for proton dose calculations. *Phys. Med. Biol.*, 41, 1305-1330.

ICRP, 1975. Report on the Task Group on Reference Man, Publication 23, *International Commission on Radiological Protection,* Elmsford, New York. (Oxford: Pergamon Press)

ICRU, 1984. Radiation dosimetry: electron beams with energies between 1 and 50 MeV, Report 35, *International Commission on Radiation Units and Measurements,* Washington, D.C. (Oxford: Oxford University Press)

ICRU, 1989. Tissue substitutes in radiation dosimetry and measurement, Report 44, *International Commission on Radiation Units and Measurements,* Washington, D.C. (Oxford: Oxford University Press)

ICRU, 1993. Stopping powers and ranges for protons and alpha particles, Report 46, *International Commission on Radiation Units and Measurements,* Washington, D.C. (Oxford: Oxford University Press)

ICRU, 1998, Clinical proton dosimetry – part I: beam production, beam delivery and measurement of absorbed dose, Report 59, *International Commission on Radiation Units and Measurements,* Washington, D.C. (Oxford: Oxford University Press)

ICRU, 2000. Nuclear data for neutron and proton radiotherapy and for radiation protection, Report 63, *International Commission on Radiation Units and Measurements,* Washington, D.C. (Oxford: Oxford University Press)

ICRU, 2007. Prescribing, recording, and reporting proton-beam therapy, Report 78, *International Commission on Radiation Units and Measurements,* Washington, D.C. (Oxford: Oxford University Press)

Inaniwa T., Kanematsu N., Sato S., and Kohno R., 2016. A dose calculation algorithm with correction for proton-nucleus interactions in non-water materials for proton radiotherapy treatment planning. *Phys. Med. Biol.*, 61, 67-89.

Inaniwa T., Kanematsu N., Noda K., and Kamada T., 2017. Treatment planning of intensity modulated composite particle therapy with dose and linear energy transfer optimization. *Phys. Med. Biol.*, 62, 5180-97.

Jeraj R. and Keall P., 1999. Monte Carlo-based inverse treatment planning. *Phys. Med. Biol.*, 44, 1885-96.

Jeraj R., Keall P.J., and Siebers J.V., 2002. The effect of dose calculation accuracy on inverse treatment planning. *Phys. Med. Biol.*, 7, 391-407.

Jia X., Schuemann J., Paganetti H., and Jiang S.B., 2012. GPU-based fast Monte Carlo dose calculation for proton therapy. *Phys. Med. Biol.*, 57, 7783-97.

Ju T. and Simpson T., 2008. Geometric interpretation of the gamma dose distribution comparison technique: Interpolation-free calculation. *Med. Phys.*, 35(3), 879-87.

Kawrakow I., 2000. Accurate condensed history Monte Carlo simulation of electron transport, I. EGSnrc, the new EGS4 version. *Med. Phys.*, 27, 485-98.

Keall P.J., Siebers J.V., Joshi S., and Mohan R., 2004. Monte Carlo as a four-dimensional radiotherapy treatment-planning tool to account for respiratory motion. *Phys. Med. Biol.*, 49, 3639-48.

Kimstrand P., Tilly N., Ahnesjo A., and Traneus E., 2008. Experimental test of Monte Carlo proton transport at grazing incidence in GEANT4, FLUKA and MCNPX. *Phys. Med. Biol.*, 53, 1115-29.

Knutson N., 2012. Evaluation of a proton pencil beam algorithm for dose calculations in heterogeneous media. Master's Thesis, Louisiana State University, Baton Rouge, Louisiana.

Koch N. and Newhauser W., 2005. Virtual commissioning of a treatment planning system for proton therapy of ocular cancers. *Radiat. Prot. Dosim.*, 115, 159-63.

Koch N., Newhauser W.D., Titt U., Gombos D., Coombes K., and Starkschall G., 2008. Monte Carlo calculations and measurements of absorbed dose per monitor unit for the treatment of uveal melanoma with proton therapy. *Phys. Med. Biol.*, 53, 1581-94.

Landau, L., 1944. On the energy loss of fast particles by ionization. *J. Phys. (USSR)*, 8, 201-5.

Li Y., Zhu R.X., Sahoo N., Anand A., and Zhang X., 2012. Beyond Gaussians: a study of single-spot modeling for scanning proton dose calculations. *Phys. Med. Biol.*, 57, 983-97.

Lomax, A.J., 2009. Charged particle therapy: the physics of interaction. *Cancer J.*, 15, 285-91.

Newhauser W.D., Fontenot J., Zheng Y., Polf J., Titt U, Koch N., Zhang X., and Mohan R., 2007. Monte Carlo simulations for configuring and testing an analytical proton dose-calculation algorithm. *Phys. Med. Biol.*, 52, 4569-84.

Newhauser W.D., et. al., 2008. Monte Carlo proton radiation therapy planning calculations. *Trans. Am. Nucl. Soc.*, 99, 63-4.

Newhauser W.D. and Zhang R., 2015. The physics of proton therapy. *Phys. Med. Biol.*, 60, R155.
Orton C.G., Mondalek P.M., Spicka J.T., Herron D.S., and Andres L.I., 1984. Lung corrections in photon beam treatment planning: are we ready? *Int. J. Radiat. Oncol. Biol. Phys.*, 10, 2191-99.

Paganetti H., Jiang H., Parodi K., Slopsema R., and Engelsman R., 2008. Clinicial implementation of full Monte Carlo dose calculation in proton beam therapy. *Phys. Med. Biol.*, 53, 4825-53.

Paganetti H., 2012. Range uncertainties in proton therapy and the role of Monte Carlo simulations. *Phys. Med. Biol.*, 57, R99-117.

Pedroni E., Bacher R., Blattmann H., Bohringer T., Coray A., Lomax A., Lin S., Munkel G., Scheib S., Schneider U., and Tourovsky A., 1995. The 200 MeV proton therapy project at the Paul Scherrer Institute: Conceptual design and practical realization. *Med. Phys.*, 22(1), 37-53.

Pedroni E., Scheib S., Bohringer T., Coray A., Grossman M., Lin S. and Lomax A., 2005. Experimental characterization of physical modeling of the dose distribution of scanned pencil beam. *Phys. Med. Biol.*, 50, 541-61.

Peeler C.R. and Titt U., 2012. Monte Carlo study of radial energy deposition from primary and secondary particles for narrow and large proton beamlet source models. *Phys. Med. Biol.*, 57, 3785-92.

Pelowitz, D.B. (ed), 2011. MCNPX™ User's Manual, Version 2.7.0. (Los Alamos, NM: Los Alamos National Laboratory).

Perl J., Shin J., Schuemann J., Faddegon B., and Paganetti H., 2012. TOPAS: an innovative proton Monte Carlo platform for research and clinical applications. *Med. Phys.*, 39, 6818-37.

Petti, P.L., 1992. Differential-pencil-beam dose calculations for charged particles. *Med. Phys.*, 19(1), 137-49.

Polf J.C., Harvey M., Titt U., Newhauser W.D., and Smith A.R., 2007. Initial beam size study for passive scatter proton therapy: I. Monte Carlo verification. *Med. Phys.*, 34, 4213-8.

PTCOG, 2017. *Particle therapy facilities in operation.* [Online] Avaialable: http://ptcog.web.psi.ch/ptcentre.html (Particle Therapy Co-Operative Group).

Qin N., Botas P., Giantsoudi D., Schuemann J., Tian Z., Jian S.B., Paganetti H., and Jia X., 2016. Recent developments and comprehensive evaluations of a GPU-based Monte Carlo package for proton therapy. *Phys. Med. Biol.*, 61, 7347-62.

Randeniya S.D., Taddei P.J., Newhauser W.D., and Yepes P., 2009. Intercomparison of Monte Carlo Radiation Transport Codes MCNPX, GEANT4, and FLUKA for simulating proton radiotherapy of the eye. *Nucl. Technol.*, 168, 810-4.

Rossi B. and Griesen K., 1941. Cosmic-Ray Theory. *Rev. Mod. Phys.*, 12, 240-309.

Russell K.R., Grussell E., and Montelius A., 1995. Dose calculations in proton beams: range straggling corrections and energy scaling. *Phys. Med. Biol.*, 40, 1031-1043.

Rutherford, E., 1911. The scattering of α and β particles by matter and the structure of the atom. *Phil. Mag.*, 21, 669-88.

Sandison G.A., Chetsov A.V., 2000. Proton loss model for therapeutic beam dose calculations. *Med. Phys.*, 27(9), 2133-45.

Sawakuchi G.O., Titt U., Mirkovic D., and Mohan R., 2008. Desnity heterogeneities and the influence of multiple Coulomb and nuclear scatterings on the Bragg peak distal edge of proton therapy beams. *Phys. Med. Biol.*, 53, 4605-19.

Sawakuchi G.O., Zhu X.R., Poenisch F., Suzuki K., Ciangaru G., Titt U., Anand A., Mohan R., Gillin M.T., and Sahoo N., 2010a. Experimental characterization of the low-dose envelope of spot scanning proton beams. *Phys. Med. Biol.*, 55, 3467-78

Sawakuchi G.O., Mirkovic D., Perles L.A., Sahoo N., Zhu X.R., Ciangaru G., Suzuki K., Gillin M.T., Mohan R., and Titt U., 2010b. An MCNPX Monte Carlo model of a discrete spot scanning proton beam therapy nozzle. *Med. Phys.*, 37, 4690-70

Sawakuchi G.O., Titt U., Mirkovic D., Ciangaru G., Zhu X.R., Sahoo N., Gillin M.T., and Mohan R., 2010c. Monte Carlo investigation of the low-dose envelope from scanned proton pencil beams. *Phys. Med. Biol.*, 55, 711-21

Schaffner B., Pedroni E., and Lomax A., 1999. Dose calculation models for proton treatment planning using a dynamic beam delivery system: an attempt to include density heterogeneity effects in the analytical dose calculation. *Phys. Med. Biol.*, 44, 27-41.

Schaffner B., 2008. Proton dose calculation based on in-air fluence measurements. *Phys. Med. Biol.*, 53, 1545-62

Schneider U., Schaffner B., Lomax A.J., Pedroni E., and Tourvosky A., 1998. A technique for calculating range spectra of charged particle beams distal to thick inhomogeneities. *Med. Phys.*, 25, 457-63.

Schuemann J., Dowdell S., Grassberger C., Min C.H., and Paganetti H., 2014. Site-specific range uncertainties caused by dose calculation algorithms for proton therapy. *Phys. Med. Biol.*, 59, 4007-31.

Schuemann J., Giantsoudi D., Grassberger C., Moteabbed M., Min C.H., and Paganetti H., 2015. Assessing the clinical impact of approximations in analytical dose calculations for proton therapy. *Int. J. Radiat. Oncol.*, 92, 1157-64.

Shiu A.S. and Hogstrom K.R., 1991. Pencil-beam redefinition algorithm for electron dose distributions. *Med. Phys.*, 18(1), 7-18.

Soukup M., Fippel M., and Alber M., 2005. A pencil beam algorithm for intensity modulated proton therapy derived from Monte Carlo simulations. *Phys. Med. Biol.*, 59, 5089-104.

Szymanowski H. and Oelfke U., 2002. Two-dimensional pencil beam scaling: an improved proton dose algorithm for heterogeneous media. *Phys. Med. Biol.*, 47(18), 3313-30.

Souris K. and Lee J.A., 2016. Fast multipurpose Monte Carlo simulation for proton therapy using multi- and many-core CPU architectures. *Med. Phys.*, 43(4), 1700-12.

Stewart J.G. and Jackson A.W., 1975. The steepness of the dose response curve both for tumor cure and normal tissue injury. *Laryngoscope*, 85, 1107-11.

Taddei P.J., Fontenot J.D., Zheng Y., Mirkovic D., Lee A.K., Titt U., and Newhauser W.D., 2008. Reducing stray radiation dose to patients receiving passively scattered proton radiotherapy for prostate cancer. *Phys. Med. Biol.*, 53, 2131-47.

Testa M, Schuemann J., Lu H.M., Shin J., Faddegon B., Perl J., and Paganetti H., 2013. Experimental validation of the TOPAS Monte Carlo system for passive scattering proton therapy. *Med. Phys.*, 40, 121719.

Titt U., Sahoo N., Ding X., Zheng Y., Newhauser W.D., Zhu X.R., Polf J.C., Gillin M.T. and Mohan R., 2008. Assessment of the accuracy of an MCNPX-based Monte Carlo simulation model for predicting three-dimensional absorbed dose distributions. *Phys. Med. Biol*., 53, 4455-79.

Tourovksy A., Lomax A.J., Schneider U., and Pedroni E., 2005. Monte Carlo dose calculation for spot scanned proton therapy. *Phys. Med. Biol.*, 50, 971-81.

Vavilov, P.V., 1957. Ionization losses of high-energy heavy particles. *Sov. Phys. JETP*, 5, 749-51.

Westerly D.C., Mo X., Tome W.A., Mackie T.R., and Deluca P.M., 2013. A generalized 2D pencil beam scaling algorithm for proton dose calculation in heterogeneous slab geometries. *Med. Phys.*, 40, 061706.

Yamashita T., Akagi T. Aso T., Kimura A., and Sasaki T., 2012. Effect of inhomogeneity in a patient's body on the accuracy of the pencil beam algorithm in comparison to Monte Carlo. *Phys. Med. Biol.*, 57, 7673-88.

Yepes P., Randenjya S., Taddei P.J., and Newhauser W.D., 2009. A track-repeating algorithm for fast Monte Carlo dose calculations of proton radiotherapy. *Nucl. Technol.*, 168, 736-40.

Yepes P., Mirkovic D., and Taddei P.J., 2010. A GPU implementation of a track-repeating algorithm for proton radiotherapy dose calculations. *Phys. Med. Biol.*, 55, 7107-7120.

Yepes P., Guan F., Kerr M., Randeniya S., Li Y., Bronk L., Liu A., Mirkovic D., Sahoo N., Titt U., Anand A., and Mohan R., 2016a. Validation of a track-repeating algorithm versus measurements in water for proton scanning beams. *Biomed. Phys. Eng. Express.*, 2, 037002.

Yepes P., Eley J., Liu A., Mirkovic D., Randeniya S., Titt U., and Mohan R., 2016b. Validation of a track repeating algorithm for intensity modulated proton therapy: clinical cases study. *Phys. Med. Biol.*, 61, 2633-45.

Yepes P., Adair A., Grosshans D., Mirkovic D., Poenisch F., Titt U., Wang Q., and Mohan R., 2018. Comparison of Monte Carlo and analytical dose computations for intensity modulated proton therapy. *Phys. Med. Biol.*, 63, 045003.

Zhang X., Liu W., Li Y., Li X., Quan M., Mohan R., Anand A., Sahoo N., Gillin M., and Zhu X.R., 2011. Paramaterization of multiple Bragg curves for scanning proton beams using simulationeous fitting of multiple curves. *Phys. Med. Biol.*, 56, 7725-35.

Zhu X.R., Poenisch F., Lii M., Sawakuchi G.O., Titt U., Bues M., Song X., Zhang X., Li Y., Ciangaru G., Li H., Taylor M.B., Suzuki K., Mohan R., Gillin M.T., and Sahoo N., 2013. Commissioning dose computation models for spot scanning proton beams in water for a commercially available treatment planning system. *Med. Phys.*, 40, 041723.

Ziegler J.F., Biersack J.P., and Ziegler M.D., 2012. SRIM: The Stopping and Range of Ions in Matter (Chester, MD.: SRIM Co.).

APPENDIX. SUPPLEMENTAL DATA

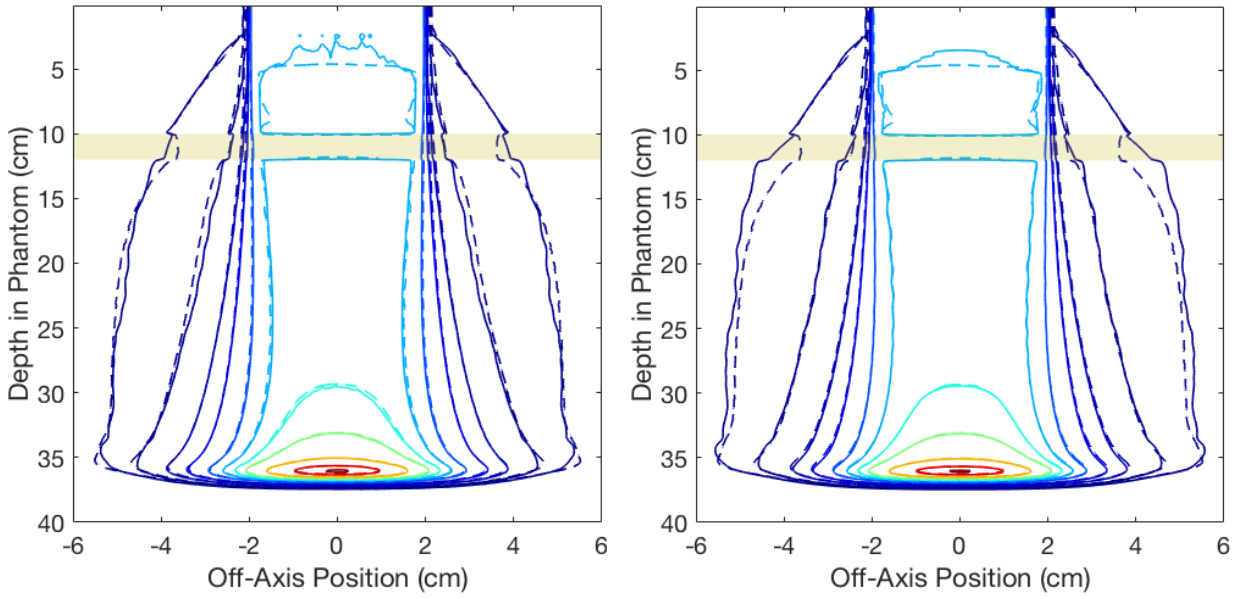

(a) (b)

Figure A.1. Isodose (1, 2, 5, 10, 20, 30, 40, 50, 70, 90, and 100%) comparisons for a 250 MeV, 4x4 cm^2 beam in a water phantom with a 2 cm compact bone slab at *z=10 cm* that stretches across the entire width of the phantom. Shown using (a) sbMC (solid) vs MC (dashed), and (b) Chapman *et al* (2017) model (solid) and MC (dashed). Pass rates were 100% (a) and 100% (b). The bone slab is indicated as a translucent yellow rectangle.

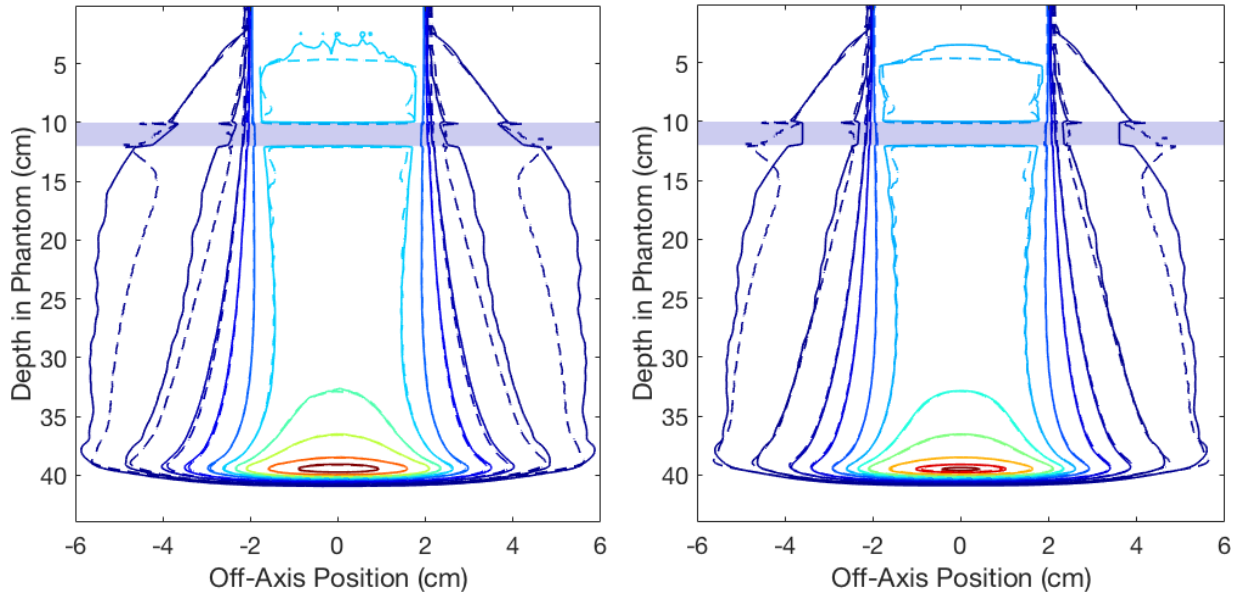

(a) (b)

Figure A.2. Isodose (1, 2, 5, 10, 20, 30, 40, 50, 70, 90, and 100%) comparisons for a 250 MeV, 4x4 cm^2 beam in a water phantom with a 2 cm air slab at *z=10 cm* that stretches across the entire width of the phantom. Shown using (a) sbMC (solid) vs MC (dashed), and (b) Chapman *et al* (2017) model (solid) and MC (dashed). Pass rates were 99.8% (a) and 99.8% (b). The air slab is indicated as a translucent blue rectangle.

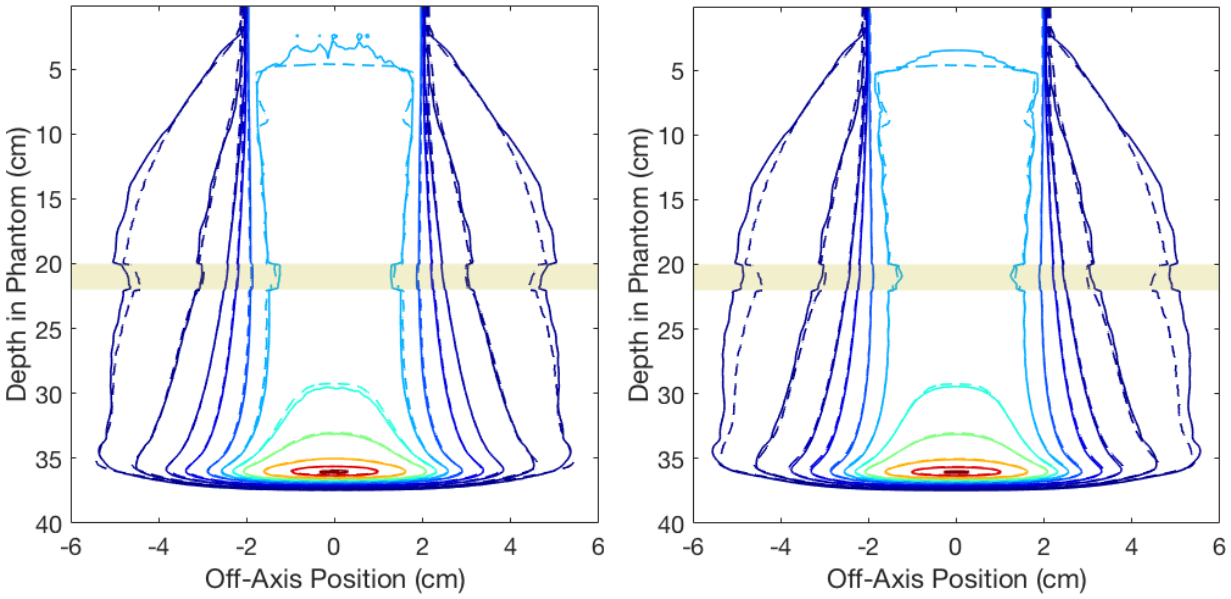

(a) (b)

Figure A.3. Isodose (1, 2, 5, 10, 20, 30, 40, 50, 70, 90, and 100%) comparisons for a 250 MeV, 4x4 cm^2 beam in a water phantom with a 2 cm compact bone slab at *z=20 cm* that stretches across the entire width of the phantom. Shown using (a) sbMC (solid) vs MC (dashed), and (b) Chapman *et al* (2017) model (solid) and MC (dashed). Pass rates were 100% (a) and 100% (b). The bone slab is indicated as a translucent yellow rectangle.

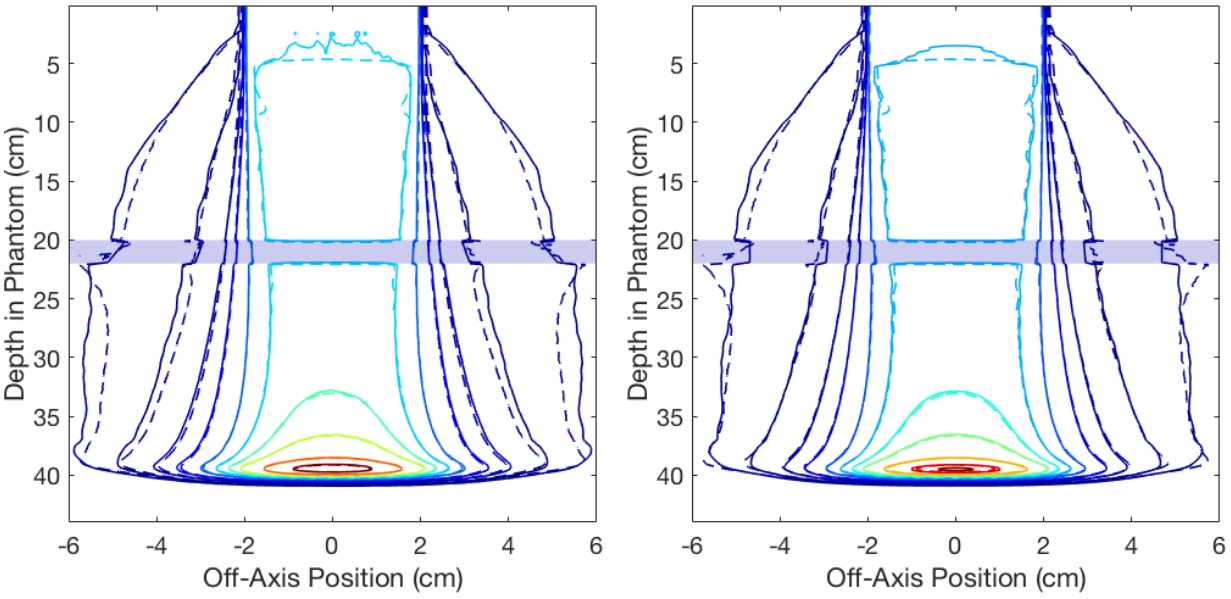

(a) (b)

Figure A.4. Isodose (1, 2, 5, 10, 20, 30, 40, 50, 70, 90, and 100%) comparisons for a 250 MeV, 4x4 cm^2 beam in a water phantom with a 2 cm air slab at *z=20 cm* that stretches across the entire width of the phantom. Shown using (a) sbMC (solid) vs MC (dashed), and (b) Chapman *et al* (2017) model (solid) and MC (dashed). Pass rates were 99.8% (a) and 99.8% (b). The air slab is indicated as a translucent blue rectangle.

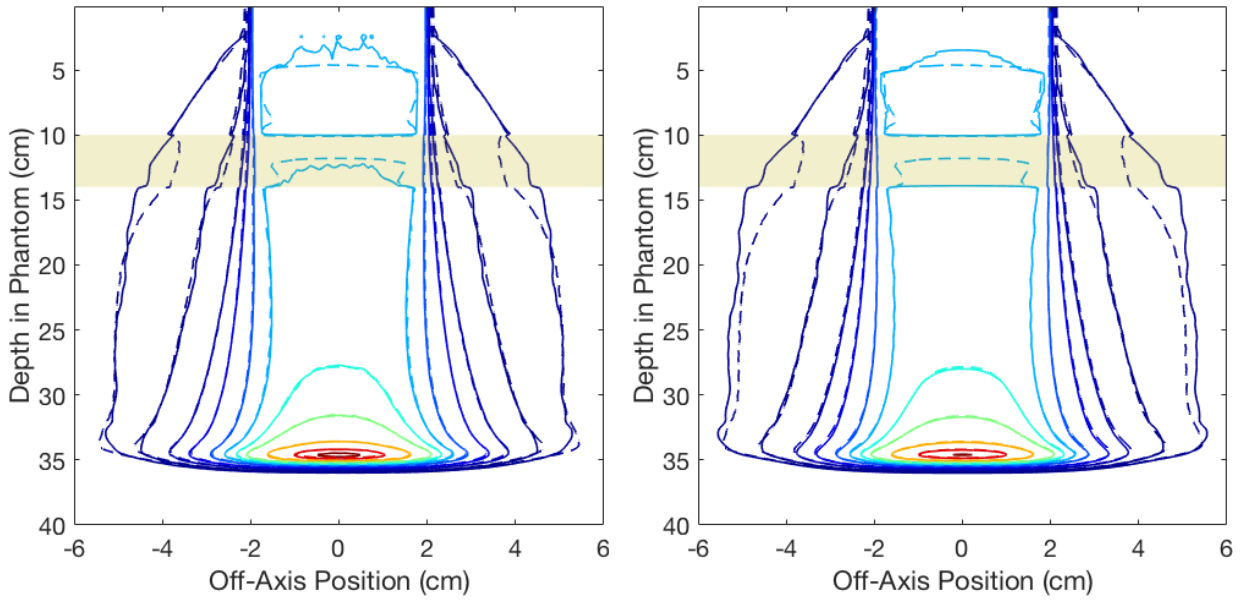

(a) (b)

Figure A.5. Isodose (1, 2, 5, 10, 20, 30, 40, 50, 70, 90, and 100%) comparisons for a 250 MeV, 4x4 cm^2 beam in a water phantom with a 4 cm bone slab at *z=10 cm* that stretches across the entire width of the phantom. Shown using (a) sbMC (solid) vs MC (dashed), and (b) Chapman *et al* (2017) model (solid) and MC (dashed). Pass rates were 100% in (a) and (b). The bone slab is indicated as a translucent yellow rectangle.

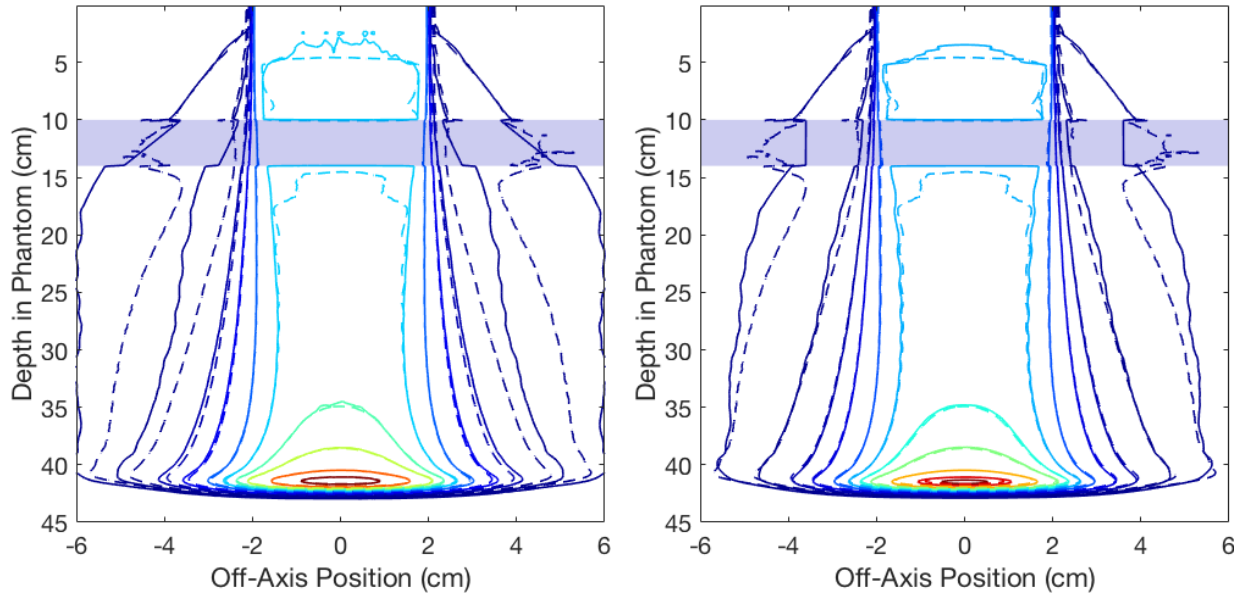

(a) (b)

Figure A.6. Isodose (1, 2, 5, 10, 20, 30, 40, 50, 70, 90, and 100%) comparisons for a 250 MeV, 4x4 cm^2 beam in a water phantom with a 4 cm air slab at *z=10 cm* that stretches across the entire width of the phantom. Shown using (a) sbMC (solid) vs MC (dashed), and (b) Chapman *et al* (2017) model (solid) and MC (dashed). Pass rates were 99.6% (a) and 99.6% (b). The air slab is indicated as a translucent blue rectangle.

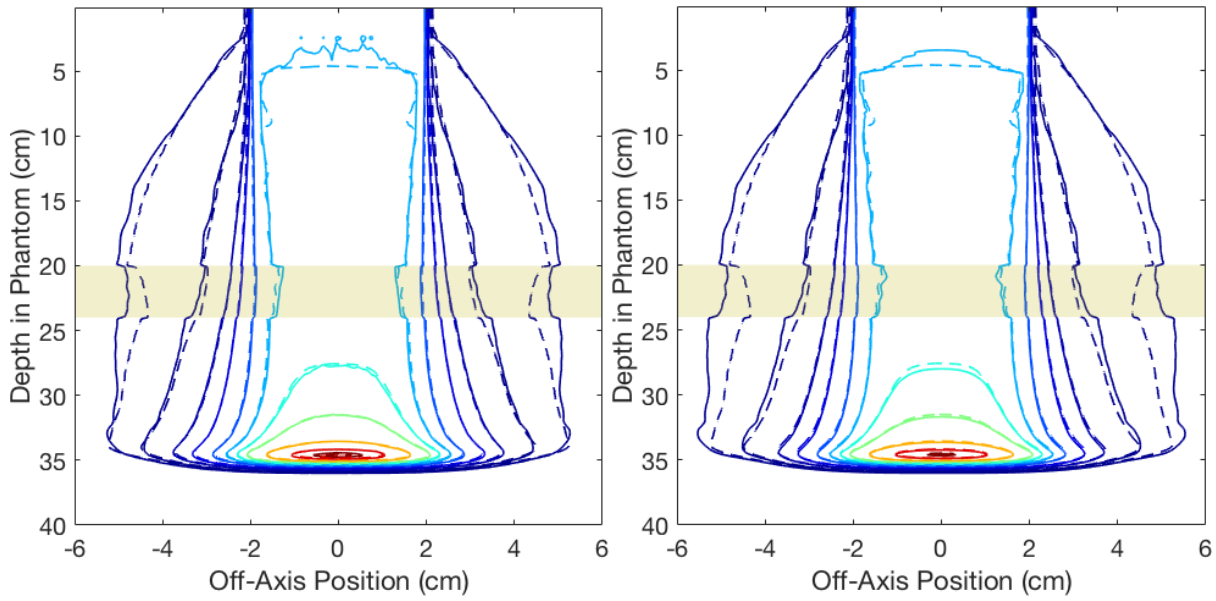

(a) (b)

Figure A.7. Isodose (1, 2, 5, 10, 20, 30, 40, 50, 70, 90, and 100%) comparisons for a 250 MeV, 4x4 cm^2 beam in a water phantom with a 4 cm bone slab at *z=20 cm* that stretches across the entire width of the phantom. Shown using (a) sbMC (solid) vs MC (dashed), and (b) Chapman *et al* (2017) model (solid) and MC (dashed). Pass rates were 100% (a) and 100% (b). The bone slab is indicated as a translucent yellow rectangle.

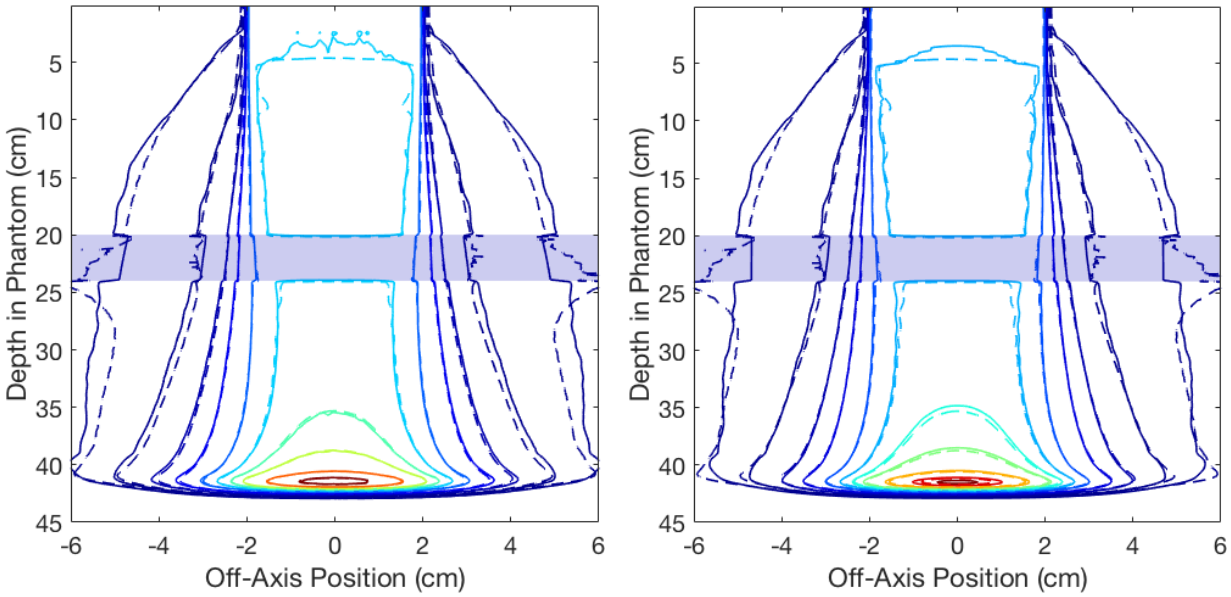

(a) (b)

Figure A.8. Isodose (1, 2, 5, 10, 20, 30, 40, 50, 70, 90, and 100%) comparisons for a 250 MeV, 4x4 cm^2 beam in a water phantom with a 4 cm air slab at *z=20 cm* that stretches across the entire width of the phantom. Shown using (a) sbMC (solid) vs MC (dashed), and (b) Chapman *et al* (2017) model (solid) and MC (dashed). Pass rates were 99.6% (a) and 99.4% (b). The air slab is indicated as a translucent blue rectangle.

VITA

John Chapman was born in Lake Charles, Louisiana, in 1984. He was raised in Westlake, Louisiana, and graduated from Westlake High School in May of 2002. Since 2004, he earned a Bachelor of Science in Electrical Engineering degree with a minor in mathematics at Louisiana State University, and in 2012, he earned a Master of Science in Medical Physics at Louisiana State University. In the summer of 2018, he will enroll in the medical physics residency program at Washington University in St. Louis to further his clinical exposure in preparation for a career as an academic clinical medical physicist.